# MULTIPLEXED FLUORESCENCE DIFFUSE OPTICAL TOMOGRAPHY

A Thesis
Presented to
The Academic Faculty

by

Ali Behrooz

In Partial Fulfillment
of the Requirements for the Degree
Doctor of Philosophy in
Electrical and Computer Engineering


**School of Electrical and Computer Engineering**

**Georgia Institute of Technology**

**December 2013**

# MULTIPLEXED FLUORESCENCE DIFFUSE OPTICAL TOMOGRAPHY

Approved by:

Dr. Ali Adibi, Advisor
School of Electrical and Computer Engineering
*Georgia Institute of Technology*

Dr. John A. Buck
School of Electrical and Computer Engineering
*Georgia Institute of Technology*

Dr. Gee-Kung Chang
School of Electrical and Computer Engineering
*Georgia Institute of Technology*

Dr. Albert B. Frazier
School of Electrical and Computer Engineering
*Georgia Institute of Technology*

Dr. Hao-Min Zhou
School of Mathematics
*Georgia Institute of Technology*

Date Approved: November 4, 2013

*To my family, for their love and support.*

# ACKNOWLEDGEMENTS

First and foremost, I wish to thank my parents and my sister, Guiti, Leili and Alireza, for their unconditional love, support, and understanding throughout this long journey.

I wish to thank my doctoral advisor, Professor Ali Adibi, and my mentors at Georgia Tech, Professor Hao-Min Zhou, and Dr. Reza Eftekhar, for their guidance in this endeavor.

I am profoundly grateful to my colleagues and mentors at PerkinElmer, Dr. Brad Rice, Dr. Chaincy Kuo, Dr. Heng Xu, and Dr. Daniel Stearns, from whom I learned the many complex aspects of molecular imaging.

I wish to acknowledge my reading committee for their dedication and guidance throughout the preparation of this dissertation: Professor John A. Buck, Professor Gee-Kung Chang, and Professor Albert B. Frazier.

# TABLE OF CONTENTS

# LIST OF TABLES

# LIST OF FIGURES

# LIST OF ABBREVIATIONS

| | |
|---|---|
| 1D | One Dimensional |
| 2D | Two Dimensional |
| 3D | Three Dimensional |
| ART | Algebraic Reconstruction Technique |
| CCD | Charge-Coupled Device |
| CT | Computed Tomography |
| CW | Continuous Wave |
| DMSO | Dimethyl Sulfoxide |
| DOT | Diffuse Optical Tomography |
| FEM | Finite Element Method |
| FT | Fluorescence Tomography |
| ICG | Indocyanine Green |
| LED | Light-Emitting Diode |
| MRI | Magnetic Resonance Imaging |
| MLS-ART | Multi-Level Scheme Algebraic Reconstruction Technique |
| NIR | Near Infra-Red |
| PDE | Partial Differential Equation |
| PET | Positron Emission Tomography |
| PSF | Point Spread Function |
| ROF | Rudin Osher Fatemi |
| RTE | Radiative Transfer Equation |
| SVD | Singular Value Decomposition |
| TV | Total Variation |

# LIST OF SYMBOLS

| | |
|---|---|
| $\lambda$ | Regularization Parameter (weight) |
| $\eta$ | Fluorescent Quantum Efficiency |
| $\mu_a$ | Optical Absorption Coefficient |
| $\mu_{fl}$ | Fluorescent Absorption Coefficient |
| $\mu_s$ | Scattering Coefficient |
| $\Phi$ | Average Radiance (Fluence) |
| $\omega$ | Modulation Frequency |
| D | Diffusion Coefficient |
| M | Fluorescence Tomography System Matrix |
| p | Scattering Phase Function |
| U | Optical Radiance |
| W | Hadamard Multiplexing Matrix |
| x | Fluorescent Distribution Vector |
| y | Fluorescence Tomography Data Vector |

# SUMMARY

Fluorescence Tomography (FT) is an optical imaging modality extensively used for non-invasive *in vivo* localization and quantification of the distribution of fluorophore-tagged molecules and inclusions in animal and human subjects. This technology offers *in vivo* functional three-dimensional localization of fluorescence up to few centimeters under the skin using non-invasive optical measurements. Empowered by a host of targeted, activated, and vascular probe technologies, this imaging technique has found crucial applications in preclinical studies for cancer research, drug monitoring, and development.

The performance of existing FT systems in accurately imaging and reconstructing the fluorescent agents inside optically turbid media such as tissue is severely hindered by the ill-posed nature of the reconstruction problem, modeling errors, and weak and noisy data.

In this work, a multiplexed FT system is conceptualized and developed that has the potential to circumvent the limitations of existing single-point illumination FT systems. Accompanied by several novel reconstruction techniques as part of the preliminary research, the Hadamard multiplexed FT system shows great promise for enhancing the throughput in FT systems and adding robustness to 3D reconstructions in FT.

# CHAPTER 1

# INTRODUCTION TO FLUORESCENCE TOMGORAPHY (FT)

## 1.1 Background

Medical and molecular imaging modalities have long been used for non-invasive three-dimensional (3D) localization and quantification of inclusions such as cancer lesions, test drugs, and reporter genes buried at different depths in biological tissue [1-5]. Every bio-imaging platform has unique advantages to offer and is primarily employed in areas where its advantages are of interest. Various bands of the electromagnetic spectrum have been extensively used for medical imaging purposes for decades, *e.g.*, X-ray in computed tomography (CT), radio frequency (RF) in magnetic resonance imaging (MRI), and gamma radiation in positron emission tomography (PET). However, the use of visible and near infra-red light in *in vivo* imaging has only recently been explored [6-11]. Strong diffusion of the visible and near infra-red photons in biological tissue is the main reason behind the late arrival of deep tissue optical imaging. Modeling of light diffusion in turbid and highly scattering biological tissue is computationally costly and requires bulky data processing. Also, depth-resolved 3D localization of inclusions using non-invasive surface density measurements of diffuse and scattered photons requires low-noise detectors and high-precision hardware [6]. With the advent of high-speed processors and advancements in the field of optoelectronics in recent decades, the computational burden of optical tomography has become manageable, and highly accurate light measurements have become available, thus giving rise to widespread research on the topic of optical imaging.

Similar to various imaging modalities such as MRI or PET, the performance of optical imaging is greatly enhanced by contrast agents that are used to tag and track inclusions of interest [10, 11]. Moreover, in many cases where anatomical and physiological contrast is weak or does not exist, molecular probes must be employed to target and localize inclusions [12-15]. Fluorescent probes are the most popular contrast agents used in optical imaging and microscopy because of their widespread availability, increased versatility, and high efficiency [16]. They have been shown to label cancer lesions [16], test drugs [13], enzymes, and messenger proteins *in vivo* [10]. When used in deep tissue diffuse optical imaging, fluorescent agents provide the necessary contrast for early tumor detection, drug monitoring, drug discovery, and *in vivo* biology and genetics research. These contrast agents can be used in both animal and human subject. For example, a number of fluorescent probes belonging to the indocyanine green (ICG) family have recently been approved by the Food and Drug Administration (FDA) for low-dosage clinical applications and serve as the primary optical contrast agents for fluorescent enhanced optical mammography [17]. Moreover, a wide variety of rhodamine and cyanine dyes, such as Alexa Fluor® [18], are widely used in fluorescence optical tomography for preclinical and small animal studies in cell biology and cancer research [19]. The variety and availability of fluorescent dyes for *in vivo* labeling and tracking of molecular and physiological processes are the significant advantages of fluorescence diffuse optical tomography over other *in vivo* imaging platforms.

Fluorescence diffuse optical tomography, referred to as fluorescence tomography (FT) herein, is presently attracting extensive attention from pharmaceutical industries, biology researchers, and radiology community because of its unique capabilities.

However, this imaging technology suffers from drawbacks that impair its performance. To compete with other conventional diagnostic imaging platforms, the performance of FT must be improved and its drawbacks must be resolved. The major drawbacks of FT stem from the mathematically ill-posed and intractable problem of reconstructing the quantitative 3D distribution of administered fluorescent agents labeling inclusions of interest from the measured surface density of diffuse and scattered photons emitted by these agents. Therefore, the efficacy of the optical hardware used for the fluorescence tomographic scan and the quality of the post-processing inversion algorithms are extremely important and crucial in the successful performance of FT. This work is focused on the development and implementation of cost-effective high-throughput instrumentation and computational algorithms for improving the accuracy and robustness of FT systems. This work is aimed at circumventing the current limitations and drawbacks of FT by developing robust novel algorithms and system architecture that significantly improve the performance of FT.

## 1.2 Modeling

Fluorescence tomography (FT) aims at 3D localization and quantification of fluorescent agents buried deep in biological tissue. The optical absorption of biological tissue plummets in the near infra-red spectrum (wavelength range of 750-1000 nm) [2], as shown in Figure 1, allowing for light to diffuse through layers of tissue. The major chromophores in biological tissue, namely water, lipids, oxy- and deoxy-hemoglobin, demonstrate relatively low optical absorption in the NIR spectrum compared to visible and infra-red. Consequently, the NIR band provides a spectral window for photons to diffuse through layers of tissue before being entirely absorbed.

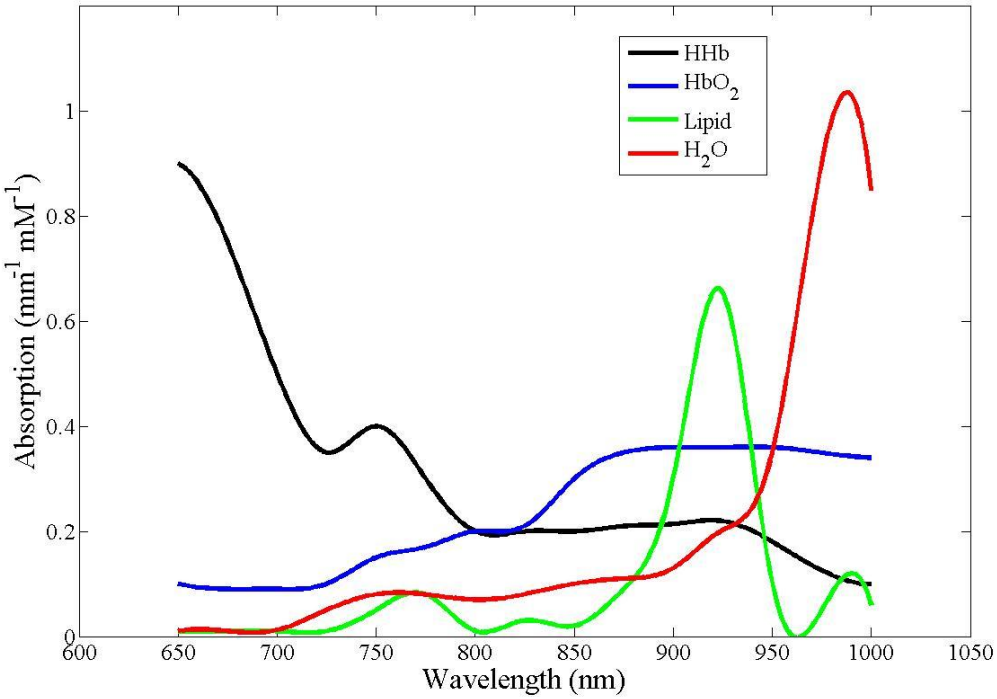


**Figure 1: Spectra of optical absorption of major chromophores in tissue, water, lipid, oxy-hemoglobin ($HbO_2$) and deoxy-hemoglobin (HHb) plummet in the near infra-red window.**

Therefore, tissue can be regarded as a highly scattering low absorptive medium for near infra-red light propagation [6]. Reduced tissue absorption in the near infra-red window is exploited in many areas of biomedical optics including fluorescence tomography [6]; the fluorescent dyes used in FT are excited by and emit near infra-red radiation, *e.g.*, Alexa Fluor® 750 (excitation 750 nm and emission 775 nm) and Indocyanine Green (excitation 800 nm and emission 840 nm).

In FT, tissue surface is illuminated by near infra-red light directed from a laser or a light emitting diode (LED). The near infra-red wavelength used for illuminating the tissue matches the excitation wavelength of the administered fluorescent agents. The near infra-red radiation penetrates the tissue and excites the fluorophores distributed over its volume. The excited fluorophores emit near infra-red radiation at a higher wavelength

than their excitation wavelength. The emitted photons propagate to the surface of the tissue. By collecting the diffuse fluorescent photons on the tissue surface and measuring their surface intensity, the 3D distribution of the fluorescent dyes is estimated in FT. The propagation of light in highly scattering turbid media such as tissue is modeled by the radiative transport equation (RTE) [20] as formulated in Equation 1:

$$\frac{1}{c}\frac{\partial}{\partial t}U(r,\hat{s},t) + \hat{s}.\nabla U(r,\hat{s},t) + (\mu_s + \mu_a)U(r,\hat{s},t) = \mu_s \int U(r,\hat{s},t)p(\hat{s},\hat{s}')d\hat{s}' + S(r,\hat{s},t), \quad (1)$$

where c is the speed of light in vacuum in meters per second, $\hat{s}$ is the unit vector in the direction of interest, and $\mu_s$ and $\mu_a$ are the scattering and absorption coefficients of the medium in inverse meters. The function $p(\hat{s},\hat{s}')$ is the scattering phase function which quantifies the probability of a photon with initial direction $\hat{s}'$ to be scattered off to direction $\hat{s}$. The function $S(r,\hat{s},t)$ is the source strength at location r in direction $\hat{s}$ at time t in Watts per steradian per cubic meter, and $U(r,\hat{s},t)$ is the radiance at location r in direction $\hat{s}$ at time t in Watts per steradian per square meter. In, Equation 1, the transport of light or radiative energy within a medium characterized by high optical scattering and an arbitrary level of optical absorption with radiative sources distributed over the volume of the medium is described.

The right-hand side of Equation 1 contains the temporal change, spatial change, and loss from absorption and scattering in the radiance $U(r,\hat{s},t)$, and the left-hand side contains the source strength term in direction $\hat{s}$ that describes the local source contribution to $U(r,\hat{s},t)$ and the total contributions of photons scattered off to direction $\hat{s}$ from all other directions. Equation 1 accurately models the behavior of light in turbid media and is used for photon transport modeling in optical tomography by some researchers [21, 22]. However, it has been shown that a first-order approximation to

Equation 1 greatly reduces the computational complexity and numerical burden of modeling while maintaining a relatively high level of accuracy sufficient for optical imaging purposes [23]. The first-order approximation, which is broadly used by the optical tomography community [24], results in a first-order partial differential equation (PDE) called the diffusion equation as formulated below

$$\frac{1}{c}\frac{\partial}{\partial t}\Phi(r,t) - \nabla.D(r)\nabla\Phi(r,t) + \mu_a(r)\Phi(r,t) = q(r,t), \tag{2}$$

where $D(r)$ is the diffusion coefficient in meters, $\Phi(r,t)$ is the average radiance or fluence in Watts per square meter, and $q(r,t)$ is the source power density in Watts per square meter. Mathematically, they can be defined as

$$D(r) = \frac{1}{3(\mu_s'(r)+\mu_a(r))}, \tag{3-5}$$

$$\Phi(r,t) = \int U(r,\hat{s},t)d\hat{s},$$

$$q(r,t) = \int S(r,\hat{s},t)d\hat{s}.$$

In Equation 2, the time-domain diffusion equation is formulated. This equation is mainly used for fluorescence lifetime imaging and time-domain fluorescence tomography [25, 26]. In most applications of FT, however, the source intensity and hence the fluorescent signal intensity either remain constant over time or follow single frequency periodic oscillations. The frequency-domain diffusion equation, formulated as

$$\frac{1}{c}i\omega\Phi(r,t) - \nabla.D(r)\nabla\Phi(r) + \mu_a(r)\Phi(r) = q(r), \tag{6}$$

is the broadly used form of the diffusion equation, since frequency-domain and continuous-wave (CW) systems are currently the most widely used FT platforms. It must

be noted that, as shown in Equations 1 and 2, the temporal derivative term represents the temporal change in the radiance or fluence rate and not the temporal change in the electromagnetic field intensity. In the context of optical imaging, the term frequency refers to the modulation frequency of the source intensity and not the frequency of the light wave propagating in the tissue. To avoid confusion, the term wavelength is only used to specify the electromagnetic wavelength of the visible or near infra-red light propagating in the tissue. The term frequency is used to specify the frequency of the intensity modulation of fluence. While frequency modulation can add some extra information to the collected data, it requires highly sensitive, complex, and costly hardware. Also, frequency modulation only makes a significant difference in the accuracy of the tomographic localization of deep sources embedded in very thick (5-6 cm) tissues [27]. Hence, continuous-wave FT is preferred over frequency-domain FT in preclinical applications, *e.g.*, small animal imaging, where the animal is at most two to three centimeters thick [28]. Continuous-wave FT is quite analogous to a direct-current (DC) system where quantities remain constant over time. The diffusion equation for CW FT is formulated in Equation 7:

$$-\nabla.\,\mathrm{D}(\mathrm{r})\nabla\Phi(\mathrm{r}) + \mu_{\mathrm{a}}(\mathrm{r})\Phi(\mathrm{r}) = \mathrm{q}(\mathrm{r}). \tag{7}$$

## 1.3 Methodology

In Figure 2, a two-dimensional (2D) configuration for FT is depicted. The turbid medium or tissue is illuminated at a sequence of boundary points by laser or LED radiation at the excitation wavelength of the administered fluorescent agents that are distributed throughout the volume of the medium. The diffuse photons propagating through the tissue excite the fluorescent agents resulting in the emission of fluorescent

photons that travel to the tissue surface and are collected at several boundary locations by optical detectors.

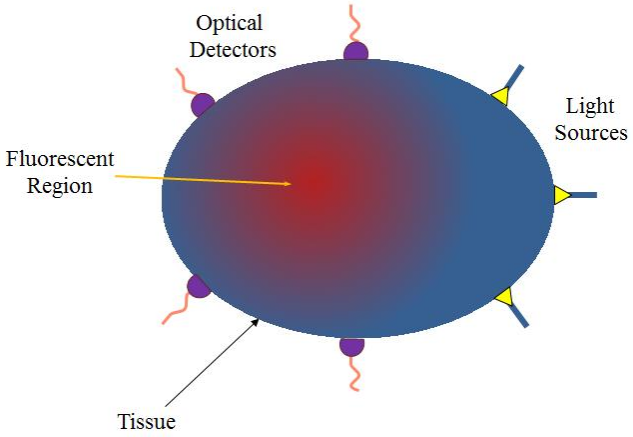


**Figure 2: Fluorescence tomography (FT) is performed by illuminating the tissue at several source locations and measuring the emitted fluorescent signal at several boundary points using detectors.**

Therefore, two coupled diffusion equations describe the dynamics of a fluorescence tomographic scan; one is for the diffusion of excitation photons and the other is for the diffusion of fluorescent photons. The coupled equations are formulated as below

$$-\nabla.\,\mathrm{D}(\mathrm{r})\nabla\Phi_{exc}(\mathrm{r}) + \mu_{\mathrm{a}}(\mathrm{r})\Phi_{exc}(\mathrm{r}) = \mathrm{q}_{exc}(\mathrm{r}), \tag{8}$$

$$-\nabla.\,\mathrm{D}(\mathrm{r})\nabla\Phi_{em}(\mathrm{r}) + \mu_{\mathrm{a}}(\mathrm{r})\Phi_{em}(\mathrm{r}) = \eta\mu_{fl}\mathrm{c}(\mathrm{r})\Phi_{exc}(\mathrm{r}), \tag{9}$$

where $\Phi_{exc}(\mathrm{r})$ is the average fluence of excitation photons at location r, $\mathrm{q}_{exc}(\mathrm{r})$ is the power density of the excitation laser or LED source used for the illumination of the tissue at location r (as a result, $\mathrm{q}_{exc}(\mathrm{r})$ is zero inside the tissue and non-zero at the boundary source locations), $\Phi_{em}(\mathrm{r})$ is the average fluence of the fluorescent light at location r, $\eta$ is the dimensionless quantum efficiency of the fluorescent dye, $\mu_{fl}$ is the per-molar fluorescent absorption coefficient, and $\mathrm{c}(\mathrm{r})$ is the molar concentration of the fluorescent

dye at location r. As formulated in the right-hand side of Equation 9, the source intensity term for the emission diffusion equation is the product of the quantum efficiency, the per-molar fluorescent dye absorption, the fluorescent dye concentration, and the excitation fluence. The boundary conditions accompanying Equations 8 and 9 are modified Robin-type boundary conditions [29] expressed as

$$\Phi(\xi) + 2AD(\xi)\hat{n}.\nabla\Phi(\xi) = 0, \tag{10}$$

where $\xi$ is any given point on the boundary, $\hat{n}$ is the normal vector to the boundary surface at $\xi$, and A is a dimensionless constant that accounts for the index mismatch and internal reflection at the boundary. More mathematical details about Equation 10 and its variables can be found in Ref. [29]. The modified Robin condition sets the fluence directly below the surface equal to the surface optical flux which effectively models the tissue-air boundary condition [29].

In FT, $c(r)$ is estimated using the coupled excitation and emission diffusion equations, and the Robin-type boundary conditions. This is accomplished by varying $q_{exc}(r)$ (through changing the boundary source location) and measuring $\Phi_{exc}(r)$ and $\Phi_{em}(r)$ on the boundary of the medium while $D(r)$, $\mu_a(r)$, $\eta$, and $\mu_{fl}$ are either known *a priori* or determined using diffuse optical tomography (DOT) [6], and dye absorbance and efficiency measurements [30]. Finding $c(r)$ can be decomposed into two problems: the forward problem, and the inverse problem. The forward problem involves solving Equation 8 and finding $\Phi_{exc}(r)$ at every point inside and on the boundary of the tissue. The inverse problem involves finding $c(r)$ using $\Phi_{exc}(r)$, which is obtained from solving the forward problem, and boundary measurements of $\Phi_{em}(r)$. The core step in solving the forward problem is finding the Green's functions of the excitation equation (Equation

8). A Green's function is the solution of an inhomogeneous partial differential equation (PDE) with a Dirac delta source term or inhomogeneity [31]. Solutions to linear PDEs with arbitrary source terms can be written as a linear convolution of the Green's functions with the source term [31].

Depending on the parameters and the geometry of the problem, various techniques can be used to find the Green's functions and hence the solution of the forward problem. Analytical expressions are easily derived for infinite or semi-infinite media [32], however, real FT scenarios involve arbitrary and possibly irregular geometries, *e.g.*, large rodents, and therefore analytical solutions derived for regular geometries cannot always be used. It has been shown, however, that for a homogeneous medium (*i.e.*, a medium with spatially homogeneous optical absorption and scattering) with an arbitrary geometry, approximate semi-analytical expressions can be formulated as below [33]

$$G_{ij} = \frac{1}{2\pi D}\left(\frac{\exp(-\mu_{eff}\, r_{ij})}{r_{ij}} - \frac{1}{z_b}\int_0^{\infty} \exp\left(\frac{-x}{z_b}\right)\frac{\exp\left(-\mu_{eff}\sqrt{(d_j+x)^2+{p_{ij}}^2}\right)}{\sqrt{(d_j+x)^2+{p_{ij}}^2}}\, dx\right), \qquad (11)$$

where $d_j$ is the distance of the point indexed j from the plane tangent to the medium at the boundary point source indexed i and $p_{ij}$ is the distance of the source indexed i to a point on the tangent plane closest to the point indexed j. Hence, $r_{ij} = \sqrt{{d_j}^2 + {p_{ij}}^2}$ while $\mu_{eff}$ and $z_b$ are parameters that depend on the geometry of the medium and its optical properties as described in detail in Ref. [33]. The semi-analytical expression given for $G_{ij}$ in Equation 11 describes the fluence at a point inside the turbid medium indexed j when a point source indexed i is illuminating the medium on the boundary. This model provides a fast semi-analytical framework for finding the Green's functions of the excitation and

emission diffusion equations. However, it is limited to optically homogeneous media and cannot perform optimally when strong heterogeneities are present.

Statistical methods have also been used to obtain the Green's functions of the diffusion equation. The most prominent statistical technique for photon transport in turbid media is the Monte Carlo method [34] where random trajectories of photons are traced until they either exit the medium at the boundary or get completely absorbed. This is continued until the required counting statistics are collected and solutions or data, with statistically low error, are simulated. While effective in modeling complex dynamics such as photon transport in highly scattering media, the Monte Carlo method is computationally very costly and is only used in cases where faster alternatives are not available, *e.g.*, higher order approximations to RTE or complex heterogeneous media [34].

Numerical methods for solving the diffusion PDEs are the most commonly used approach for finding the Green's functions in FT. Finite element method (FEM) [29, 35] provides a fast, stable platform for solving the FT forward problem and it can be applied to heterogeneous media with arbitrary geometry. In Section 1.4, FEM and its application to FT are described in detail.

## 1.4 Finite Element Formulation and Linear Model of FT

The finite element method (FEM) is the most commonly used numerical technique for solving the diffusion PDE in optical tomography [2, 6, 29]. In this method, the volume of the medium is discretized by a triangular (for 2D geometry) or a tetrahedral (for 3D geometry) mesh. Using the Galerkin formulation of FEM [29], piecewise linear functions centered on the nodes of the mesh are employed to establish a

basis for approximating the fluence and the source functions defined within the volume of the medium [29, 36]. Mathematically, the fluence function $\Phi(\mathrm{r})$ is approximated by the finite element (FE) basis functions denoted $\psi_\mathrm{j}$ , $\mathrm{j} = 1, \dots, \mathrm{N}$, (where N is the number of mesh nodes and hence the number of basis functions) as follows

$$\Phi^{\mathrm{h}}(\mathrm{r}) = \sum_1^{\mathrm{N}} \Phi_\mathrm{j}\psi_\mathrm{j}\,(\mathrm{r}), \tag{12}$$

where $\Phi_\mathrm{j}$ denotes the weight of the j-th basis function $\psi_\mathrm{j}(\mathrm{r})$ in the expansion, and $\Phi^{\mathrm{h}}(\mathrm{r})$ is the projection of $\Phi(\mathrm{r})$ onto the space spanned by the FE basis function. In applying the Galerkin approach to diffusion equation, the weak formulation of Equation 7 can be derived for each node indexed $\mathrm{j} = 1, \dots, \mathrm{N}$ as below [29]

$$\int \psi_\mathrm{j}(\mathrm{r})\big(-\nabla.\,\mathrm{D}(\mathrm{r})\nabla + \mu_\mathrm{a}(\mathrm{r})\big)\Phi^{\mathrm{h}}(\mathrm{r}) = \int \psi_\mathrm{j}(\mathrm{r})\mathrm{q}(\mathrm{r}). \tag{13}$$

Integration by parts and substitution of $\Phi^{\mathrm{h}}(\mathrm{r})$ from Equation 12 transforms Equation 13 to the following discrete matrix equation [29]

$$[\mathrm{K}(\mathrm{D}) + \mathrm{C}(\mu_\mathrm{a})]\Phi = \mathrm{Q} - \beta, \tag{14}$$

where

$$\mathrm{K}_{\mathrm{ij}} = \int \mathrm{D}(\mathrm{r})\nabla\psi_\mathrm{i}(\mathrm{r}).\nabla\psi_\mathrm{j}(\mathrm{r})\mathrm{d}\Omega, \tag{15-18}$$

$$\mathrm{C}_{\mathrm{ij}} = \int \mu_\mathrm{a}(\mathrm{r})\psi_\mathrm{i}(\mathrm{r})\psi_\mathrm{j}(\mathrm{r})\mathrm{d}\Omega,$$

$$\beta_\mathrm{i} = \int \psi_\mathrm{i}(\mathrm{r})\Gamma(\mathrm{r})\mathrm{d}(\delta\Omega),$$

$$\mathrm{Q}_\mathrm{i} = \int \psi_\mathrm{i}(\mathrm{r})\mathrm{q}(\mathrm{r})\mathrm{d}\Omega,$$

and $d\Omega$ and $d(\delta\Omega)$ denote the differential elements for volume and boundary of the medium. Also, $\Gamma(r)$ is the surface exitance expressed mathematically as below and simplified using Robin boundary condition [29]

$$\Gamma(\xi) = -c\, D(\xi)\hat{n}.\nabla\Phi(\xi) = \frac{c\Phi(r)}{2A}, \tag{21}$$

which when substituted in Equation 14 yields

$$[K(D) + C(\mu_a) + F(A)]\Phi = Q\,, \tag{20}$$

where

$$F_{ij} = \frac{-c}{2A}\int \psi_i(r)\psi_j(r)d(\delta\Omega). \tag{21}$$

Therefore, the expansion coefficients populated in the vector $\Phi$ can be obtained by solving the linear system expressed in Equation 20 and then substituted in Equation 12 to get $\Phi^h(r)$ that approximates the desired $\Phi(r)$. In the case of FT, where there are two coupled diffusion equations for every source position, the FE formulation yields two matrix equations as below

$$Z_e\Phi_e^{(i)} = Q_e^{(i)}, \tag{22-23}$$

$$Z_m\Phi_m^{(i)} = Q_m^{(i)},$$

where $\Phi_e^{(i)}$ ($\Phi_m^{(i)}$) and $Q_e^{(i)}$ ($Q_m^{(i)}$) are the fluence and the source vectors at the excitation (emission) wavelength, respectively, when i-th source location is used. As described in Section 1.3, in FT only one source location is illuminated at a time. The matrix $Z_e$ ($Z_m$) is the system matrix obtained from the FEM formulation at the excitation (emission) wavelength. The excitation source vector, $Q_e^{(i)}$, is non-zero only on the mesh nodes that

neighbor the i-th point source location. Equation 22 is the discrete FEM version of the forward problem and its solution for any given source location constitutes a Green's function.

The emission source vector, $\mathrm{Q}_{\mathrm{m}}^{(\mathrm{i})}$, can be mathematically expressed as follows

$$\mathrm{Q}_{\mathrm{m}}^{(\mathrm{i})} = \eta\mu_{\mathrm{fl}} diag\left(\Phi_{\mathrm{e}}^{(\mathrm{i})}\right)\mathrm{x}\,, \tag{24}$$

where for any $\mathrm{N} \times 1$ vector g, diag(g) is defined as an $\mathrm{N} \times \mathrm{N}$ diagonal matrix with elements of g populating its diagonal entries. Also, x represents the projection of fluorophore concentration function $\mathrm{c}(\mathrm{r})$ onto the FEM basis functions, and therefore lists the fluorophore concentration at each node of the mesh. Let $\mathrm{N_s}$ and $\mathrm{N_d}$ denote the number of source locations and detector locations, respectively. Hence, for every source location, there are $\mathrm{N_d}$ measurements of $\Phi_{\mathrm{m}}^{(\mathrm{i})}$ on the boundary of the medium. Let y denote the $\mathrm{N}_s\mathrm{N_d} \times 1$ vector that lists the boundary measurements of $\Phi_{\mathrm{m}}^{(\mathrm{i})}$ for all source locations $\mathrm{i} = 1, \ldots, \mathrm{N_s}$. From Equations 22, 23, and 24, it follows that

$$\mathrm{y} = \begin{bmatrix} \bar{\mathrm{Z}}_m^{-1}\eta\mu_{\mathrm{fl}} diag\left(\mathrm{Z}_e^{-1}\mathrm{Q}_e^{(1)}\right) \\ \vdots \\ \bar{\mathrm{Z}}_m^{-1}\eta\mu_{\mathrm{fl}} diag\left(\mathrm{Z}_e^{-1}\mathrm{Q}_e^{(\mathrm{N_s})}\right) \end{bmatrix}\mathrm{x}, \tag{25}$$

where $\bar{\mathrm{Z}}_m^{-1}$ is a sub-matrix of $\mathrm{Z}_m^{-1}$ that only includes the $\mathrm{N}_d$ rows that correspond to the detector locations. As a result, Equation 25 establishes a linear relationship between boundary detector measurements of emitted fluorescent signal and fluorophore distribution in the turbid medium. Considering detector noise, shot noise, and modeling errors present in FT, the linear model in Equation 25 can be expressed as below

$$\mathrm{y} = \mathrm{Mx}, \tag{26}$$

where e is the additive $N_s N_d \times 1$ error vector encompassing the modeling errors and noise, M is the $N_s N_d \times N$ system matrix (N being the number of nodes as mentioned previously) formulated in Equation 25, x is the $N \times 1$ fluorophore concentration vector, and y is the $N_s N_d \times 1$ measurement vector [37]. Solving for x in Equation 26 from measurements of y, prior knowledge of M, and statistical properties of e constitutes the inverse problem of FT.

## 1.5 Framework for Simulation and FT Numerical Studies

In this section the general simulation framework and the platform used for FT numerical studies are discussed. The simulation framework can be divided into three modules: FE mesh generation, the forward solver, and the inverse solver. The finite element mesh generation consists of 2D triangular and 3D tetrahedral mesh creation over areas or volumes with arbitrary geometry. MATLAB PDE toolbox is used for 2D triangular mesh generation and COMSOL 3D mesh toolbox is used for tetrahedral FE mesh generation. COMSOL generated meshes can be exported to MATLAB so that both triangular and tetrahedral meshes are available in the MATLAB environment.

The forward solver module used in this work is based upon the publicly available Nirfast software [38] coded in MATLAB. It simulates the propagation of light in 2D and 3D turbid media with known optical absorption and scattering using FE formulation of the diffusion equation as described in Section 1.4. In Figure 3, the diffusion of excitation and emission light in a rectangular turbid medium with two circular fluorescent blobs, which are simulated by the forward solver, are depicted. Figure 3 (a) shows the two fluorescent blobs in the turbid medium. Figures 3 (b) and 3 (d) show the diffusion of excitation light (that enters the medium from a boundary point), and Figures 3 (c) and 3

(e) show the emission of the fluorescent blobs diffusing through the turbid medium. The image in Figure 3 (d) is in log-scale and shows the diffusion of excitation light as it penetrates through the turbid medium and reaches the fluorescent blobs. As a result, the fluorescent blobs are excited and fluoresce. The emitted fluorescent radiation from these blobs diffuses through the medium as shown in the log-scale image in Figure 3 (e).

The forward problem module yields the fluence distribution of the excitation light for each source location, the Green's functions of the emission diffusion equation, and the simulated data vector. These are fed to the inverse solver module where the system matrix M is constructed and the fluorophore distribution vector x is estimated using the system matrix and the data vector. More details regarding FT inverse solvers are presented in Chapters 2 and 3.

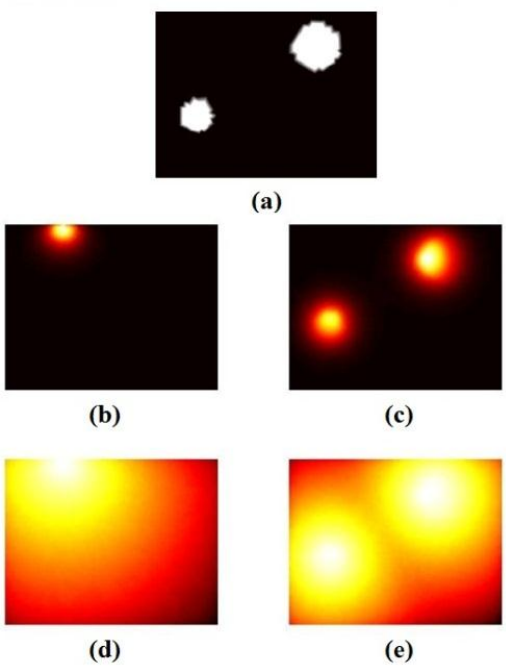


**Figure 3: A 2D FT configuration is simulated using the forward solver. a) Two circular fluorophore blobs are simulated in a rectangular turbid medium. b) Excitation light enters the medium from a boundary source point. c) Emission of the fluorescent blobs diffuses through the medium. d) Image from part (b) is plotted in log-scale. e) Image from part (c) is plotted in log-scale.**

## 1.6 FT Experimental System

While fiber-based optical tomography systems are used extensively for non-fluorescent platforms, *e.g.*, diffuse optical tomography (DOT), these systems suffer from limitations in the size of acquired data. The fiber-based systems also suffer from geometry complications as fiber tips must be in full contact with the animal surface at all times during the experiment. Free-space non-contact systems are generally preferred in FT because of their large data capacity, high speed, and efficient data acquisition. In non-contact FT, measurements are obtained using near infra-red charged coupled device (CCD) cameras focused on the animal surface. The first-generation FT system developed for this work was a cylindrical fiber-based system. Because of the limited number of measurements and calibration errors in this system, a non-contact continuous-wave (CW) trans-illumination phantom-based FT system was developed to replace the first-generation system. In Figure 4, a schematic and a picture of this second-generation experimental system are displayed.

The non-contact FT system developed in this work consists of a light-generation chamber and an imaging chamber. The imaging chamber is housed in a completely light-tight box that prevents outside radiation from interfering with the FT data acquisition devices. This separation of light generation and imaging functions also ensures that stray light and radiation noise from the light-generation devices do not contaminate the acquired FT images. The NIR radiation from the light-generation chamber is guided to the imaging chamber through a perforation in the light-tight box and using a multimode fiber, called the source fiber, whose distal end rests on a translation stage, as shown in Figure 4 (c).

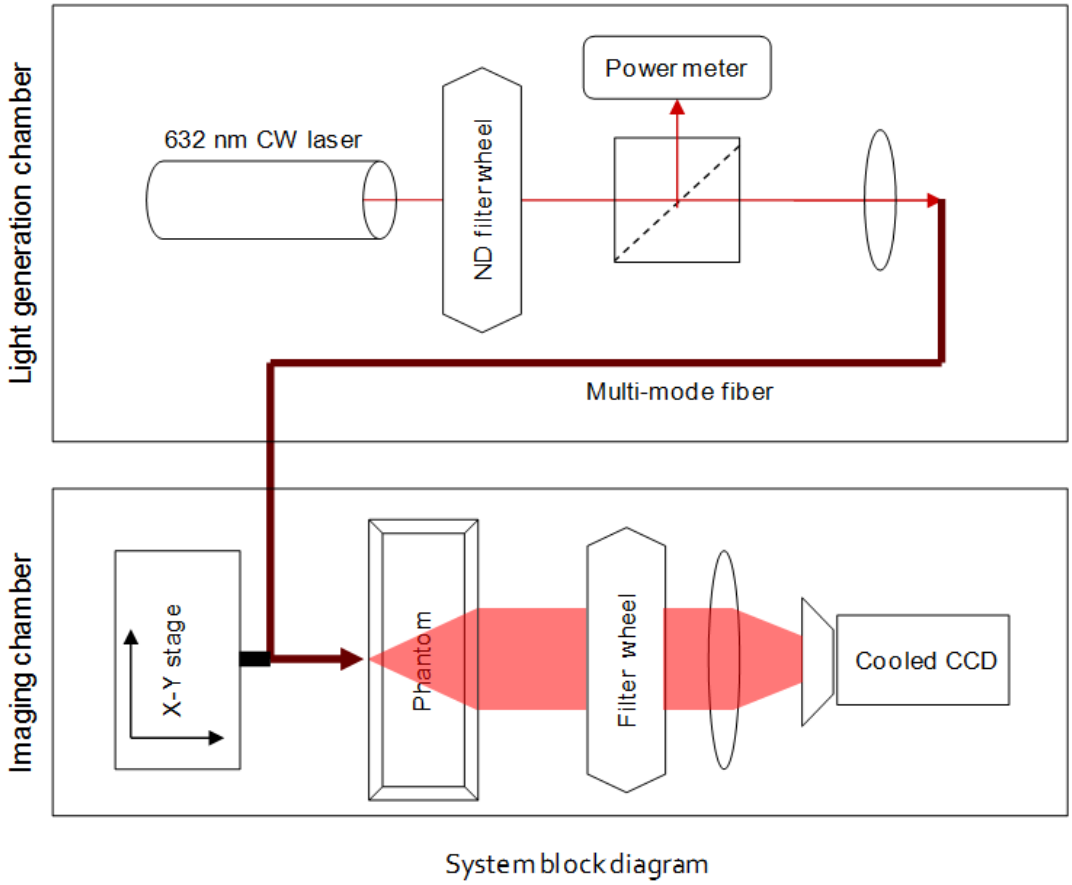


System block diagram

(a)

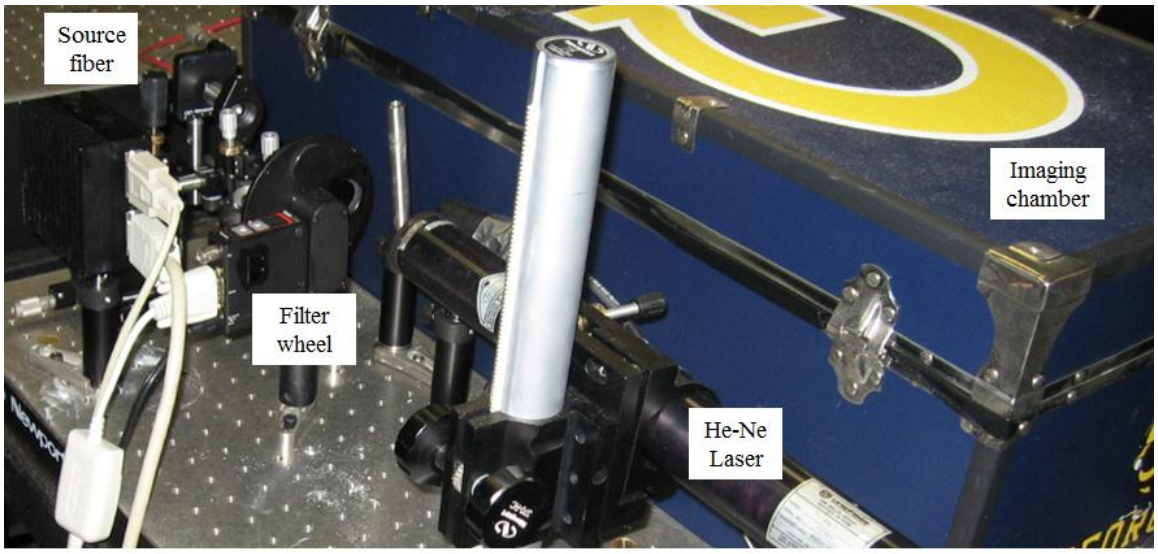


(b)

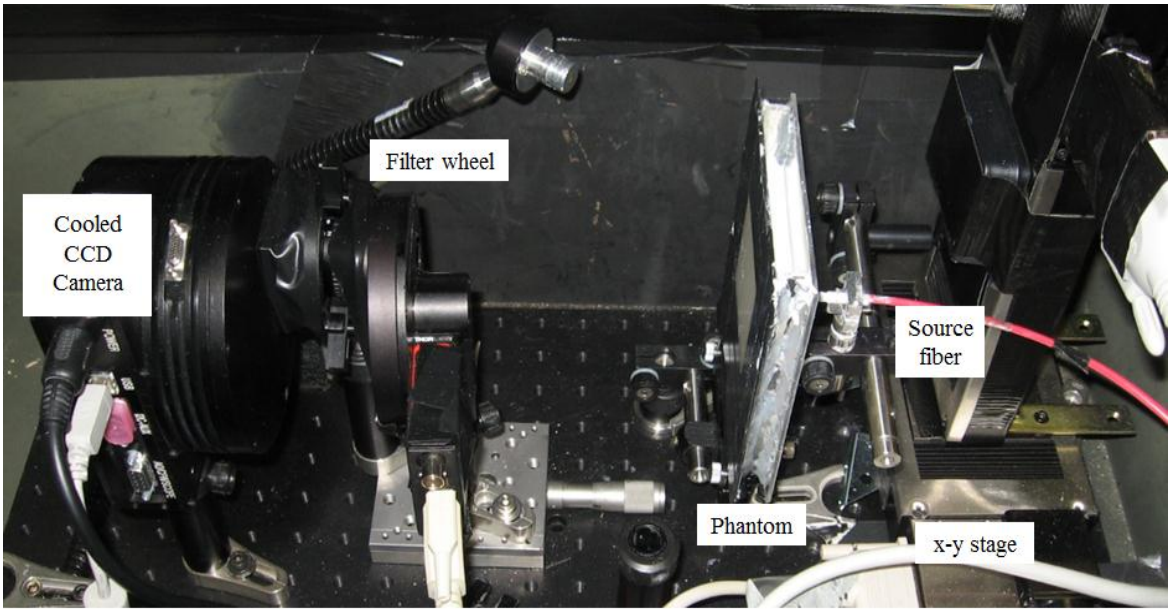


(c)

**Figure 4: A non-contact fluorescence tomography system was developed for this work. a) Outline of the FT system is depicted in a schematic. b) The light-generation section is the subsystem where laser radiation is coupled to a multi-mode fiber while attenuated by neutral-density filters and measured by a power detector. c) The imaging chamber is the section where the light from the source fiber illuminates the phantom and excites the fluorophores distributed over the volume of the phantom, and the fluorescence signal and trans-illumination of the excitation light are imaged by a cooled CCD camera.**

As shown in Figures 4 (a) and 4 (b), a Helium-Neon (He-Ne) 20 mW cavity laser produces CW light at 632 nm. The power of this NIR radiation is adjusted and measured using neutral-density filters and a power detector. The laser light is coupled into a multi-mode fiber whose distal end is mounted on a translation stage and lies in full contact with the tissue phantom. The fiber directs the laser light to a point on the phantom surface. Translation stages are used to change the position of the tip of the fiber on the surface of the tissue phantom to illuminate it at different locations and scan the source grid. The liquid phantom, which assumes the box shape of the phantom vessel, forms a slab with a thickness of 14 mm (which matches the average thickness of laboratory mice used in optical tomography experiments). As shown in Figure 4 (c), the phantom holder is a hollow box with two transparent plexi-glass sides that face one another. One side is

scanned by the source fiber and the other side is imaged by the cooled CCD camera for FT data acquisition as shown in Figure 4 (c).

Colored-glass filters mounted on a motorized filter wheel are used to allow for sequential imaging of the trans-illumination signal at the excitation wavelength, and the fluorescent signal at the emission wavelength. A 650 nm short-pass and a 700 nm long-pass filter are used for separate imaging of the trans-illumination and fluorescent signals. The cooled CCD camera captures the filtered data images. The front phantom surface is imaged to the CCD using a convex camera lens. To minimize dark-current noise, the CCD is cooled down to -10 °C, and for every captured image a closed-shutter image (dark-frame image) is also taken and subtracted from the data image. This entire imaging chamber, which houses the CCD camera and the phantom, is optically insulated in a light-tight box, as mentioned previously. The entire FT scan, which consists of scanning the source grid using the source fiber and capturing filtered trans-illumination and fluorescent images, is automated using a LabView script. The planar source scan is carried out in an automated fashion using the pair of translation stages, and the filtered image acquisition is performed automatically using the motorized filter wheel and the CCD camera. Prior to running the FT scan, a calibrated grid is placed on the phantom holder's front panel, which faces the CCD, and is imaged by the camera. The grid image is later used for selection and calibration of the data points on the acquired FT images. The setup is carefully calibrated prior to the data acquisition. The calibration process consists of several steps as shown in Figure 5. The integration times for image acquisition in the excitation and emission bands and the laser power level must be adjusted to avoid saturation in the acquired images.

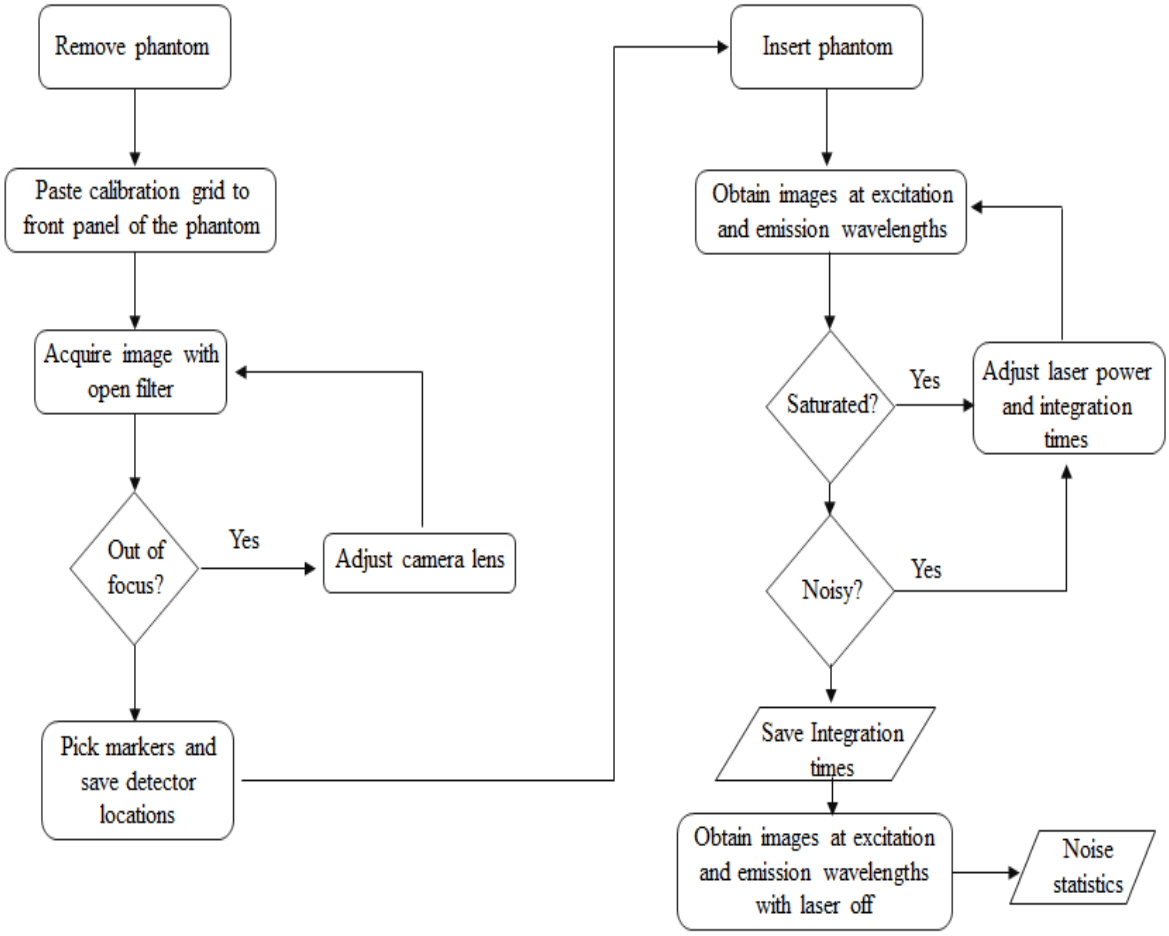


**Figure 5: The calibration process of non-contact CCD-based FT system is detailed in a flowchart.**

For precise quantification of fluorophore concentration, power loss from index mismatch, fiber coupling, and absorption and scattering in the optical components of the system must be corrected. By dividing the imaged fluorescent signal by the trans-illumination signal in a Born normalization fashion, this correction can be implemented. Since both fluorescent and trans-illumination images share the same power loss factors arising from index mismatch, fiber coupling, and optical components, these power loss factors get canceled out by dividing the fluorescent image by the trans-illumination image. The normalized images are used in the reconstruction algorithm instead of the raw

data images. With Born normalization, quantification of fluorophore concentration can be performed accurately despite unknown levels of power loss in the system [39].

## 1.7 Tissue Phantom Fabrication and Characterization

Controlled verifiable *in vivo* FT experiments are difficult to carry out because of unknown levels of modeling errors and complications associated with implanting fluorophore inclusions at fixed locations in live small animals. Instead, objects made from turbid materials that mimic the optical properties of biological tissue, called tissue phantoms, are used for testing theoretical methods and analysis of the performance of optical tomography systems. In this section, the recipe for development and the methodology for characterization of a liquid tissue phantom developed and used this work are reviewed. Tissue phantoms generally consist of a scattering or diffusive agent, an absorbing agent, and in the case of solid phantoms, a holding or hardening matrix. The holding matrix is usually either resin-based or gel-based. The scattering and absorptive agents are mixed according to proportions adjusted to achieve desirable scattering and absorption coefficients, and the holding matrix is added to harden the mixture. In the case of liquid tissue phantoms, liquid scattering and absorptive materials are used and there is no need for a hardening matrix. The main advantage of liquid tissue phantoms is their higher optical homogeneity compared to solid tissue phantoms. Also, liquid phantom recipes are very straightforward (as they mainly involve mixing two or more liquids with certain proportions) and hence easily repeatable.

The scattering agent of the liquid tissue phantom used in this work is diluted intralipid-20% fat emulsion, and the absorptive agent is India ink. Both materials are extensively used in solid and liquid tissue phantoms as they offer homogeneous optical

properties that match the optical properties of biological tissue [40, 41]. Also, intralipid has negligible optical absorption compared to India ink while India ink has almost no optical scattering. Therefore, by controlling the concentration of each agent, the optical scattering and absorption of the phantom can be adjusted. The scattering and absorption of the intralipid fat emulsion and the India ink samples used for making the tissue phantom must be measured precisely before each experiment as they may slightly differ under different conditions. Hence, a subsystem was developed in this work for systematic measurement of the optical absorption of India ink. Also, a separate subsystem was developed to measure the scattering and absorption of diluted intralipid-20% mixed with India ink. Figure 6 shows a schematic and pictures of the setup used for measurement of the optical absorption of India ink.

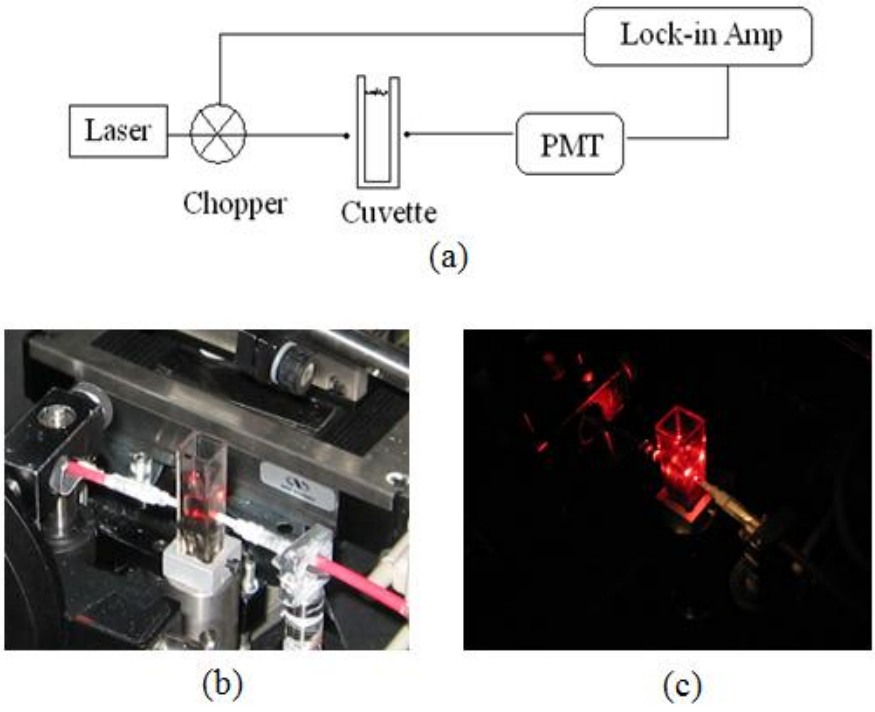


**Figure 6: Measurement of the absorption of India ink is performed using a cuvette-based setup. a) Outline of the setup is depicted in a schematic. b) Setup is imaged under normal lighting conditions. c) Setup is used under dark conditions to measure absorption.**

Water-based India ink solutions of varying concentrations are poured into a cuvette, as shown in Figure 6, and the transmittance of the laser light through the cuvette is measured. Hence, using the data points of the transmittance measurements, optical absorption of India ink is computed. These measurements indicated an absorption coefficient of 3.7 $mm^{-1}$ for a diluted 10 mL/L (1% volume concentration) solution of India ink. While optical absorption may slightly differ from sample to sample, these results are in strong agreement with previously reported results [42].

To measure the scattering coefficient of intralipid, a second subsystem was developed as shown in Figure 7. Unlike the cuvette-based setup, the system shown in Figure 7 is designed for measurement of the scattering and absorption coefficients of highly scattering low absorptive liquids. As shown in Figure 7, the fiber tips are inserted in a big tank filled with a turbid liquid. The dimensions of the tank are chosen to be very large compared to the scattering and absorption lengths and the distance between the tips of the two fibers. The propagation of the diffuse light originating from the source fiber in the medium can be approximated by diffuse photon propagation in a homogeneous infinite medium. Hence, because of radial symmetry in the 3D infinite medium, the diffusion equation is simplified to the following form in spherical coordinates,

$$\mathrm{D}\frac{\partial}{\partial \mathrm{R}^2}\,\Phi(\mathrm{R}) + \frac{2\mathrm{D}}{\mathrm{R}}\frac{\partial}{\partial \mathrm{R}}\Phi(\mathrm{R}) - \mu_a\Phi(\mathrm{R}) = \delta(\mathrm{R}), \tag{27}$$

where R represents radial distance from the tip of the source fiber and $\delta(\mathrm{R})$ is the spatial Dirac delta function that models the tip of the source fiber. As a result, the propagation of diffuse photons is given by

$$G(R) = \frac{1}{4\pi D}\frac{\exp\left(-\sqrt{\frac{\mu_a}{D}}R\right)}{R}, \tag{28}$$

where $G(R)$ denotes the Green's function of Equation 27 and models the diffusion of light from a point source (fiber tip).

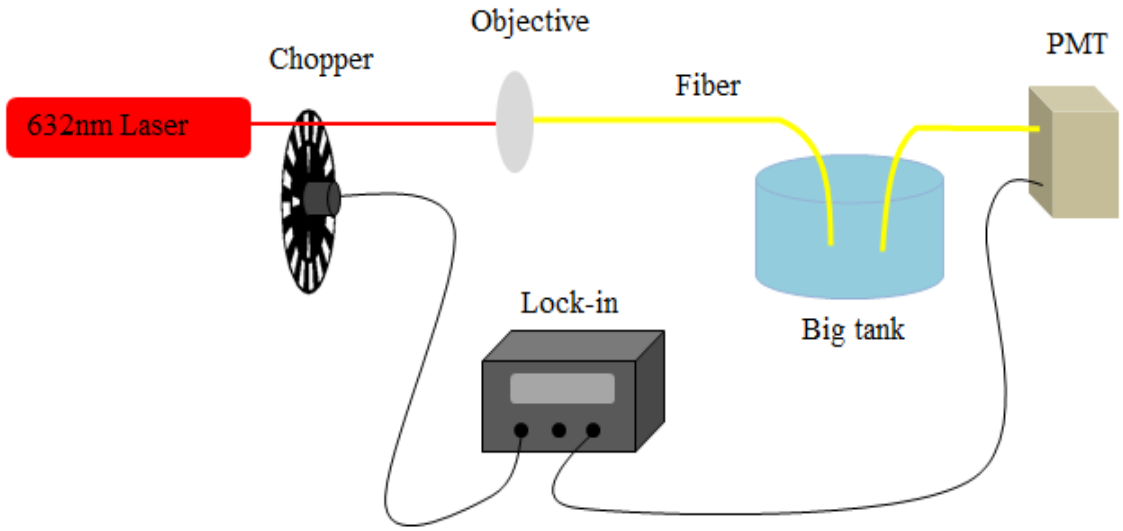


**Figure 7: Measurement of the scattering of a mixture of diluted intralipid-20% fat emulsion and India ink is performed using a lock-in amplifier-based subsystem.**

By changing the location of the source fiber and measuring the power transmitted from the source fiber to the detector fiber that is connected to a photo-multiplier tube (PMT), the rate of change in the transmitted power can be measured and therefore, the decay coefficient $\sqrt{\frac{\mu_a}{D}}$, which can be approximated by $\sqrt{3\mu_a\mu_s}$ (in highly scattering low absorptive materials) can be experimentally determined. By adding various levels of India ink to diluted intralipid-20% and performing these measurements, the decay coefficient $\sqrt{3\mu_a\mu_s}$ of the turbid mixture can be experimentally determined. Meanwhile,

the absorption coefficient of the mixture is already known as India ink particles are the dominant absorbers, and their absorption coefficient had been already determined using the cuvette-based setup depicted in Figure 6. By combining the results from the two subsystems, the scattering and absorption of intralipid-20% fat emulsion diluted to 1% and India ink are determined and can be used towards the design of the liquid tissue phantom. On aggregate, these experiments indicated a scattering coefficient of 1.05 $mm^{-1}$ for intralipid-1%. These measurements are repeated for every new sample of India ink or intralipid before using them in the phantom recipe. In addition to scattering and absorption agents, the fluorescent dyes must be placed in the tissue phantom to mimic fluorophore-tagged inclusions in tissue. A DMSO-based (dimethyl sulfoxide) 100 μM solution of Oxazine-750 perchlorate fluorescent dye is used in the phantom-based FT experiments. Oxazine-750 is excited at 633 nm, and its emission peak is around 700 nm. The excitation band and emission spectrum of this dye were determined using a fiber-based spectrometer as shown in Figure 8. The filters mounted in the filter wheel placed in front of the CCD camera are selected based on the excitation and emission bands of the dye.

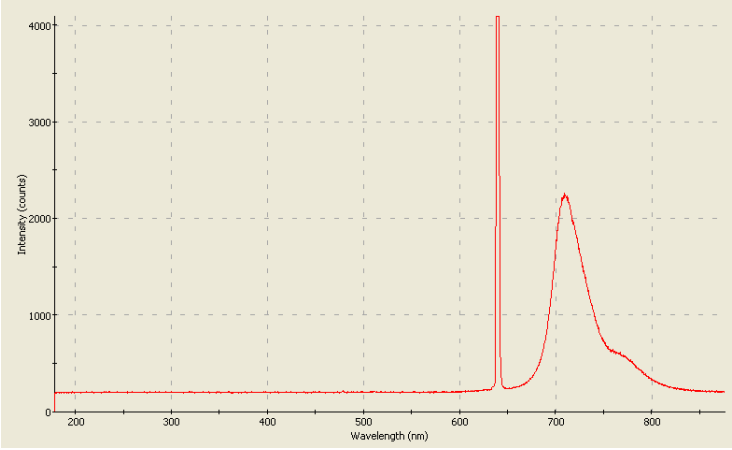


**Figure 8: Emission of Oxazine-750 dissolved in DMSO peaks around 700 nm when excited at 633 nm.**

The DMSO-based Oxazine-750 dye is inserted into thin capillary glass tubes (inner diameter of 1 mm) that are in turn inserted in the liquid phantom with vertical orientation. The configuration depicted in Figure 9 involves a pair of fluorophore-filled glass tubes suspended vertically in the phantom vessel by a crane-type structure.

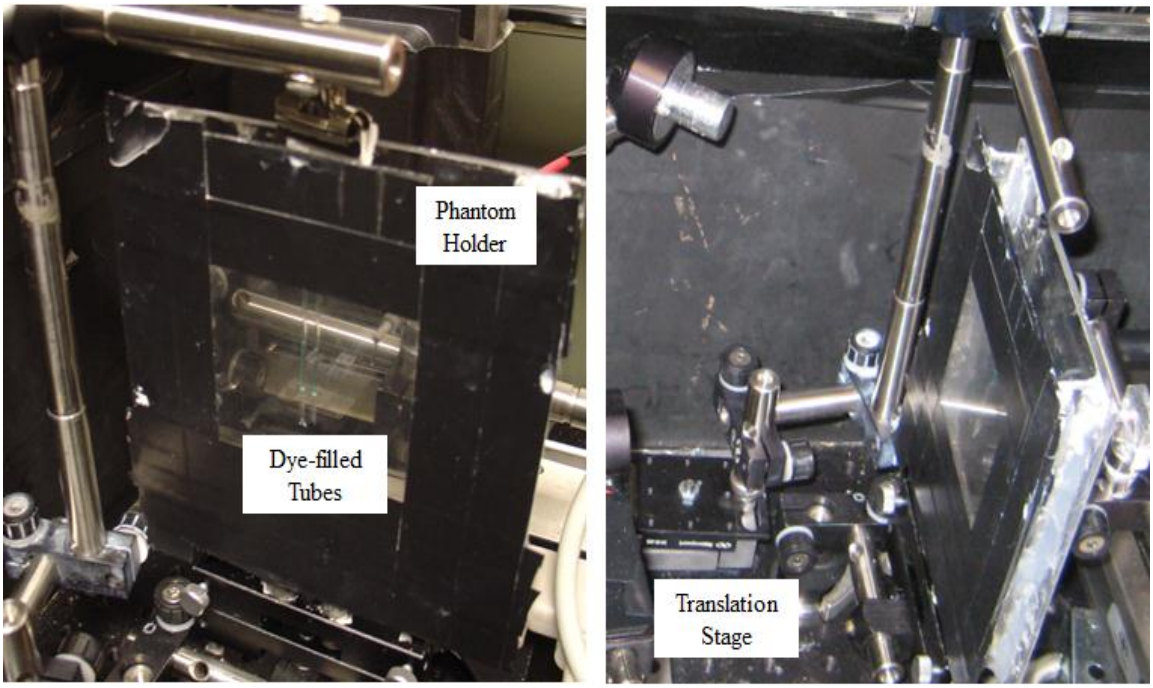


**Figure 9: A crane-type configuration is developed for insertion and suspension of fluorophore-filled tubes in the liquid phantom. a) Oxazine-filled capillary tubes are suspended using a crane-type configuration in the phantom holder. b) The crane-type configuration used for suspension of the dye-filled tubes is mounted on a translation stage.**

The crane-type configuration is used for suspension of the dye-filled tubes in the liquid tissue phantom as shown in Figure 9 (a). The crane-type structure is mounted on a translation stage as depicted in Figure 9 (b). The translation stage allows for positioning of the dye-filled tubes and adjusting their depths with respect to the front panel of the phantom vessel. After the capillary tubes are partially filled with DMSO-based Oxazine

dye, their lower ends are sealed while their top ends are attached to the horizontal optical post in the crane-type structure as shown in Figure 9 (b).

To summarize, a detailed synopsis of the experimental FT system developed in this work is listed in Table1.

**Table 1: Synopsis of the experimental FT system.**

| | |
|---|---|
| Illumination Source | 633 nm 10 mW He-Ne Laser |
| Data Acquisition | CCD cooled to -10 °C |
| Automation | Full LabView automation |
| Phantom Material | Intralipid-1% + India ink liquid phantom |
| Phantom Dimensions | 120 mm by 90 mm by 14 mm |
| Fluorescent Dye | Oxazine-750 perchlorate in DMSO |
| Total Acquisition Time | 10 minutes |
| Geometry | Non-contact trans-illumination |
| Excitation Filter | 650 nm short-pass |
| Emission Filter | 700 nm long-pass |

## 1.7 Entropy-based Analysis and Optimization

To characterize and optimize data acquisition and sampling in FT, the information content of FT datasets and their contributions to the accuracy of the 3D reconstruction must be analyzed. The configuration of the data acquisition and sampling must be optimized by maximizing the information content of the acquired data. In this section, an information-theoretic analysis of the relationship between the information content of FT data and the data acquisition and sampling configuration is presented. As discussed in Section 1.4 and formulated in Equation 26, the FT 3D reconstruction problem can be

modeled as a linear equation, and so it can be viewed as a multiple input multiple output (MIMO) system.

The input to the system is the fluorophore distribution vector x, and the output is the FT data vector y acquired by the CCD camera or the detector array. In FT, the vector x is estimated from y using the linear relationship between them. Hence, for optimal data acquisition, the level of information or certainty that y provides about x must be maximized. The concept of mutual information in MIMO systems quantifies the level of information the output of the system (or linear channel) provides about its input [43]. This concept is used to quantify the information content of FT data.

The amount of information that is transferable through a linear system can be quantified given the system matrix and noise statistics. This quantity is called the mutual information and defined as

$$I(x; y) = H(x) - H(x|y), \tag{29}$$

where for a given random vector x, $H(x)$ denotes its information-theoretic entropy, and for two random vectors x and y, $H(x|y)$ denotes their conditional entropy [43]. The mutual information is given in bits and can be interpreted as follows. Prior to observing the data vector y, there is a level of uncertainty associated with x given by $H(x)$. After observing the data vector y, some of this uncertainty is removed, thus, reducing the amount of uncertainty associated with the unknown vector x to $H(x|y)$. The amount of certainty that is obtained about the input vector after observing the data vector is defined as the mutual information denoted by $I(x; y)$. The maximum level of mutual information for a linear channel is called channel capacity and is reached when all entries of the

vector x have independent and identical Gaussian distributions. When entries of the input vector have independent identical distributions, the capacity C is given by [44]

$$C(M) = \log_2 \det(I_K + M^* M \rho_i), \tag{30}$$

where $I_K$ is the identity matrix of size K, the asterisk denotes the conjugate transpose operation, and $\rho_i$ is the input signal-to-noise ratio (SNR) formulated as

$$\rho_i = \frac{L \times E(x^* x)}{K \times E(n^* n)}, \tag{31}$$

where for a given input vector x of size K, $E(x^* x)$ is the energy of the vector, and $E(n^* n)$ is the energy level of the noise or error in the output. The input SNR $\rho_i$ differs from the data SNR or the ratio of the measurement signal energy to the noise energy. A Gaussian noise with zero mean and a variance of $\sigma_n^2$ is assumed. The total number of measurements is denoted by L, and E denotes the mathematical expectation operator.

The information-theoretic measure of capacity is applied to the linear model of FT to optimize FT data acquisition configuration [45]. While the capacity formula as given in Equation 30 can be employed, a more accurate measure is obtained by considering a more realistic probability distribution for the input signal. Equation 30 is obtained assuming a zero-mean Gaussian distribution for the input vectors. Since the fluorophore distribution cannot be negative and is between 0 and a certain maximum level, a better statistical model for the fluorophore distribution is given by the uniform distribution on the unit interval, where the maximum possible fluorophore concentration on a given mesh node is normalized to 1. Therefore, it is assumed that the fluorophore concentrations on the mesh nodes are all independent and each has a uniform probability distribution on the unit interval.

Furthermore, in real world scenarios only the measurement SNR is observable and quantifiable. Therefore, it needs to be translated to the measurement SNR, denoted here by $\rho_M$ to the input SNR, denoted by $\rho_i$. This is accomplished using the uniform probability distribution model of the vector x as follows. The measurement signal-to-noise ratio is given by

$$\rho_M = \frac{E((Mx)^* Mx)}{E(n^* n)} = \frac{E(tr(Mxx^* M^*))}{L\sigma_n^2}, \tag{32}$$

as the energy of a given column vector y can be alternatively expressed as $E(tr(yy^T))$, where tr denotes the matrix trace operator. Moving the expectation inside the trace operator the following is obtained:

$$\rho_M = \frac{tr(ME(xx^*)M^*)}{L\sigma_n^2}, \tag{33}$$

where for the uniform distribution of x, $E_x$ is given by

$$E(xx^*) = I_K/12 + U_K/4, \tag{34}$$

where $U_K$ denotes the all-one K × K matrix. Therefore, the input SNR is given by

$$\rho_i = \frac{L\rho_M}{3\, tr(ME(x^* x)M^*)}. \tag{35}$$

Substituting for $\rho_i$ is Equation 30, the following is obtained

$$C(M) = \log_2\left(\det\left(I_K + M^* M \frac{L\rho_M}{3\, tr(ME(x^* x)M^*)}\right)\right). \tag{36}$$

The expression in Equation 36 is used for quantification of the system capacity of the FT linear model. Figure 10 depicts the results of applying the system capacity notion as formulated in Equations 30 and 36 to the FT experimental system described in Section

1.6. As shown in Figure 10, while system capacity increases remarkably with SNR, saturation occurs as the detector pitch decreases below a certain limit (or the number of detectors, and hence the number of measurements, increases beyond a certain limit).

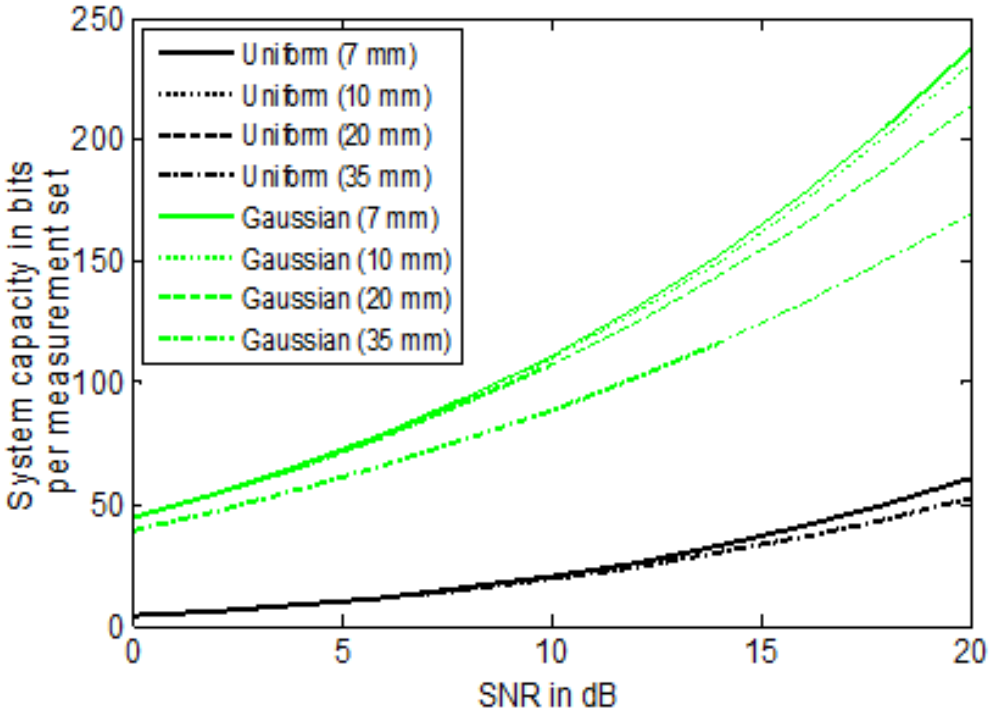


**Figure 10: The FT system capacity is plotted for various detector grid sizes versus SNR assuming a Gaussian fluorophore distribution (green curves) and a uniform fluorophore distribution (black curves).**

The saturation of information depicted in the converging curves of Figure 10 implies the saturation of the information content of FT measurements as the sampling of the data points from the surface of the phantom becomes dense. Based on this study and the presented results, the optimal sampling strategy in the FT system is to sample data points from a grid with a pitch of around 7 mm [45]. Beyond this sampling pitch, the increase in the FT data information content is merely incremental. This study renders the optimized sampling and binning for post-processing of FT data.

## 1.8 Ill-posed Nature of the FT Inverse Problem

The inverse problem in FT involves depth-resolved localization and quantification of the fluorophore distribution in biological tissue from surface measurements and therefore is a highly ill-conditioned problem by nature [2, 24]. As discussed in Section 1.4, the inverse problem in FT can be expressed using a discrete linear model formulated in Equation 26. The system matrix M has a high condition number and is ill-conditioned. For example, the condition number of the system matrix corresponding to the 2D FT scenario described in Section 1.5 is around 1.31e9. Figure 11 shows a plot of the singular values of this matrix.

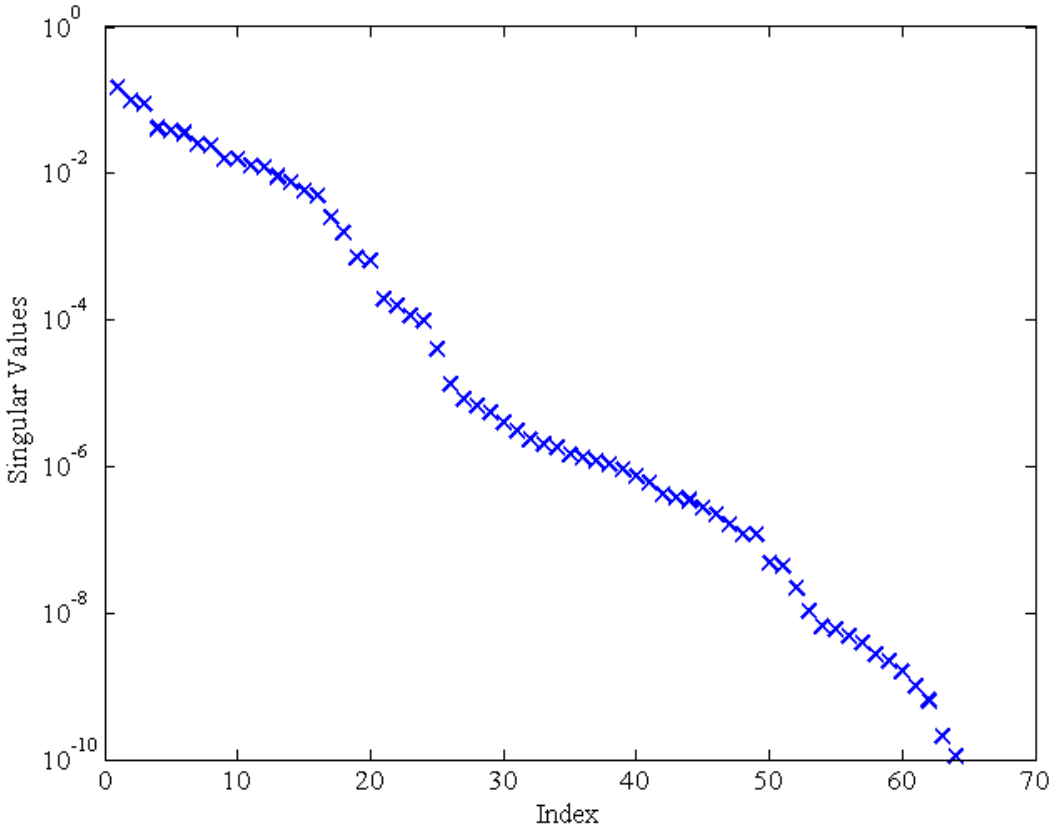


**Figure 11: Singular values of the system matrix of the 2D FT scenario described in Figure 10 (Section 1.5) are plotted in a descending order.**

The singular values of M range from 1.11e-10 to 0.147 as plotted in Figure 11. The standard procedure for solving a linear system of equations with a non-square matrix is to normalize the equation and then invert the normalized symmetric equation to obtain the least-squares solution of the problem [46, 47]. The procedure described above can be mathematically formulated as below

$$\mathrm{M}x = \mathrm{y}, \tag{37-39}$$

$$\mathrm{M}^{*}\mathrm{M}x = \mathrm{M}^{*}\mathrm{y},$$

$$x_{\mathrm{rec}} = (\mathrm{M}^{*}\mathrm{M})^{-1}\mathrm{M}^{*}\mathrm{y}.$$

When applied to the linear inverse problem of FT, accurate computation of the inverse of $\mathrm{M}^{*}\mathrm{M}$ becomes intractable because of the high condition number of M. Numerical errors, such as round-off errors, become very large in the computation of $(\mathrm{M}^{*}\mathrm{M})^{-1}$ [48]. Furthermore, modeling errors and noise, populated in the error vector e, as well as the numerical errors in the computation of $(\mathrm{M}^{*}\mathrm{M})^{-1}$, become amplified when fed through the ill-conditioned linear operator of $(\mathrm{M}^{*}\mathrm{M})^{-1}$ and create strong amplified errors and artifacts in the reconstructed fluorophore distribution vector $x_{\mathrm{rec}}$ [49]. The amplification of errors in the solution space occurs because of the extremely small singular values (or eigenvalues) of $\mathrm{M}^{*}\mathrm{M}$ which become inverted in $(\mathrm{M}^{*}\mathrm{M})^{-1}$ and turn into extremely large singular values. Therefore, when the matrix $(\mathrm{M}^{*}\mathrm{M})^{-1}$ operates on a certain vector, those components of the operand vector lying along the singular vectors that correspond to large singular values will be strongly amplified, while components lying along singular vectors that correspond to singular values with moderate values are not amplified and retain their magnitude. In the linear model of FT, similar to many discrete inverse problems [50, 51], the singular vectors that correspond to small singular

values are oscillatory and possess high-frequency behavior while singular vectors that correspond to large singular values are smooth and non-oscillatory [52]. In the context of FT, this can be explained by the dynamics of the forward problem. Highly oscillatory components of the fluorophore distribution vector have negligible contributions to the surface measurements because the opposing half cycles of the oscillatory behavior cancel each other out, but smooth and non-varying components of the fluorophore distribution contribute significantly to the surface measurements. Therefore, highly oscillatory components of a fluorophore distribution produce diminished effects on the measurements while constant or smooth components significantly affect the measurements. Conversely, the dynamics of the inverse problem are the exact opposite; the system matrix is inverted and hence the singular values are inverted. As a result, the large singular values correspond to oscillatory vectors and amplify oscillatory components in the inverse problem, and so error and noise components present in the measurements or resulting from computational limitations, which possess oscillatory behavior because of their random nature, become amplified by the inverse operator in the solution space. Therefore, noise and error components cause significant harm to the quality of the reconstructions when fed through the inverse operator. For this reason, standard non-penalized least-squares techniques do not perform optimally in solving ill-posed problems such as the FT inverse problem [53].

Various techniques have been developed to solve ill-posed inverse problems [54, 55], but the most popular and notable among them are regularization methods [56]. Regularization methods stabilize the solutions of ill-posed problems by perturbing the system matrix to diminish its singularity and decrease its condition number.

Regularization methods stabilize the condition of the inverse problem at the expense of introducing inaccuracy in system modeling and modify the singular values of the system matrix, specifically the smaller singular values as perturbations have a more significant effect on them than on the larger singular values. The inverted modified system matrix (after perturbations are introduced) does not possess large singular values that correspond to oscillatory singular vectors and so does not amplify noise and error components. In regularization techniques, the inverted linear system in Equation 39 becomes

$$x_{rec} = (M^{*}M + \lambda R)^{-1}M^{*}(y + e), \tag{40}$$

where R is a non-singular full-rank matrix and $\lambda$ is a scalar called the regularization weight (or regularization parameter) that adjusts the strength of regularization [57]. The term $\lambda R$ is the perturbation added to the normalized system matrix to filter out its small singular values. The choice of $\lambda$ and R determines the dynamics of the stability-accuracy trade-off offered by the regularization technique. The details of different regularization techniques and other inversion algorithms are discussed in Chapters 2 and 3.

# CHAPTER 2

# LEAST-SQUARES RECONSTRUCTION ALGORITHMS

## 2.1 $L_2$ Regularization

As discussed in Section 1.8, non-penalized least-squares inversion techniques do not perform optimally in FT and produce artifact-contaminated reconstructions. Hence, FT inverse solvers resort to regularization algorithms to overcome the ill-posed nature of the FT inverse problem and stabilize the reconstructions. In regularization methods, accuracy is jeopardized in favor of stability. Also, unlike non-penalized least-squares techniques where only the data fidelity term is minimized, in regularization methods, a penalty term that depends on the solution is minimized along with data fidelity to avoid error-induced impulses in the solution. Mathematically, regularization of the linear system expressed in Equation 26 can be formulated as below

$$\min_x \|y - Mx\|^2 + \lambda^2 \|Lx\|^2, \tag{41}$$

where $\lambda$ is the regularization parameter and L is the regularization matrix. The norm used for the data fidelity term, $\|y - Mx\|$, is often chosen to be $L_2$ to provide a least-squares fit to the data [58]. The norm for the penalty term, $\lambda^2\|Lx\|$, is conventionally selected to be $L_2$ in optical tomography [59, 60]. This is mainly because of the simplicity associated with solving $L_2$ regularization problems and their effective regularizing power. Regularization of the FT inverse problem using penalty terms based on other $L_p$ norms has also been a subject of study in recent years [61]. Among them, $L_1$ regularization has been shown to perform optimally in reconstruction of sparse and localized fluorescent distributions in scenarios such as early-stage cancer detection [62]. Various

implementations of $L_1$ regularization have been shown to improve 3D reconstructions in FT scenarios with sparse fluorophore distributions [62-65]. However, optimal performance of $L_1$ regularization is limited to cases with sparsity priors, and $L_1$ regularization does not generally perform well in reconstructing non-localized extended fluorescent distributions. The $L_2$ regularization is the most widely used and well-established regularization method in optical tomography. As a result, this section is devoted to the study of this regularization technique.

The $L_2$ regularization can be expressed as below

$$\min_x \|y - Mx\|_2^2 + \lambda^2 \|Lx\|_2^2 , \tag{42}$$

that is equivalent to

$$x = (M^*M + \lambda^2 L^*L)^{-1} M^*y, \tag{43}$$

where, as discussed in Section 1.8, the matrix of the normalized linear system expressed in Equation 38 is regularized by $\lambda^2 L^*L$. The addition of $\lambda^2 L^*L$ to the normalized system matrix makes the inversion non-singular and stable. Choice of the regularization matrix L and the regularization parameter $\lambda$ determines the dynamics and strength of the regularization. Conventionally, L is chosen to be the identity matrix [28, 58] unless spatially non-uniform regularization is desired. Meanwhile, $\lambda$ is adjusted to yield an appropriate level of regularization. Optimal selection of $\lambda$ is critical to the successful performance of $L_2$ regularization as it determines the cut-off below which singular values are considered too small and are filtered out to stabilize the inverse problem [58]. If $\lambda$ is too large, then the problem is over-regularized and its accuracy is excessively jeopardized. If $\lambda$ is too small, then the problem is under-regularized, and the

reconstructions are still noisy and artifact-contaminated since the inverse operator is still ill-conditioned and not fully stabilized. Therefore, finding the optimal λ is crucial to the optimal performance of $L_2$ regularization.

## 2.2 L-curve

As discussed in Section 2.1, optimal selection of the regularization parameter λ plays a key role in the successful performance of $L_2$ regularization. In problems where noise or error statistics are known *a priori*, λ can be determined based on Morozov's discrepancy principle [66]. However, the statistics of noise and errors in modeling and computation are unknown in FT. Generalized cross validation (GCV) technique is a computationally costly method that determines the optimal λ without use of error statistics [67], but this method is mostly suited for statistical estimation problems rather than large-scale inverse problems like FT. L-curve is a computationally efficient algorithm developed for optimal selection of the regularization parameter in large-scale ill-posed problems [68]. Because of its computational efficiency, L-curve is the best technique for the selection of the regularization parameter in FT. L-curve simply graphs the accuracy-stability trade-off offered by $L_2$ regularization, as discussed in Section 2.1, and picks the optimal middle point. Figure 12 shows the L-curve for a large-scale ill-posed linear system with a condition number of $10^8$. As shown in Figure 12, the x-axis represents the data fidelity or $L_2$ norm of the residual, $\|y - Mx\|_2$, and the y-axis represents the $L_2$ norm of the solution, $\|x\|_2$. Each point on the curve corresponds to a solution of $L_2$ regularization applied to the linear system using the regularization weight labeled on the curve at that point. For example, the solution of $L_2$ regularization of the linear system with a regularization weight of 5.46e-5 has a norm of around $10^9$ and a

residual norm of around $10^5$ as marked on the curve in Figure 12. The trade-off between stability (norm of the solution) and data fidelity (norm of the residual) makes the curve L-shaped, which explains the name L-curve. The middle point with the best trade-off between stability and accuracy is the corner of the L-curve which yields the optimal regularization weight. In Figure 12, the L-curve corner occurs around λ = 4.9e-5.

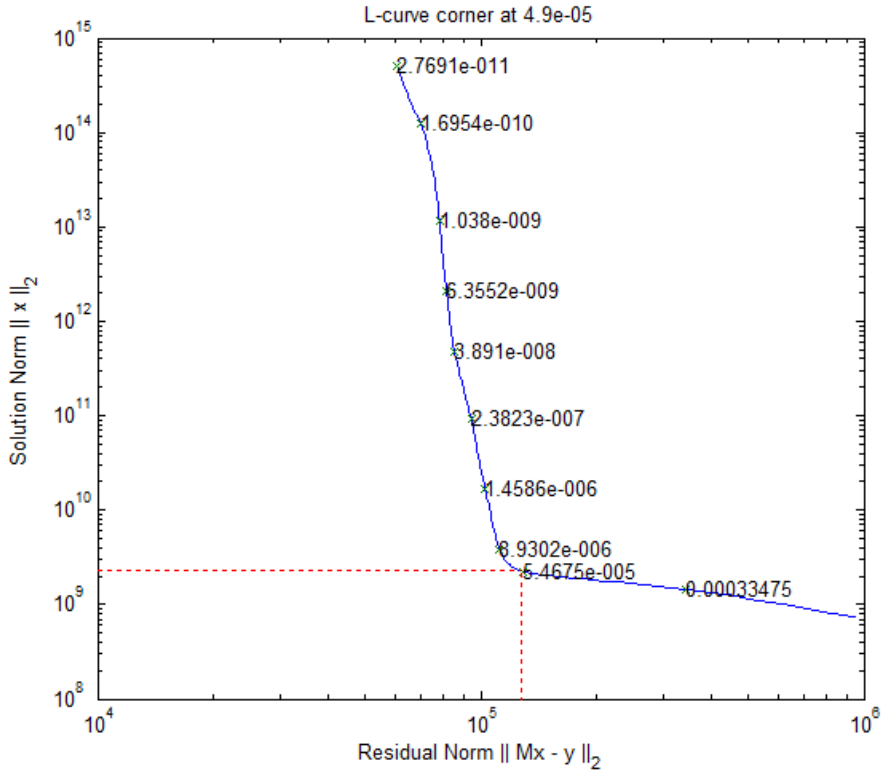


**Figure 12: The L-curve of a linear ill-posed problem is plotted to find the optimal $L_2$ regularization weight. The values on the graph represent the regularization weights that range from the smallest to the largest singular value of the system matrix (2.7e-11 to 3.3e-4).**

Obtaining the L-curve of a linear system does not require solving the $L_2$ regularization of the system for a wide range of regularization weights to obtain the solution and residual norms. It has been shown that the solution and residual norms of $L_2$

regularization with a weight of $\lambda$ can be computed using the data vector and the singular value decomposition of the system matrix as shown below [68]

$$\|x\|_2^2 = \sum_i \left( f_i \frac{u_i^* y}{\sigma_i} \right), \tag{44-45}$$

$$\|Mx - y\|_2^2 = \sum_i (1 - f_i) u_i^* y,$$

where $\sigma_i$ represents the i-th singular value of the system matrix M (when sorted in a descending order), $u_i^*$ represents the conjugate transpose of the i-th left singular vector of M, and $f_i$ is the i-th Tikhonov filter factor as below

$$f_i = \frac{{\sigma_i}^2}{{\sigma_i}^2 + \lambda^2}. \tag{46}$$

Therefore, the solution and residual norms can be computed using Equations 44 and 45 for any given regularization weight $\lambda$ by just computing the singular value decomposition of the system matrix. As a result, the computational cost of finding the L-curve of ill-posed linear systems only involves finding the singular value decomposition of the system matrix, and singular value decomposition can be performed much faster than GCV [69]. Details regarding the performance of $L_2$ regularization (with L-curve) in FT are presented in Section 2.4.

## 2.3 Algebraic Reconstruction

While regularization methods are conventionally used to overcome the ill-posed nature of inverse problems, optimal selection of the regularization parameter is needed to avoid over-regularization or under-regularization as discussed in Sections 2.1 and 2.2. Also, the computational cost and memory requirements for the numerical implementation

of regularization-based reconstruction algorithms become considerably high for large-scale problems. Iterative row-action reconstruction methods are a widely used class of memory efficient, low-cost inverse solvers that avoid bulky matrix computations in large-scale problems by iteratively updating the solution using only one equation at a time, and so only involve one dimensional vector computations [70, 71]. Of the most popular iterative row-action methods are algebraic reconstruction techniques (ART) that have recently found extensive applications in medical image reconstruction for various medical and molecular imaging modalities [72-74]. In conventional algebraic reconstruction technique, the solution is updated at each iteration through an orthogonal projection to the hyper-plane defined by the corresponding equation in the linear system of equations. Mathematically, given the system of equations defined in Equation 26, x is updated at the k-th iteration, which corresponds to the i-th row of the system of equations, as below

$$x^{(k+1)} = \min\left\|x^{k+1} - x^{k}\right\|_2 \text{ subject to } M_{i:}x^{(k+1)} = y_i\,, \tag{47}$$

where $M_{i:}$ denotes the i-th row of the system matrix M, and $y_i$ is the i-th entry in the data vector. Solving for $x^{(k+1)}$ while enforcing non-negativity (since x represents the non-negative concentration of fluorophores at each voxel) yields

$$x^{(k+1)} = x^{(k)} + \frac{y_i - M_{i:}x^{(k)}}{M_{i:}M_{i:}^{*}} M_{i:}^{*}\,, \tag{48-49}$$

$$x^{(k+1)} = \max\left(x^{(k+1)}, 0\right).$$

Equations 48 and 49 constitute the non-negative conventional ART. It has been shown that the projection access order (order at which the equations are accessed and

used for updating the solution) plays an important role in the speed of convergence in ARTs [75-77]. Multi-level scheme algebraic reconstruction technique (MLS-ART) is a modification to conventional ART where the equations are accessed in an optimal order to ensure speedy convergence [75]. The equations are considered to be optimally ordered when hyper-planes corresponding to successive equations are orthogonal to each other or intersect at close-to-perpendicular angles. After the equations are re-ordered to ensure optimal convergence, they are accessed one by one for iterative projections, and this continues until each equation has been accessed P times (usually P~10). Figure 13 provides a geometric insight into the dynamics of the MLS-ART algorithm for a 2D problem with two equations represented by the red lines. The progress of MLS-ART is represented by dark cross marks and gray arrow lines. As depicted in Figure 13, the points indicated with cross marks progress towards the solution (intersection of the two lines) with orthogonal successive projections.

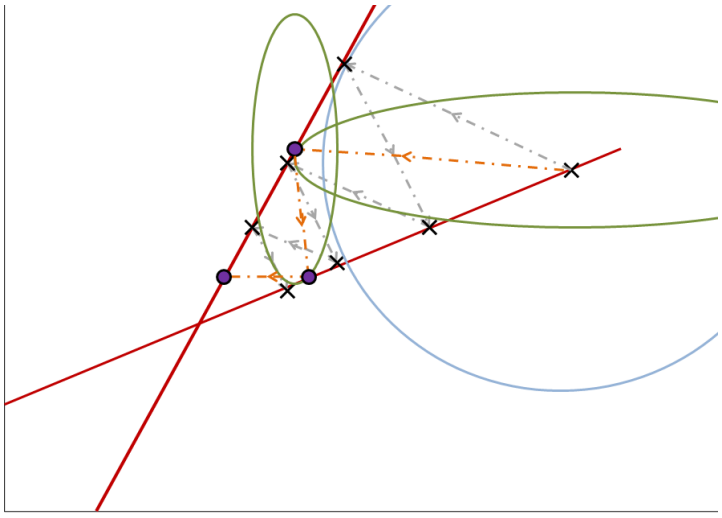

**Figure 13: A geometric interpretation is established for MLS-ART and MLS-AART. Red lines represent two linear equations in the 2D space. Gray arrows and dark x-marks show the convergence of MLS-ART. Orange arrows and violet dots show the convergence of MLS-AART to the crossing point of two lines.**

To improve the speed and performance of MLS-ART, a modification has been proposed that smartly guides the projections towards the solution and increases the speed of convergence, and geometric proximity of the result to the true solution [78]. The proposed algorithm is called multi-level scheme adaptive algebraic reconstruction technique (MLS-AART) because it adapts the projections to the updates at every iteration. In Figure 14, the violet dots and orange arrows demonstrate the progression of MLS-AART algorithm towards the solution. As depicted in Figure 13, in adaptive algebraic reconstruction the direction of the projection in each iteration is inclined towards the crossing point of the two lines, making convergence towards the true solution faster. Mathematically, at the k-th iteration of MLS-AART, corresponding to the i-th row in the linear system of equations expressed in Equation 26, the solution is updated as follows,

$$x^{(k+1)} = \min\left\|x^{k+1} - x^{k}\right\|_{X^{-1}} \text{ subject to } M_{i:}x^{(k+1)} = y_i\,, \tag{50}$$

where

$$\|x\|_{X^{-1}}^2 = x^{*}\mathrm{diag}\left(\frac{1}{x}\right)x = x^{*}\begin{bmatrix} \frac{1}{x_1} & \dots & 0 \\ \vdots & \ddots & \vdots \\ 0 & \dots & \frac{1}{x_n} \end{bmatrix}x\,. \tag{51}$$

Solving for $x^{(k+1)}$ using Lagrange multipliers [79] yields

$$x^{(k+1)} = x^{(k)} + \frac{y_i - M_{i:}x^{(k)}}{M_{i:}XM_{i:}^{*}}XM_{i:}^{*}\,, \tag{52-53}$$

$$x^{(k+1)} = \max\left(x^{(k+1)}, -x^{(k+1)}\right).$$

To illustrate the dynamics of MLS-AART, a 2D geometrical interpretation is presented as shown in Figure 13. The unit circle of the adaptive weighted $L_2$ norm,

$\|x\|_{X^{-1}}$, which is used in Equation 50, is an ellipse in two dimensions and an n-dimensional ellipsoid in higher dimensions with its longest diameter lying along the coordinate axis corresponding to the largest entry in x. When projections are ordered in a multi-level scheme to maximize the independence (or the angle) between successive equations or hyper-planes, the ellipsoid representing the unit circle of the adaptive weighted norm lies inclined towards the meeting point of the hyper-planes as shown by the green ellipses in Figure 13. As a result, MLS-AART projects the updates closer to the true solution compared to MLS-ART, which uses orthogonal projections. In Figure 13, a geometrical justification is presented to show how the convergence of MLS-AART, represented by orange arrows and violet dots, is faster than MLS-ART convergence represented by gray arrows and dark cross marks. In MLS-AART, the inclined nature of the weighted norm quickly guides the updates to the solution. In MLS-ART, the orthogonal nature of the projections can make the convergence slow particularly when the angle between successive equations is highly acute.

MLS-AART offers a fast, robust platform for solving large-scale linear systems of equations and is capable of stabilizing ill-conditioned systems because it minimizes the norm of the updates in each iteration and prevents the updates from blowing up in size. This stabilizing property and speedy convergence make MLS-AART very useful for medical image reconstruction purposes [78, 80]. However, while MLS-AART and similar row-action iterative algorithms offer stability and robustness in solving ill-posed problems, they do not possess the same level of noise robustness as regularization algorithms. As described above, ARTs possess a weakly regularizing effect. As a result, for problems or imaging scenarios involving high level of noise or error, they may not

produce robust results. More details regarding the performance of MLS-AART in FT are presented in Section 2.4.

## 2.4 Numerical and *In vivo* Studies

To investigate the performance of the inversion algorithms discussed in this chapter, they are applied to 3D numerical and verifiable dual-modality *in vivo* FT studies whose results are presented and discussed in this section. The algorithms used for performing reconstructions were $L_2$ regularization with L-curve (for parameter estimation) and MLS-AART.

The 3D numerical study is presented in Figure 14. The configuration of the simulated FT scenario involved a slab turbid medium with two AF680 spheres located in the central region. The scattering and absorption coefficients of the turbid medium were chosen to be spatially homogeneous and their values were selected to match the average optical properties of biological tissue ($\mu_a \sim 0.05\ \text{mm}^{-1}$ and $\mu_s \sim 1\ \text{mm}^{-1}$) [2]. In Figure 14 (a), the configuration and geometry of the simulated FT scenario is depicted. In Figure 14 (b), the data images are displayed. The data images are acquired at the emission wavelength (700 nm) of AF680 dye when excited at 640 nm. The source locations lie on a 10-by-8 grid. To observe the effect of the depth of the inclusions on the performance of the reconstruction algorithms, the fluorescent spheres were simulated at three different depths of 6 mm, 10 mm, and 14 mm. The forward simulation was performed by using the semi-analytical Green's function in Equation 11 on a 3D rectangular grid with a voxel size (volume) of 1 $\text{mm}^3$.

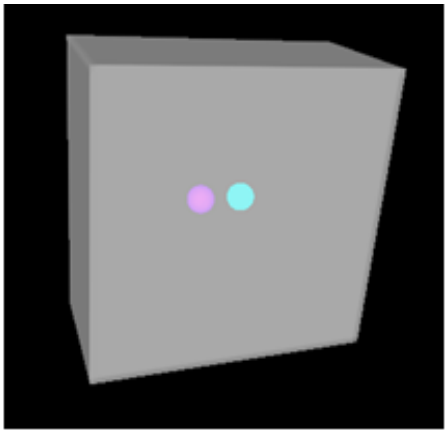

(a)

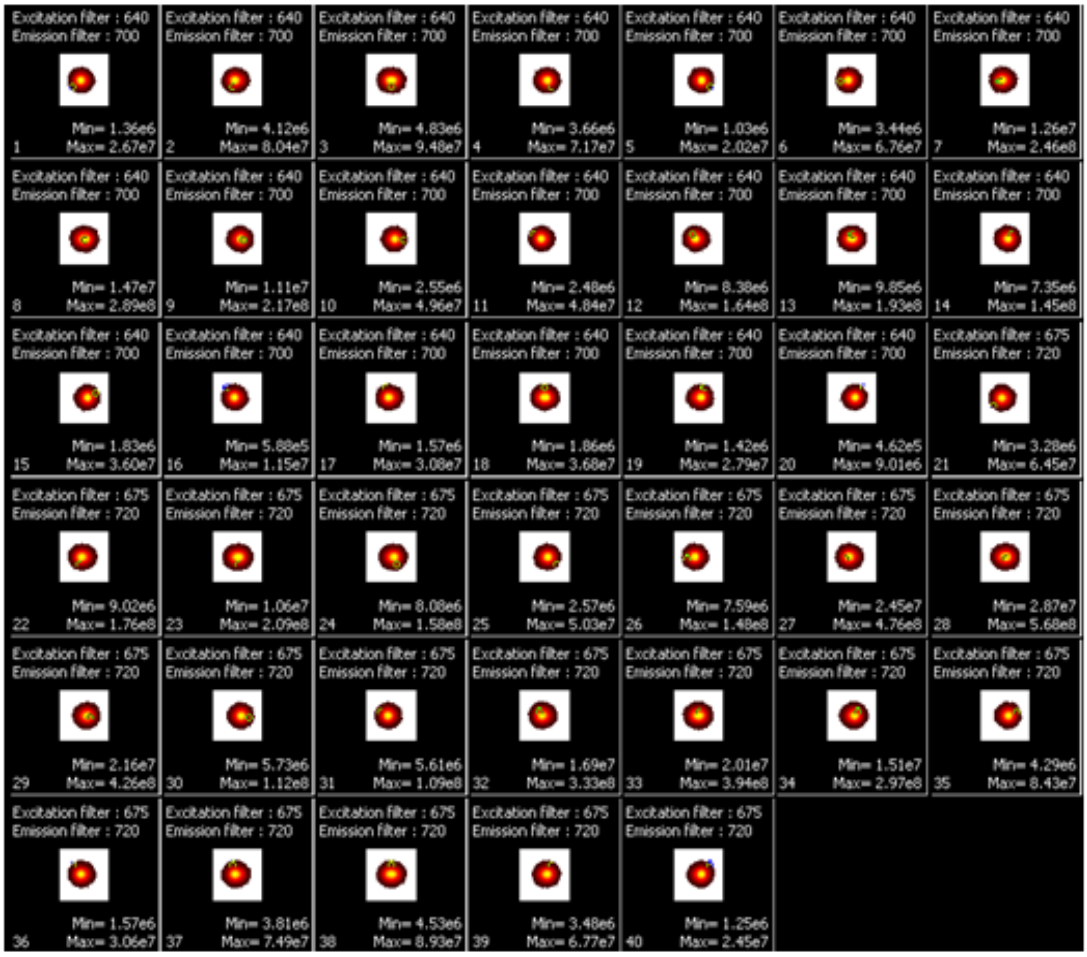


(b)

**Figure 14: In a 3D FT numerical study, two AF680 spheres buried in a turbid slab were simulated. a) The turbid box was 40 mm by 40 mm by 20 mm. The radius of each AF680 sphere was 2 mm and they were 2 mm apart. b) Data was simulated by the forward solver for 40 source locations.**

The turbid box was illuminated at 40 source locations in a trans-illumination geometry, and the surface intensity of fluorescent emission from the spheres was simulated by the forward solver for every source position. The data were contaminated with typical levels of Gaussian read-out (detector) noise and Poisson-distributed shot noise. Also, around 20% error was introduced in the optical properties estimates used in the reconstruction algorithms. Reconstructions were performed using $L_2$ regularization (with L-curve) and MLS-AART for the three numerical studies (each corresponding to a different depth). The results for the 6 mm, 10 mm, and 14 mm deep spherical inclusions are presented in Figures 15, 16, and 17, respectively. Each figure depicts the L-curve, the $L_2$ regularization reconstruction, and the MLS-AART reconstruction for the corresponding numerical study. Since the geometry and optical properties are the same for the three studies, the system matrix and the singular value decomposition are almost the same as well (they may differ slightly based on the location of sampled data points). The L-curve, however, depends on the data vector and therefore differs in each case as shown in Figures 15 (a), 16 (a), and 17 (a).

The reconstructions for the shallow-depth case (6 mm) are depicted in Figures 15 (b) and 15 (c). Both $L_2$ regularization and MLS-AART successfully reconstruct the two inclusions. However, the $L_2$-regularized reconstruction is over-smoothed and possesses over-spreading as shown in Figure 15 (b). Additionally, MLS-AART reconstruction has sporadic artifacts throughout the volume of the turbid box as depicted in Figure 15 (c). The over-spreading of the $L_2$ regularization is expected based on the discussions presented in Sections 2.1 and 2.2. The corner of the L-curve, as shown in Figure 15 (a), is considerably close to the highest singular value of the system matrix. Therefore, L-curve

selects a large regularization parameter and the reconstruction is strongly regularized, so a wide range of oscillatory singular vectors is damped out. As a result, the reconstruction possesses spreading as it lacks high-frequency components.

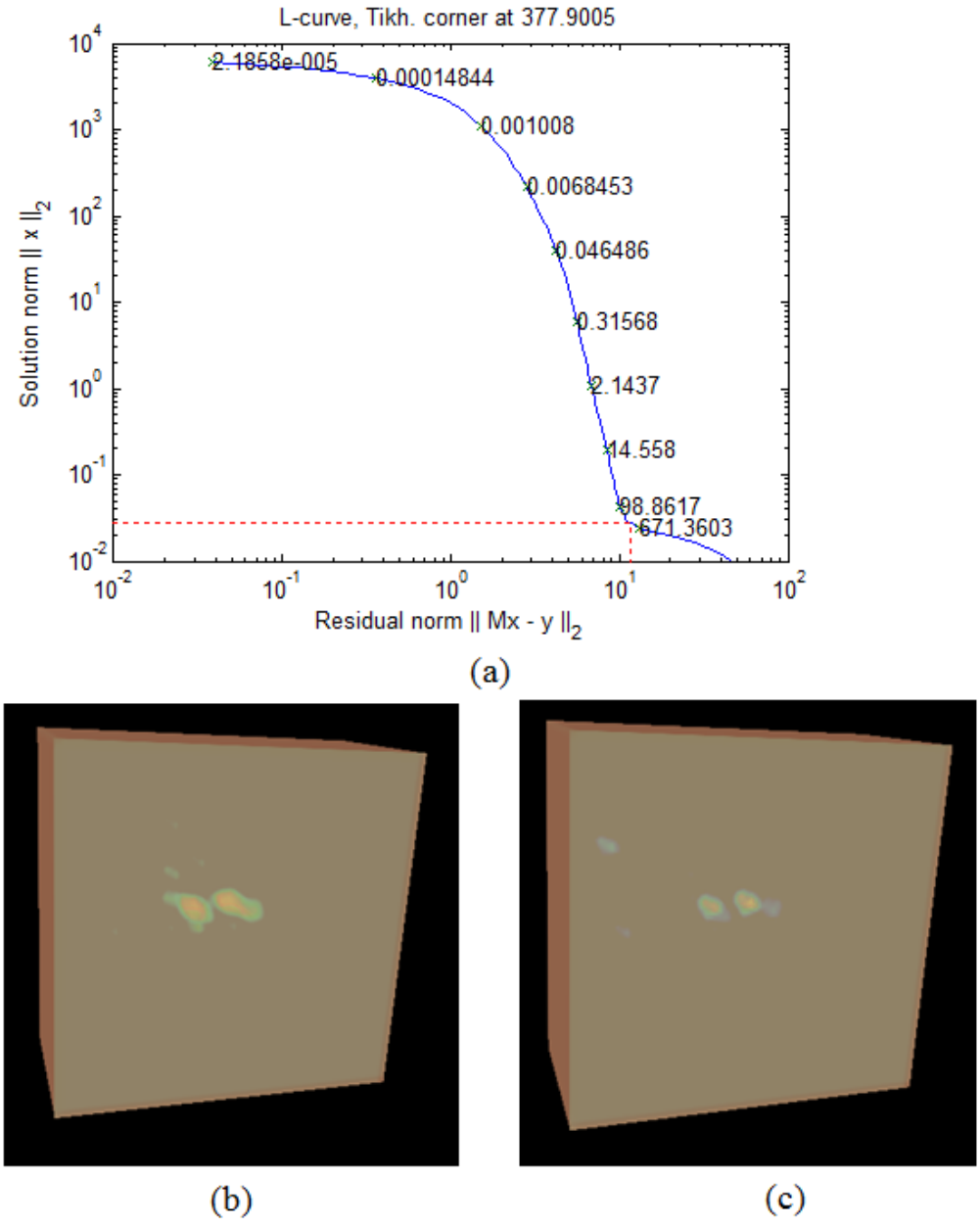


**Figure 15: 3D reconstructions were performed by $L_2$ regularization and MLS-AART for the case of double spheres buried at 6 mm. a) L-curve was plotted to select the regularization parameter λ=378. b) 3D reconstruction was performed using $L_2$ regularization. c) 3D reconstruction was performed using MLS-AART.**

MLS-AART reconstruction, as depicted in Figure 15 (c), has less spreading and is better localized around the corresponding depth of the inclusions, however, the reconstruction possesses artifacts scattered within the volume of the turbid medium. As discussed in Section 2.3, MLS-AART converges to a weakly regularized (owing to the norm minimization at every step) solution and is not as noise-robust as $L_2$ regularization. Therefore, while MLS-AART reconstructs the high-frequency components, it does not damp out noise-induced artifacts and errors. Figure 15 (c) shows how the reconstruction by MLS-AART is well-localized but possesses artifacts.

As the depth of the spheres increases, stronger regularization is required as shown in the L-curves depicted in Figures 15 (a), 16 (a), and 17 (a). This is expected because photons from deeper sources are more diffuse, and reconstructing deep sources suffers from poorer conditioning compared to reconstructing shallow sources, and requires stronger regularization. Increasing the regularization strength results in more spreading in the reconstructed inclusions. This can be observed in the $L_2$ regularization reconstructions depicted in Figures 15 (b), 16 (b), and 17 (b). As the depth of the inclusions increases, the L-curve corner value and the regularization parameter value rise, and as a result, the over-spreading in the reconstructed inclusions increases. Meanwhile, MLS-AART does not possess strong regularizing power and so its reconstructions, as shown in Figures 15 (c), 16 (c), and 17 (c), are better localized around the corresponding depths compared to $L_2$ regularization. However, as the depth of the inclusions increases, which makes the problem more poorly conditioned, the level of error-induced artifacts in the MLS-AART reconstructions rises which impairs the quality of the reconstructions. Overall, the 3D

numerical studies indicate that MLS-AART has a stronger resolving power and a weaker regularizing or stabilizing power compared to $L_2$ regularization.

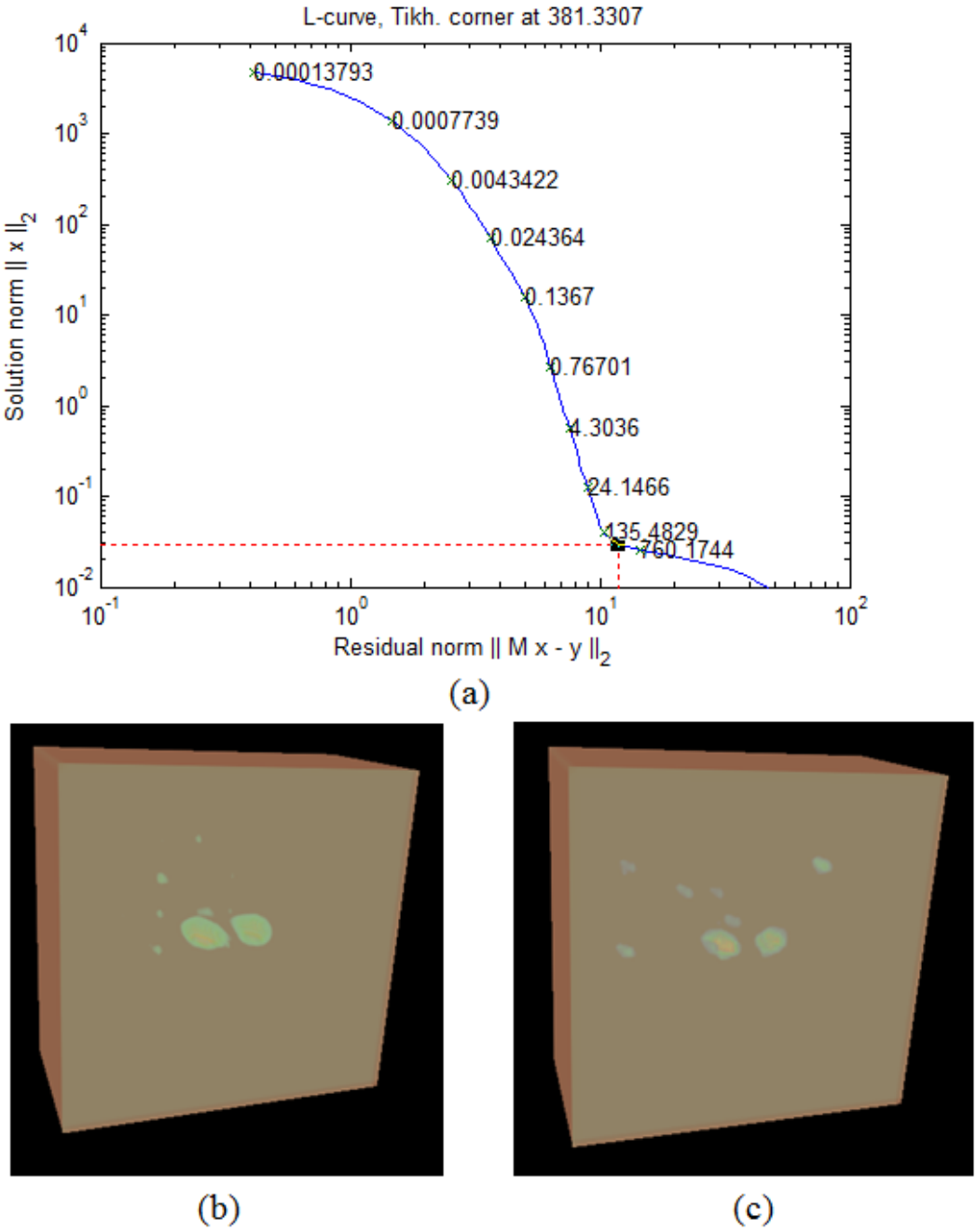


**Figure 16: 3D reconstructions were performed by $L_2$ regularization and MLS-AART for the case of double spheres buried at 10 mm. a) L-curve was plotted to select the regularization parameter λ=381. b) 3D reconstruction was performed using $L_2$ regularization. c) 3D reconstruction was performed using MLS-AART.**

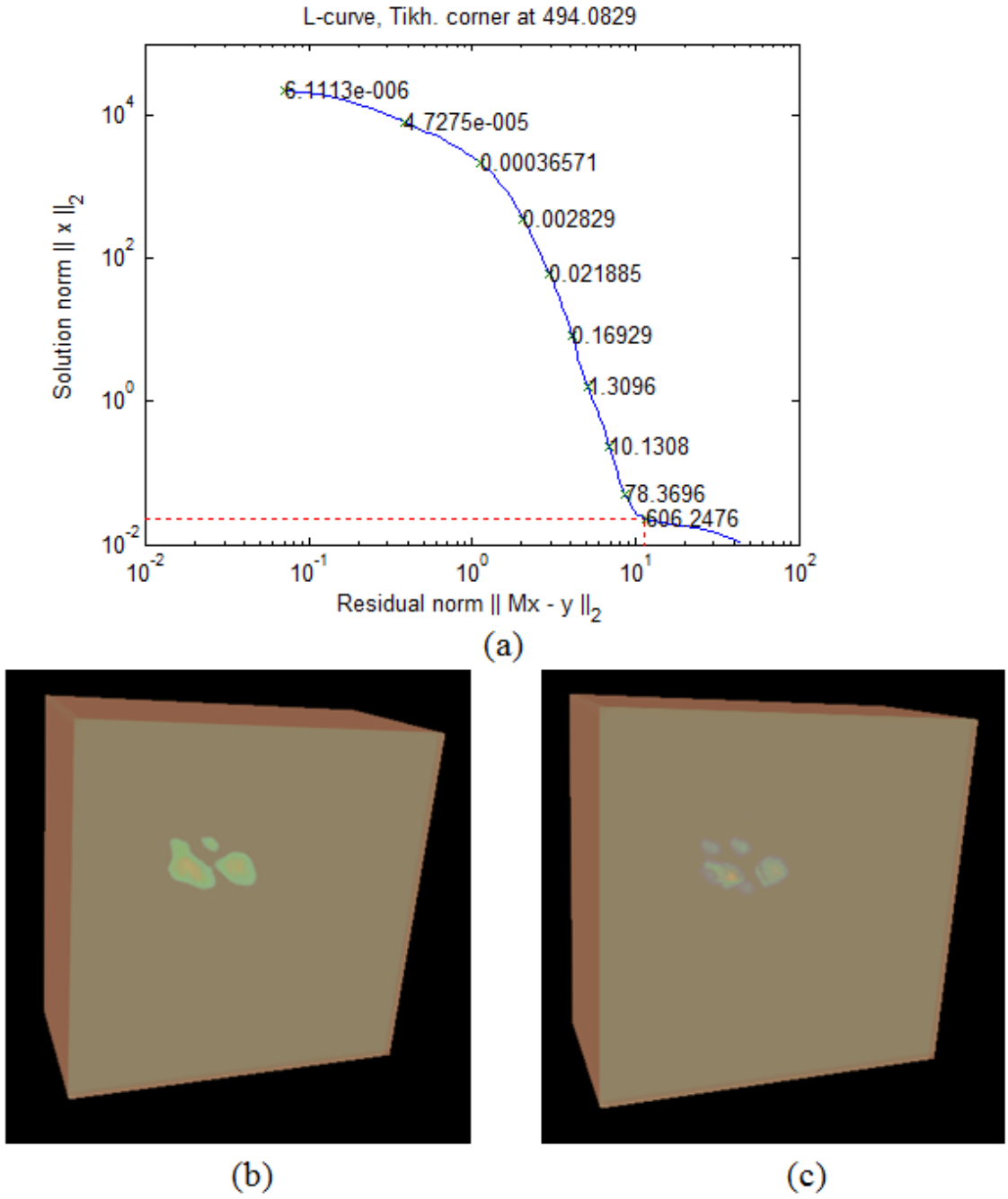


**Figure 17: 3D reconstructions were performed by $L_2$ regularization and MLS-AART for the case of double spheres buried at 14 mm. a) L-curve was plotted to select the regularization parameter λ=494. b) 3D reconstruction was performed using $L_2$ regularization. c) 3D reconstruction was performed using MLS-AART.**

To study and compare the performance of the conventional reconstruction algorithms presented in this chapter in *in vivo* scenarios, they are applied to two verifiable FT/CT dual-modality *in vivo* studies. As discussed in Section 1.2.6, *in vivo* studies involving labeled cancer tumors or test drugs cannot be used for studying the performance of FT reconstruction algorithms as the actual distribution of the administered fluorophores cannot be known precisely. Therefore, the quality of the reconstructions cannot be assessed. The fluorescent inclusions used in the verifiable *in vivo* studies were selected to be glass tubes filled with AF680 fluorescent dye and surgically implanted inside laboratory. The implants can be imaged in a dual-modality CT/FT platform as shown in Figure 18. The implant tubes can be segmented out from the soft tissue surrounding them in the 3D CT reconstructions as they are made of glass which includes elements that have higher atomic numbers than elements in soft tissue (Si=14 versus C=6, N=7, and O=8). The 3D CT reconstruction yields a high resolution 3D map of the location of the fluorophore-filled tubes. When co-registered with the 3D FT reconstruction, the CT map can be used for verification of the accuracy of the FT reconstruction. Figure 18 (a) depicts the 3D CT reconstruction of a nu/nu mouse with two cylindrical AF680-filled glass tubes surgically implanted in its intestines. The ventral side of the mouse is imaged by a trans-illumination CCD-based FT system, while the dorsal side is illuminated serially at 30 source locations as depicted in Figure 18 (b). The restraining bed used for housing and transporting the animal has fiduciary markers that are imaged by the CT system and are fixed within the coordinates of FT images. These markers are used for a fast automatic co-registration of the 3D CT map and FT reconstruction. The two *in vivo* studies presented in this section involved a pair of

cylindrical AF680-filled tubes surgically implanted in the intestines of a nu/nu mouse at different depths (3 mm and 6 mm) and imaged by a dual-modality FT/CT system.

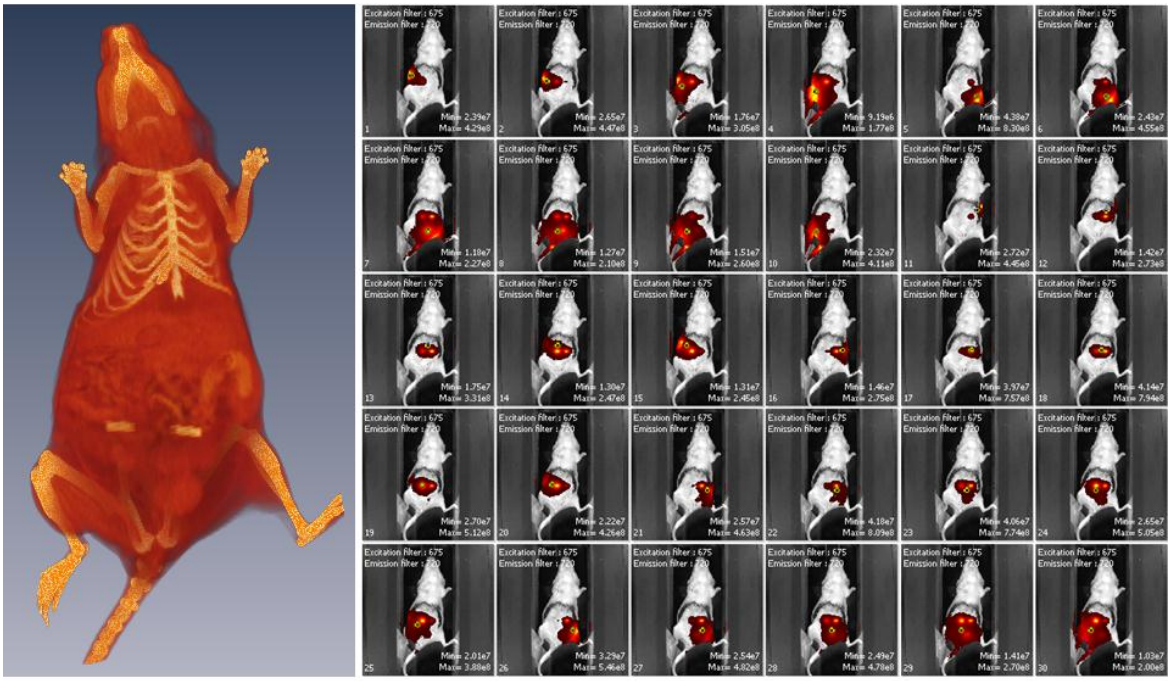


**Figure 18: Dual-modality verifiable FT/CT *in vivo* studies are performed on a nu/nu mouse. a) 3D X-ray CT reconstruction reveals the fluorophore-filled (AF680) implant tubes in the intestines of the nu/nu mouse. b) FT data are acquired using a trans-illumination CCD-based system at 30 source locations.**

Reconstructions by $L_2$ regularization and MLS-AART for the two *in vivo* studies are presented in Figures 19 and 20. The optical properties used in the reconstruction algorithms for the intestines of the nu/nu mice were statistical estimates derived from multiple measurements performed on nu/nu mice [33]. L-curves were plotted for the two studies to determine the corresponding optimal regularization parameters as shown in Figures 19 (a) and 20 (a). Similar to the numerical studies presented in this section, the singular value decomposition of the system matrices corresponding to the two *in vivo* scenarios are very similar as shown in the L-curves in Figures 19 (a) and 20 (a) because

of the similarity between the configurations and optical properties of the two experiments. Moreover, the value of the regularization parameter for the experiment with deep implants (6 mm) is higher than that of the experiment with shallow implants (3 mm).

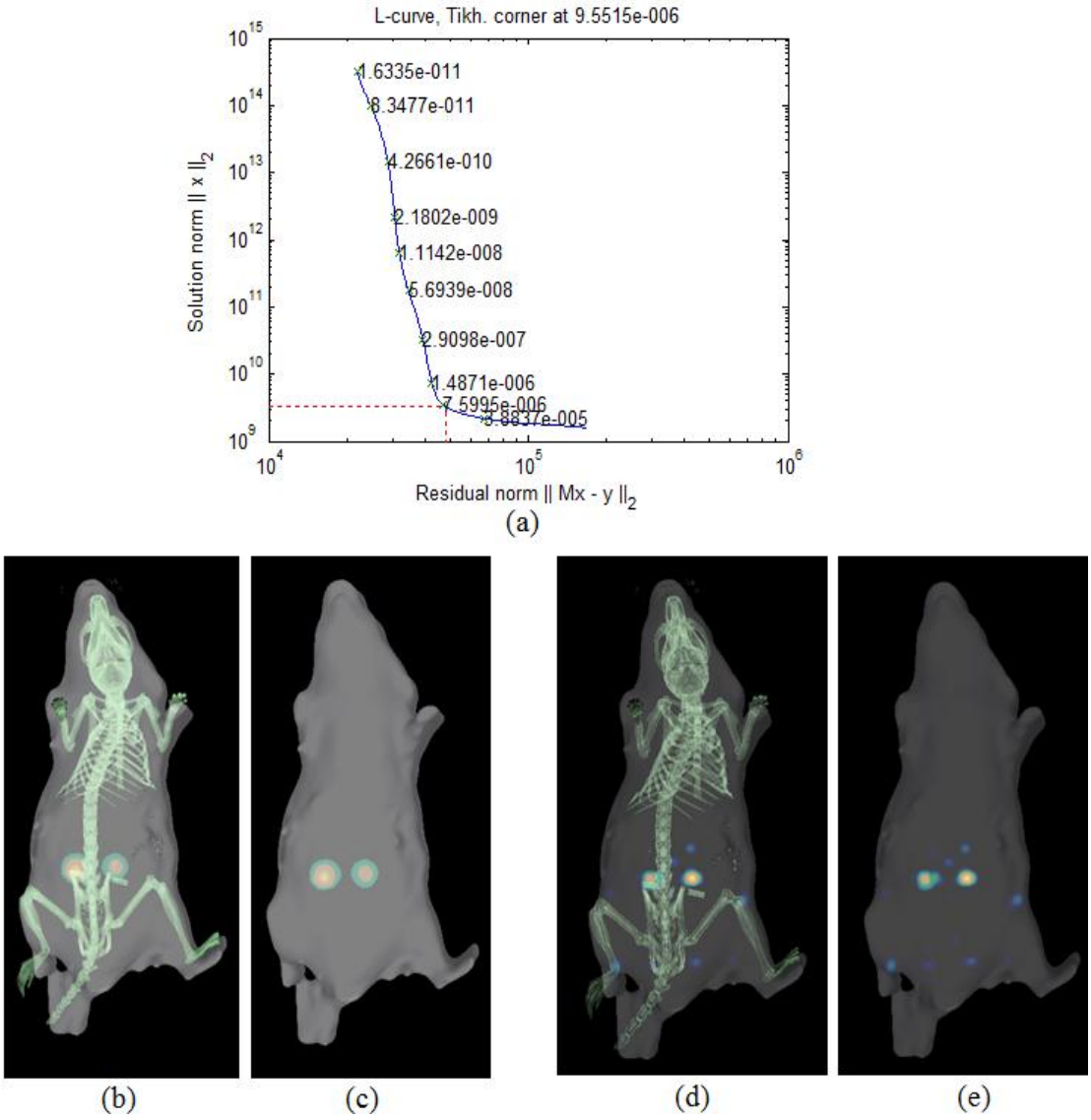


**Figure 19: Dual-modality FT/CT *in vivo* study is performed on a nu/nu mouse with two cylindrical AF680-filled tubes implanted 3 mm deep in the intestines. a) L-curve is plotted to select the regularization parameter λ=9.55e-6. b) $L_2$ regularization FT reconstruction is overlaid with co-registered 3D CT map. c) FT reconstruction is performed by $L_2$ regularization. d) MLS-AART FT reconstruction is overlaid with co-registered 3D CT map. e) FT reconstruction is performed by MLS-AART.**

$L_2$ regularization reconstructions are depicted in Figures 19 (c) and 20 (c), and MLS-AART reconstructions are shown in Figures 19 (e) and 20 (e). Meanwhile, to verify the accuracy of the reconstructions, they are overlaid with the co-registered CT maps that indicate the exact location of the implants. Figures 19 (b) and 20 (b) depict the $L_2$ regularization reconstructions overlaid with the corresponding CT maps, and Figures 19 (d) and 20 (d) show the MLS-AART reconstructions overlaid with the 3D CT maps. The $L_2$ regularization reconstructions contain two inclusions and do not possess any artifacts since the regularization parameters picked by L-curve are relatively large in both cases. These reconstructions are both strongly regularized, and the reconstructed inclusions possess over-smoothing and over-spreading as shown in Figures 19 (b) and 20 (b). As described in Sections 2.1 and 2.2, the accuracy of reconstructed inclusions is jeopardized in $L_2$ regularization to avoid noise-induced artifacts. Conversely, the MLS-AART reconstructions are contaminated with artifacts in both cases. In the shallow (3 mm) case, the inverse problem is less ill-conditioned than the deep (6 mm) case. Hence, the level of artifacts present in the MLS-AART reconstruction from the shallow scenario is much less than the deep scenario. As shown in Figures 19 (d) and 19 (e), the two implants reconstructed by MLS-AART are relatively well-localized around the corresponding tubes visualized in the co-registered CT map. The MLS-AART reconstruction has some sporadic artifacts distributed within the volume of the mouse, but they are not as bulky or intense as the reconstructed inclusions. However, in the deep (6 mm) scenario, the MLS-AART reconstruction is highly artifact-contaminated and possesses poor accuracy as shown in Figures 20 (d) and 20 (e). As discussed in Section 2.3, MLS-AART provides well-resolved accurate reconstructions in scenarios with low error or noise. However, it

fails to perform accurately as the noise and error levels in the data and the model increase. This failure is primarily due to the weakly regularizing nature of MLS-AART. Overall, the *in vivo* studies show that both reconstruction algorithms perform relatively accurate in reconstructing shallow inclusions, but the reconstructions become either artifact-contaminated or poorly resolved for deep inclusions.

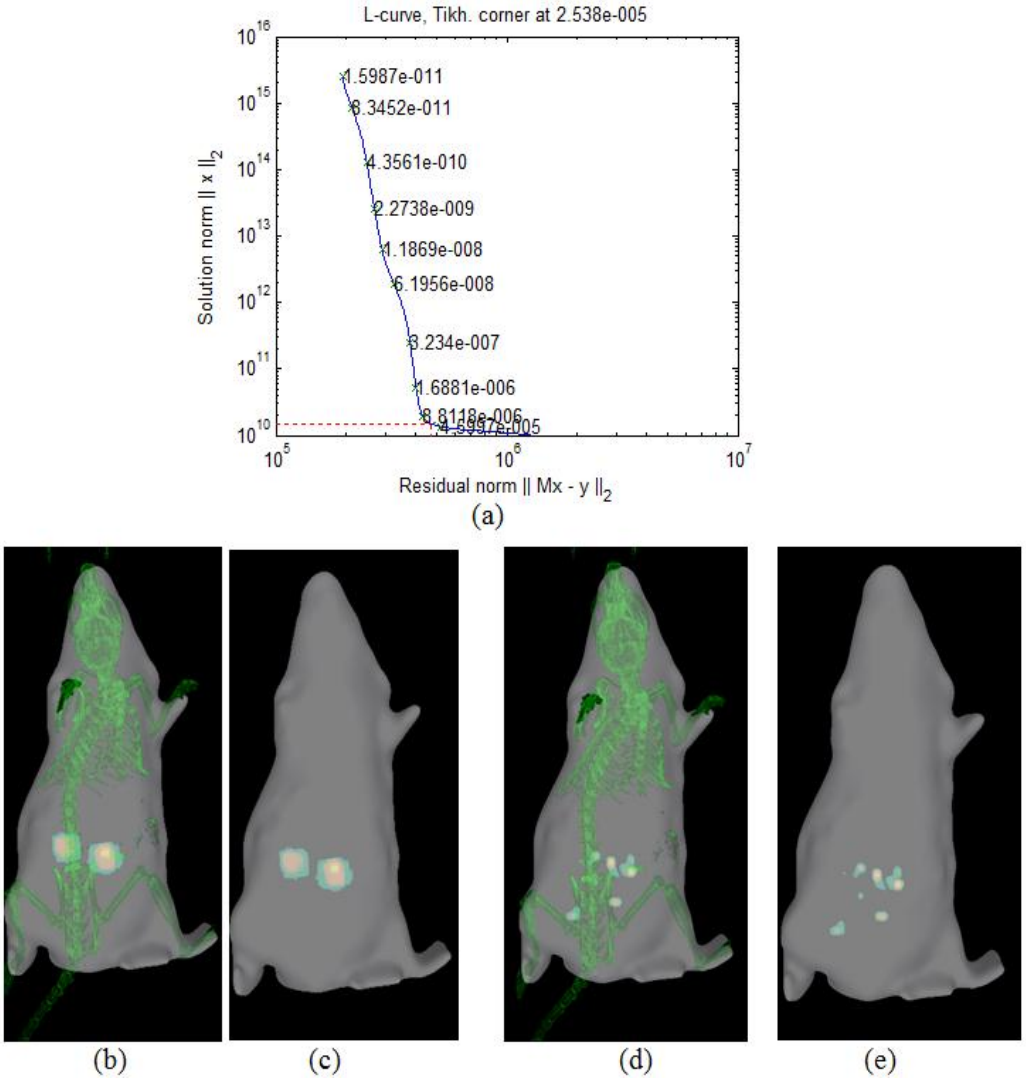


**Figure 20: Dual-modality FT/CT *in vivo* study is performed on a nu/nu mouse with two cylindrical AF680-filled tubes implanted 6 mm deep in the intestines. a) L-curve is plotted to select the regularization parameter λ=2.53e-5. b) $L_2$ regularization FT reconstruction is overlaid with co-registered 3D CT map. c) FT reconstruction is performed by $L_2$ regularization. d) MLS-AART FT reconstruction is overlaid with co-registered 3D CT map. e) FT reconstruction is performed by MLS-AART.**

## 2.5 Limitations and Drawbacks

Based on the results and discussions presented in Section 2.4, the limitations and drawbacks of $L_2$ regularization and MLS-AART can be summarized as follows. As presented in Section 2.4, the $L_2$ regularization entails smoothing effects and results in continuous and spatially over-spread reconstructions while damping noise-induced artifacts. The $L_2$ regularization filters out the high-frequency and edge-type features of the fluorescence distribution and impairs the resolution offered by FT reconstructions while removing artifacts caused by noise and modeling errors. Results reported for FT reconstructions using $L_2$ regularization in Section 2.4 possess less spreading and are better resolved in shallow depths. However, as the depth of the fluorescent inclusions increases, the need for stronger regularization rises, resulting in high spatial spreading and poor resolution. Structural and anatomical priors have been used to improve the performance of $L_2$ regularization and adapt the regularization parameters to the geometry and *a priori* information of the FT problem. This has been shown to greatly enhance the accuracy of 3D reconstructions in a few studies [81-84]. However, the performance of adaptive methods relies on the availability of priors and in problems with limited or error-contaminated priors, adaptive methods cannot perform optimally.

The MLS-AART performed accurately for cases with low levels of noise or error contaminations. In general, ARTs are used extensively in imaging scenarios with accurate models and low-noise data. Nevertheless, the performance of MLS-AART deteriorates as modeling errors and data noise level increase. MLS-AART does not possess strong regularizing power. This makes MLS-AART unsuitable for performing reconstructions on noisy data and error contaminated models. As a result, the

reconstructions from MLS-AART had a higher level of artifact contamination compared to the $L_2$ regularization.

# CHAPTER 3

# TOTAL VARIATION REGULARIZATION

## 3.1 Motivation

As discussed in Chapter 2, reconstructing the 3D fluorescent distribution in biological tissue from the fluorescent signal measured on the tissue boundary is a highly ill-conditioned problem as the depth information must be extracted from the data collected on the tissue surface. FT inverse solvers use regularization techniques to overcome the ill-posed nature of this problem and minimize the artifacts and errors contaminating the 3D reconstructions. Conventionally, as discussed in Chapter 3, the $L_2$ regularization method in which the $L_2$ norm of the solution or a linear transformation of the solution is penalized has been used for 3D reconstructions in FT. As discussed in Sections 2.4 and 2.5, the spatial resolution of the reconstructions of the $L_2$ regularization is poor. The low resolution is due to the smoothing nature of the $L_2$ norm, and the bias of the $L_2$ regularization towards spatially smooth inclusions. Also, as presented in Chapter 2, non-regularizing algorithms such as the MLS-ART do not perform optimally in FT scenarios with high levels of error or noise contaminating the model and the data.

In this chapter, the use of the total variation (TV) regularization for performing FT reconstructions is described. In the TV regularization, the TV semi-norm of the solution is penalized to stabilize the reconstructions against artifacts and errors in the data and modeling. TV image reconstruction is widely used in image processing and has been shown to enhance the contrast and the resolution of image reconstruction over the existing $L_2$ regularization technique in various medical and molecular imaging modalities such as bio-luminescence tomography and emission tomography [85, 86]. In this

regularization technique, the penalty term added to the least-squares data fidelity is the TV semi-norm of the solution as formulated in Equation 54:

$$\min_x \|y - Mx\|_2^2 + \lambda^2 \|x\|_{TV} , \tag{54}$$

where the discretized 3D fluorescent distribution is stacked in a one-dimensional (1D) vector denoted by x. Assuming that the 3D continuous scalar function representing the fluorescent distribution is denoted by u, the TV semi-norm of u can be defined as

$$\|x\|_{TV} = \int |\nabla u| d\Omega . \tag{55}$$

The integral in Equation 55 is taken across the space over which x is defined. In Equation 55, the differential element for volume is denoted by $d\Omega$, and the gradient of u is denoted by $\nabla u$. The TV semi-norm can be interpreted as the $L_1$ norm of the gradient of the 3D fluorescent distribution. Hence, in the TV regularization, the size of the variations in the solution is penalized, whereas in the $L_2$ regularization, the size of the solution itself is penalized.

## 3.2 Resolution of 3D Reconstructions: Total Variation versus $L_2$

The major limitation of the $L_2$ regularization stems from its over-smoothing property. Similar to low-pass filtering in the de-noising of 1D signals, the high-frequency components and edge-type features of the reconstructed inclusions are filtered out in the $L_2$ regularization. This filtering is done to remove the noise and error-induced artifacts from the reconstructions. Therefore, the artifacts are removed and the solution is stabilized at the cost of over-smoothing the sharp transitions and well resolved inclusions. As a result, the spatial resolution of the reconstruction algorithm is impaired at the expense of securing stability in the solution.

To provide a better insight into the spatial resolution of image reconstruction algorithms, their point spread functions (PSF) can be studied. PSF is a concept used in resolution studies for comparing the spatial resolving power of image reconstruction methods in linear problems [87]. Unlike the $L_2$ regularization, the edges and sharp transitions are not smoothed out in the TV regularization. Only highly oscillatory components are filtered out. Therefore, the TV regularization is expected to yield a better spatial resolution compared to the $L_2$ regularization. To compare the spatial resolution of the TV regularization and the $L_2$ regularization, their corresponding PSFs were studied in a 2D numerical study.

In a given turbid medium and data acquisition geometry, the PSF is defined as the reconstruction of an image that contains only a single non-zero pixel or voxel without any noise or errors present in the data or modeling. In FT, an image reconstructed from noiseless data generated from a unit-impulse fluorescent distribution represents the PSF of that voxel. Various qualities of image reconstruction techniques can be studied by examining their PSFs. The distortions and artifacts generated in an image when projected to the data domain and back to the image domain through a reconstruction algorithm are revealed by examining the PSFs of that algorithm. In the $L_2$ regularization, which is mathematically formulated as

$$\min_{\mathrm{x}} \|\mathrm{y} - \mathrm{Mx}\|_2^2 + \lambda^2 \|\mathrm{x}\|_2^2 , \tag{56}$$

the reconstructed image $\mathrm{x_{rec}}$ is directly related to the true image $\mathrm{x_{orig}}$ through a linear system [87]. This system is derived by assuming theoretically perfect noiseless conditions, which are suitable for exploring the PSFs, as shown in Equation 57:

$$(\mathrm{M^*M} + \lambda^2 \mathrm{I})\mathrm{x_{rec}} = \mathrm{M^*Mx_{orig}} . \tag{57}$$

The PSFs of the $L_2$ regularization can be calculated by substituting $x_{orig}$ in Equation 57 by a vector with only one non-zero entry and solving for $x_{rec}$. As a result, the columns of the resolution matrix formulated as $R = (M^*M + \lambda^2 I)^{-1} M^*M$ are the PSFs of the corresponding voxels (entries) in x. As the value of the parameter $\lambda$ in Equation 56 increases, *i.e.*, the strength of regularization increases, the term $\lambda^2 I$ becomes larger. This increase in the regularization component $\lambda^2 I$ results in more non-zero off-diagonal entries in the resolution matrix. Hence, the spatial resolution of the $L_2$ regularization decreases with increase in the regularization strength.

In the TV regularization, the reconstructed fluorescent distribution $x_{rec}$ is related to the actual fluorescent distribution $x_{orig}$ by

$$\left(M^*M + \lambda^2 \nabla . \frac{\nabla}{|\nabla u|}\right) x_{rec} = M^*M x_{orig}\,, \tag{58}$$

which is derived by setting the derivative of the objective in Equation 54 to zero. Also in arriving at Equation 58, it is assumed that $|\nabla u_{rec}| = |\nabla u_{orig}|$ considering the edge-preserving behavior of the TV regularization. To obtain the PSFs of the TV regularization, $x_{orig}$ is substituted by a vector with only one non-zero entry in Equation 58, and $x_{rec}$ is computed.

In Figure 21, a comparison of the PSFs of the TV regularization and the $L_2$ is depicted for a 2D numerical study. For an off-edge voxel, both regularization techniques result in spatial spreading around the corresponding voxel. However, for an on-edge voxel, the TV regularization has no spreading across the edge and does not diffuse nor smooth the edge. However, the $L_2$ regularization results in spatial spreading in all directions.

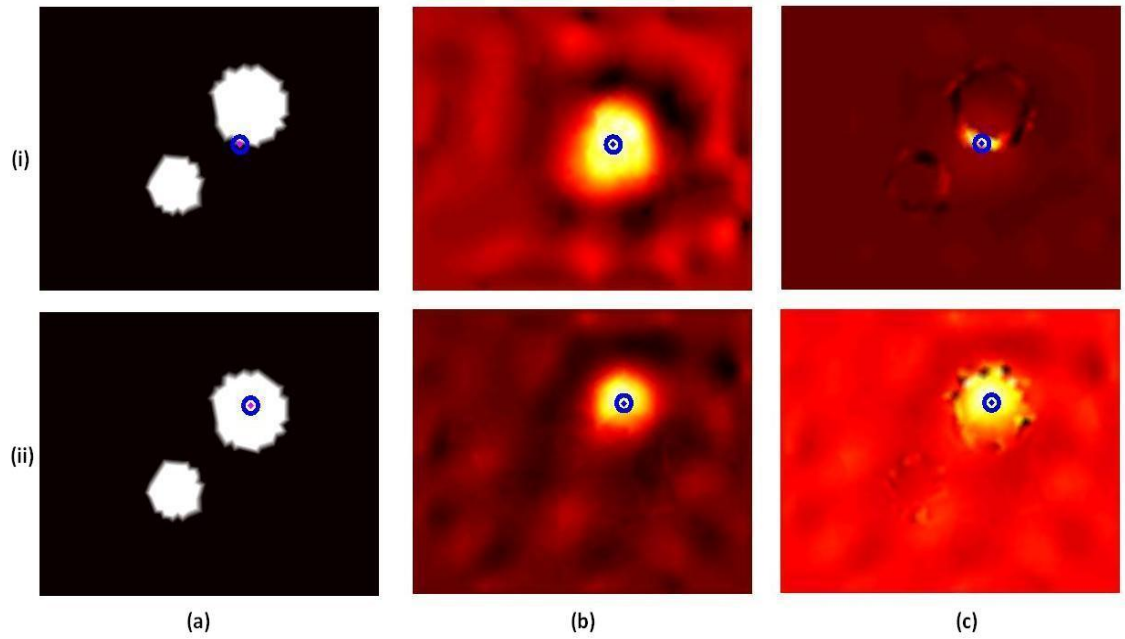


**Figure 21: The PSFs of the $L_2$ regularization and the TV regularization are compared for (i) on-edge and (ii) off-edge voxels. (a) Original fluorescent distribution and voxels whose PSFs are being studied are plotted. (b) The PSFs of the $L_2$ regularization of a moderate strength are plotted. (c) The PSFs of the TV regularization of a moderate level are plotted.**

As observed in Figure 21, the PSF of the TV regularization has almost no smoothing or regularizing effect for on-edge voxels. Nevertheless, there is a moderate level of spreading for off-edge voxels. This edge-preserving adaptive nature of the TV regularization can be explained by the fact that, as expressed in Equation 58, the regularizing term or operator in the TV regularization, formulated as $\lambda^2\nabla.\frac{\nabla}{|\nabla u|}$, depends on the gradient of the reconstructed image. The denominator of the regularization term has an important role in the performance of the TV regularization. The denominator $|\nabla u|$ has large values on the edges of u and small values on the smooth regions of u. Hence, the operator $\lambda^2\nabla.\frac{\nabla}{|\nabla u|}$ is small for voxels sitting on the edges and large for those away from the edges and sharp transitions.

Therefore, the TV regularization can be viewed as an adaptive form of regularization. For the voxels sitting in smooth regions away from the edges, strong regularization filters out oscillations and high-frequency components. But for the voxels sitting on the edges, there is weak or no regularization. So the high-frequency components are not filtered out for on-edge voxels. The PSFs do not possess smoothing around the voxels sitting on the edges. The edges are preserved in the reconstruction process. This edge-preserving property of the TV regularization results in higher spatial resolution compared to the $L_2$ regularization.

## 3.3 Implementation of the TV regularization

To implement the TV regularization for FT, the minimization in Equation 54 needs to be solved numerically. The minimization in Equation 54 is a nonlinear optimization problem. So it cannot be solved directly using linear solvers. Two different approaches are used to solve for x in the nonlinear optimization problem in Equation 54. A variational method inspired by the Rudin-Osher-Fatemi (ROF) TV de-noising technique [88], and an iterative method inspired by the linearized split Bregman iteration method [89] are used to solve the optimization problem in Equation 54.

In the first approach, an ROF-based TV regularization algorithm is used to solve the minimization problem. Let T represent the combined continuous-to-discrete and reshape operators mapping the scalar function of 3D fluorescent distribution denoted by u to the discretized 1D vector of fluorescent distribution denoted by x. Then, Equation 54 can be written in terms u of as

$$\min_{\mathrm{u}} \|\mathrm{y} - \mathrm{MT}(\mathrm{u})\|_2^2 + \lambda^2 \int |\nabla \mathrm{u}| \mathrm{d}\Omega \,, \tag{59}$$

where $\lambda$ is a scalar that controls the strength of the regularization. Equation 59 is a nonlinear minimization problem in the variable u. The gradient descent method is used to solve Equation 59 iteratively [88]. The gradient of the objective is set equal to the difference between successive iterations divided by the step size denoted by $\Delta t$ as shown in Equation 60:

$$\frac{u^{(k+1)}-u^{(k)}}{\Delta t} = 2T^{*}M^{*}\big(y - MT(u)\big) + \lambda^{2}\,\nabla.\left(\frac{\nabla u}{|\nabla u|}\right). \tag{60}$$

The finite difference method is applied to Equation 60 to discretize and numerically solve for u. The volume over which u is defined is discretized by a uniform rectangular mesh and u and its spatial derivatives are approximated by finite difference equivalents [88]. To ensure fast convergence, the initial guess used in this iterative method is the solution of $L_2$ regularization. The choice of $\lambda$ and $\Delta t$ is fundamental to the convergence and optimal performance of the algorithm. The symbol $\Delta t$ represents the time step in the numerical solver. This parameter should be optimized to obtain the highest possible rate of convergence to the steady-state solution while meeting certain constraints required for maintaining numerical stability, e.g., $\Delta t$ must be small enough to satisfy the Courant–Friedrichs–Lewy (CFL) condition [90]. The trade-off between the data fidelity and regularization strength is scaled using the parameter $\lambda$. To ensure best performance, the values for these parameters are chosen empirically.

In the second approach, the recently explored method of split Bregman iteration is used to solve the minimization problem in Equation 58. Detailed derivation of this heuristic algorithm for TV minimization can be found in Ref. [91]. Unlike $L_2$ regularization, the optimization problem of TV regularization often possesses several local minima. Only some of these minima correspond to the desirable solution. Under

certain conditions, any iterative solver may converge to the undesirable local minima. In the ROF approach, the undesirable minima were avoided by using the solution of $L_2$ regularization as an initial guess. For the Bregman iteration, an initial guess cannot be used. Therefore, the algorithm needs to be modified and biased away from undesirable local minima and towards the desired solution. This modification is done by adding an extra term to the objective of the minimization. This extra term has bias towards an initial guess that is the solution of $L_2$ regularization. The modified biased minimization problem can be written as

$$\min_u \int |\nabla u| d\Omega \ + \frac{\mu}{2} \|MT(u) - y\|_2^2 + \frac{\alpha}{2} \|u - u_{ls}\|_2^2 , \tag{61}$$

where, for the purpose of simplicity in the final form of the algorithm, the regularization parameter $\lambda$ is removed, and a positive weight denoted by $\frac{\mu}{2}$ has been added to the data fidelity. The relaxation parameter, which is denoted by $\alpha$, controls the strength of the bias term that guides the algorithm to the vicinity of the least-squares solution to avoid convergence to unwanted local minima of the TV regularization. To solve the optimization problem in Equation 61, the concept of sub-gradient space is used in the split Bregman method [89, 91] to determine the direction of descent. This descent is repeated iteratively until the algorithm converges to a solution.

Mathematically, the minimization in Equation 61 is relaxed to an iterative updating scheme by introducing auxiliary variables $b^k$ and $d^k$ that lie in the sub-gradient as formulated in Equation 62:

$$u^{k+1} = \min_u \frac{\mu}{2} \|MT(u) - y\|_2^2 + \frac{\alpha}{2} \|u - u_{ls}\|_2^2 + \frac{\beta}{2} \left\| d^k - \nabla u - b^k \right\|_2^2 . \tag{62}$$

where β is the relaxation weight of the sub-gradient term and determines the direction of the descent associated with each iteration. A large β would stipulate a descent in a direction very close to the gradient at the expense of jeopardizing the data fidelity. The parameters α, β, and μ are selected empirically by performing an exhaustive search. By setting the derivative of Equation 62 to zero, Equation 63 is obtained:

$$(\mu T^{*}M^{*}MT(u) + \alpha I - \beta\Delta)u^{k+1} = \mu T^{*}M^{*}y + \alpha u_{ls} + \beta\nabla^{*}\left(d^{k} - b^{k}\right), \qquad (63)$$

where the symbol Δ denotes the Laplacian operator. The iteration described in Equation 63 and the updates for the auxiliary variables as formulated in Ref. [91] summarize the core step of the split Bregman method for TV regularization of the FT inverse problem. The system of equations in Equation 63 is symmetric positive-definite. Therefore, Equation 63 can be solved using the preconditioned conjugate-gradient method in each iteration [92].

## 3.4 Numerical and Experimental Studies

To compare the performance of TV regularization with conventional $L_2$ regularization and MLS-ART, these methods were applied to 2D simulated FT data. The forward solver from the simulation platform described in Section 1.2.4 was used to simulate a 2D FT configuration. The simulated data were contaminated with different levels of noise. The 2D simulated FT configuration is depicted in Figure 22. The two white blobs represent fluorescent inclusions with unit quantum efficiency and fluorescence absorption $\mu_{fl}$ of $0.1\ \mathrm{mm}^{-1}$ in a rectangular turbid medium with dimensions of 8 cm by 6 cm, absorption coefficient $\mu_a$ of $0.01\ \mathrm{mm}^{-1}$, and scattering coefficient $\mu_s$ of $1\ \mathrm{mm}^{-1}$ that mimic the optical properties of biological tissue. The blue squares and the red circles in Figure 22 represent sources and detectors. Eight sources and eight

detectors are used in the FT configuration as shown in Figure 22, so the data vector denoted by y has 64 entries. The data vector y is contaminated by three different levels of additive white Gaussian noise that result in SNRs of 50 dB, 40 dB, and 30 dB in the data. After the noise is added, the data vector y is fed to the reconstruction algorithms.

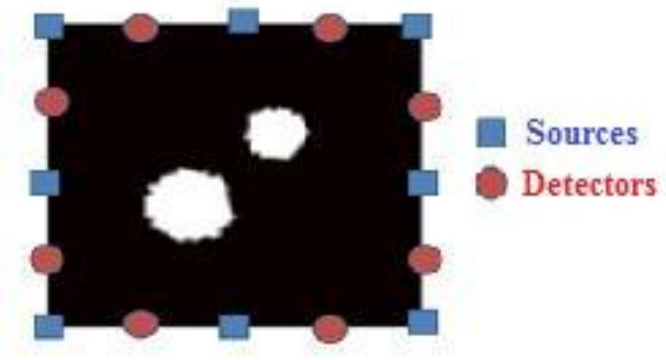


**Figure 22: In a 2D fluorescence tomography configuration, two fluorescent blobs are simulated in a turbid rectangle with eight sources and eight detectors for illumination and data acquisition.**

The 3D reconstructions from the $L_2$ regularization, the MLS-ART, and the two implementations of the proposed TV regularization are depicted in Figure 23 [93, 94]. The numerical studies presented in Figure 23 reveal the effect of noise on the performance of different reconstruction algorithms. MLS-ART is an unbiased and non-regularized reconstruction technique. This algorithm does not converge to the solution for low-SNR FT data as shown in column (ii) of Figure 23. For $L_2$ regularization, the two blobs are successfully reconstructed as depicted in column (i) of Figure 23. But the spreading and over-smoothing effects of $L_2$ regularization are present, especially for the low-SNR cases. As shown in column (iii) of Figure 23, in the ROF-based TV regularization, the blobs are reconstructed with high resolution in high-SNR cases.

Nevertheless, in low-SNR scenarios, artifacts in the form of edge distortion and shifting are present in the reconstructions of the ROF-based TV regularization. The

performance of the split Bregman-based TV regularization is also well for high-SNR cases. The high resolving power of the Bregman method can be observed in column (iv) of Figure 23. However, for low-SNR data, artifacts appear in the reconstructions, and the shapes of the reconstructed inclusions become distorted. So as presented in Figure 23, the $L_2$ regularization reconstructions are robust but have poor spatial resolution, the MLS-ART reconstructions are poor in accuracy and robustness, and the TV regularization reconstructions are robust and have high spatial resolution but are contaminated with edge distortions.

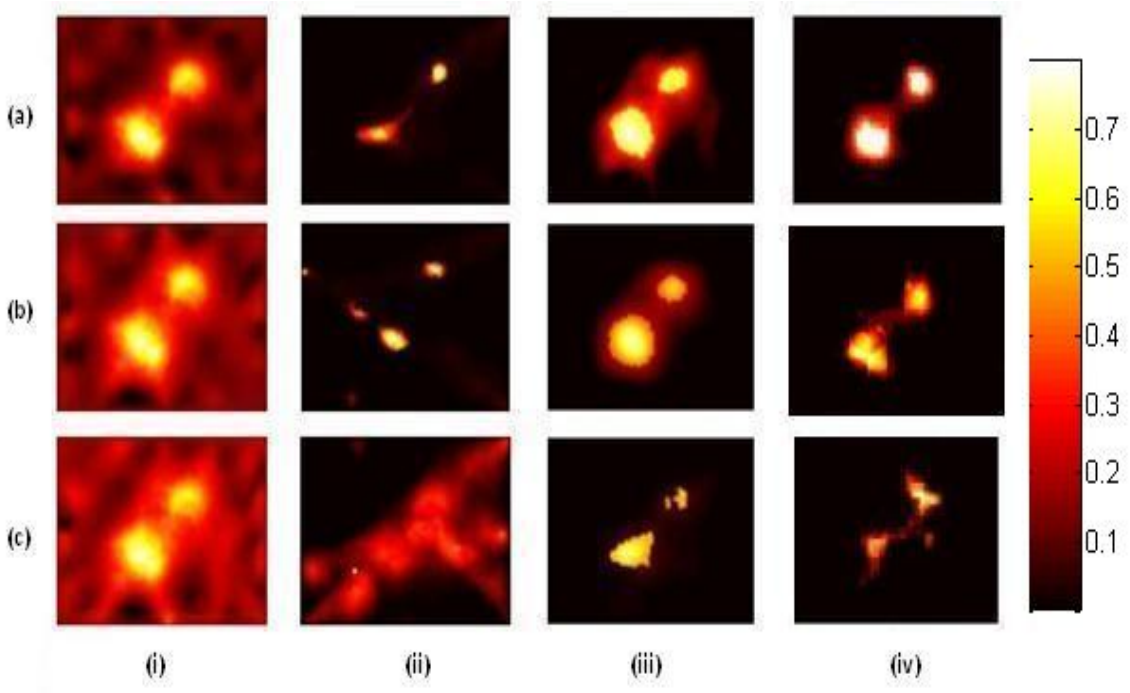


**Figure 23: Fluorescent inclusions are reconstructed from 2D simulated data with (a) 50dB SNR, (b) 40dB SNR, and (c) 30dB SNR, by (i) $L_2$ regularization, (ii) MLS-ART, (iii) time marching ROF TV regularization, and (iv) iterative Bregman TV regularization.**

The least-squares relative estimation error is calculated for each reconstruction and plotted in Figure 24. This error is defined in Equation 64:

$$\varepsilon = \frac{\|x - \hat{x}\|_2}{\|x\|_2}, \tag{64}$$

where $\hat{x}$ represents the reconstructed solution. This error does not reflect the edge-preserving advantage of reconstruction algorithms as effectively as visual inspection of the reconstructed inclusions.

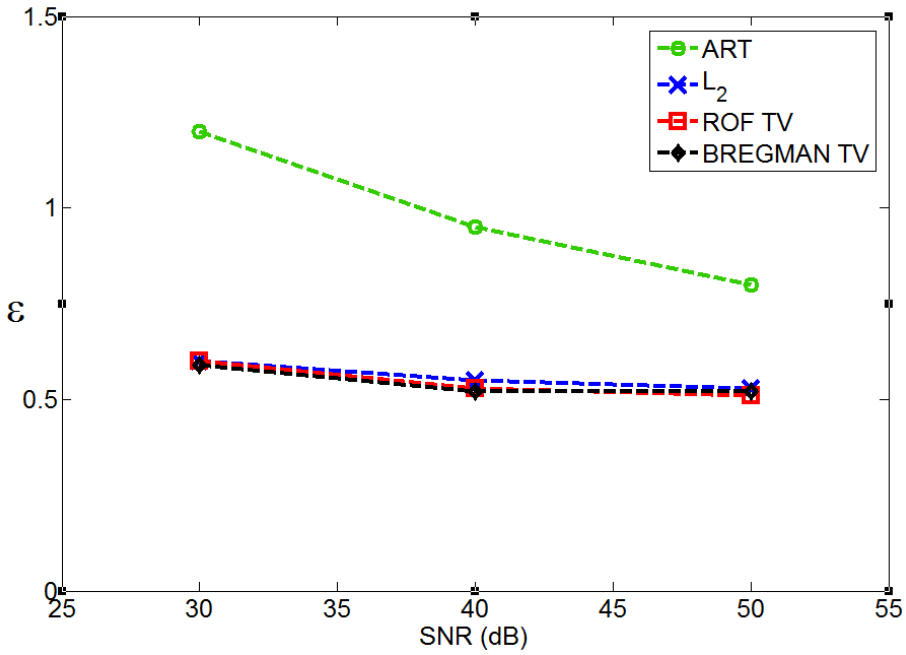


**Figure 24: Relative estimation errors for reconstructed fluorescent distributions corresponding to $L_2$ regularization, algebraic reconstruction technique, and the proposed ROF and iterative Bregman TV regularization for data SNR= 30, 40, 50 dB.**

Also, the Michelson contrast [95] was computed and plotted for each reconstructed image, as formulated Equation 65, to provide a quantitative analysis on the resolution improvements offered by the TV regularization:

$$C = \frac{I_{max} - I_{min}}{I_{max} + I_{min}}, \tag{65}$$

where $I_{max}$ represents the mean of the peak fluorophore concentrations in the two reconstructed blobs, and $I_{min}$ is the minimum fluorophore concentration on the line segment connecting the location of the peaks. In Figure 25, plots of the contrast values for each reconstructed image are depicted. As shown in Figure 24, the accuracy of the TV

regularization reconstructions is better than ART and no less than the conventional $L_2$ regularization. Figure 25 indicates that the resolution offered by the TV regularization is higher compared to $L_2$ regularization due to its edge-preserving property.

MLS-ART also provides a relatively high resolution for high-SNR data because of its weakly regularizing nature, but its performance degrades as the SNR is decreased. For low-SNR data, the TV regularization has higher resolution and accuracy compared to ART. Overall, it can be observed in Figures 24 and 25 that TV regularization is advantageous to the conventional ART and $L_2$ regularization algorithms and performs better in terms of accuracy and resolution compared to ART and $L_2$ regularization, respectively.

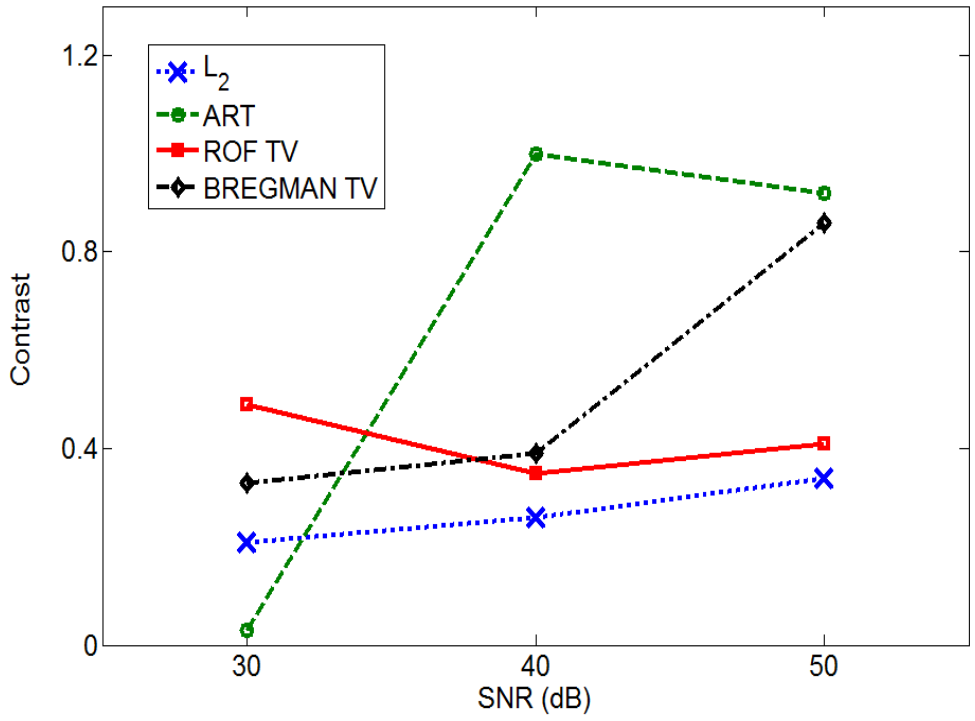


**Figure 25: The Michelson contrast, defined in Equation 15, is computed and plotted for the reconstructed fluorescent distributions corresponding to the $L_2$ regularization, the MLS-ART, and the proposed ROF and iterative Bregman TV regularization for data SNR= 30, 40, 50 dB.**

To compare the performance of the TV regularization with the $L_2$ regularization in experimental settings, a phantom-based FT system was developed and calibrated as described in Sections 1.2.5 and 1.2.6. Two capillary tubes partially filled with Oxazine-750 were suspended vertically in an intralipid-based slab liquid tissue phantom as depicted in Figure 9. One side of the phantom was illuminated at 36 source locations using an optical fiber that is coupled to a He-Ne laser (emission of 633 nm to excite the Oxazine-750 dye). The opposite side of the slab phantom was imaged by a cooled CCD camera to capture the trans-illumination and the fluorescent emission. A general schematic and three pictures of this FT phantom-based system are shown in Figure 4. As depicted in Figure 26, a total of 36 source locations and 81 detector locations were used for the illumination of the phantom and FT data acquisition, respectively.

The tubes were immersed in the tissue phantom vertically at three different depths of 3 mm, 6 mm, and 9 mm from the front surface of the phantom facing the CCD camera. The camera is cooled down to -10 °C to minimize dark-current noise. Dark-frame images (images with laser being off) are taken along with each dataset and subtracted from the data images to remove contamination from stray light and other unwanted signals. A region of interest in the central part of the phantom with an area of 8 cm by 8 cm was selected for reconstruction. A tetrahedral mesh with 15394 nodes and 87671 voxels was used to discretize the selected volume. The acquired FT data are fed to the $L_2$ regularization and the TV regularization for reconstructing the two fluorescent inclusions within the tetrahedral mesh discretizing the central region of the phantom volume.

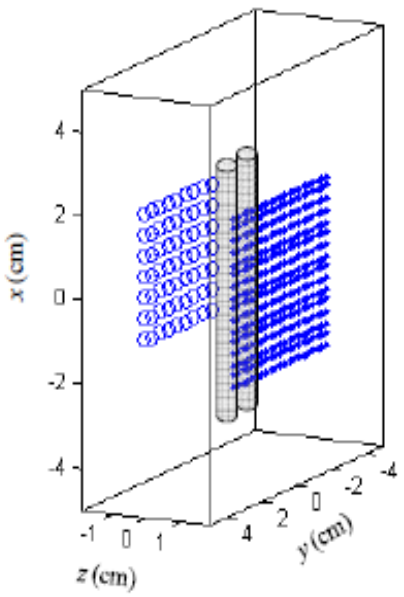


**Figure 26: The configuration used for the experimental phantom-based FT studies consists of two fluorophore-filled capillary tubes inserted in an intralipid liquid phantom that is illuminated at 36 source positions (circles) and imaged by a CCD camera that yields 81 data points (dots).**

In Figure 27, the 3D reconstructions from the experimental data using the $L_2$ regularization and the two implementations for the proposed TV regularization are shown [96]. As the depth of the fluorescent inclusions increases, the fluorescent photons collected on the surface become diffuser and the error-sensitivity of the corresponding FT reconstruction increases. Therefore, stronger regularization is required as the depth of fluorescent inclusions increases. In row (a) of Figure 27, the performance of $L_2$ regularization in reconstructing the two fluorescent tubes at three different depths is shown. For shallow inclusions, the reconstructions do not possess much spreading. The over-smoothing and spatial spreading become very strong at higher depths as the need for strong regularization increases. The ROF-based and Bregman-based TV regularization, as depicted in rows (b) and (c) of Figure 27, perform better in reconstructing the two fluorescent inclusions compared to $L_2$ regularization.

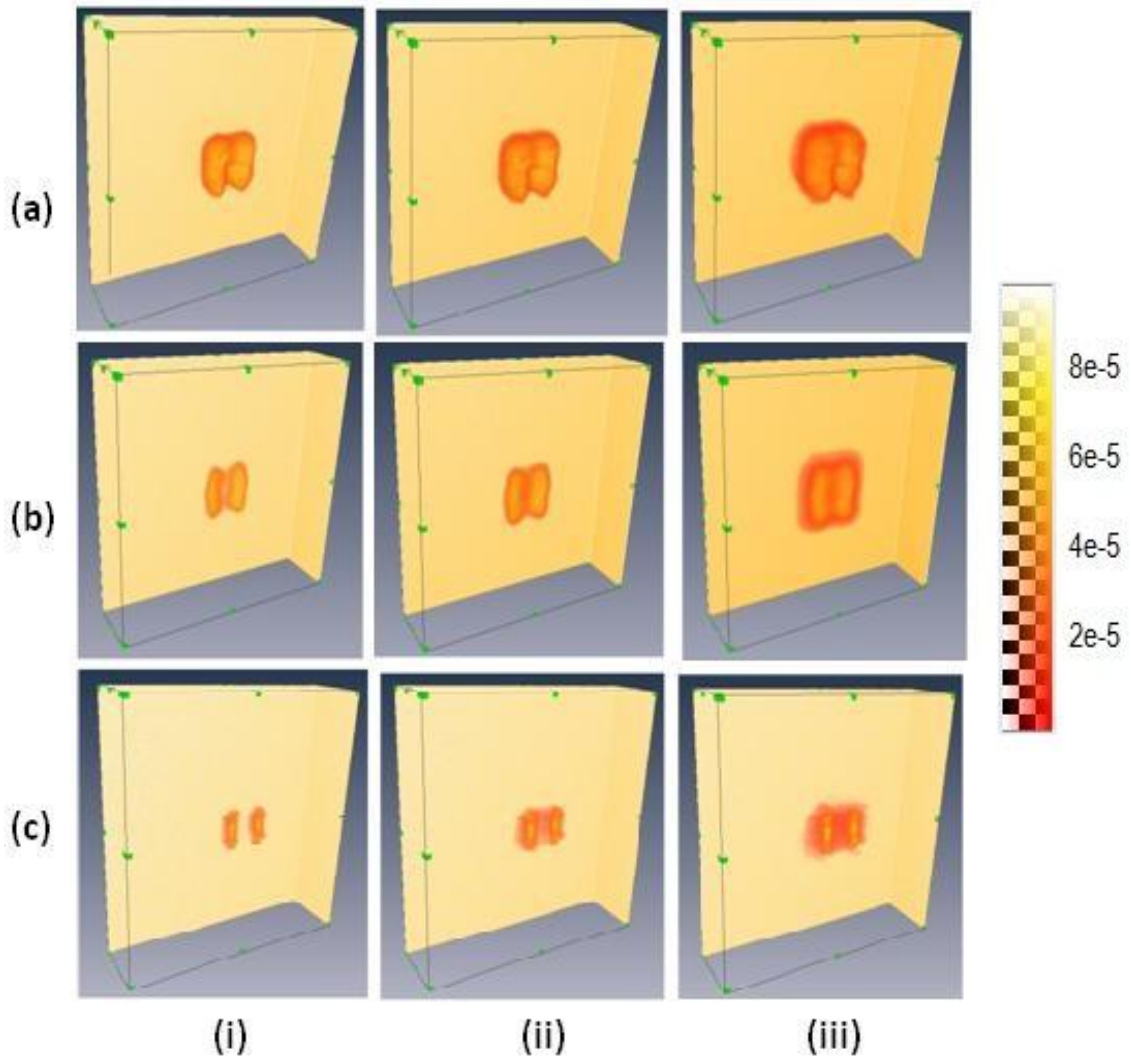


**Figure 27: Fluorescent distributions are reconstructed from experimental data where fluorophore-filled tubes are located (i) 3 mm, (ii) 6 mm, and (iii) 9 mm deep using (a) $L_2$ regularization, (b) time marching ROF-based TV regularization, and (c) iterative Bregman-based TV regularization.**

The reconstructed tubes from the ROF-based TV regularization are well resolved and well localized. Reconstructions from the Bregman-based TV regularization also have high spatial resolution and accuracy. When compared to $L_2$ regularization, results from the ROF-based and Bregman-based TV regularization have less spreading, and the reconstructed tubes are distinctly separated. The results in Figure 27 reveal the

advantages of the TV regularization over the $L_2$ regularization in resolving fluorescent inclusions. While results from both methods possess artifacts, the TV regularization has better performance in recovering and separating lesions and inclusions over $L_2$ regularization.

## 3.5 Advantages and Limitations

The numerical and experimental results presented in this chapter indicate that the TV regularization has the potential to provide higher resolution and greater robustness compared to conventional $L_2$ regularization and MLS-ART. As depicted in Figures 23 and 26, the 2D and 3D reconstructions for both implementations of the proposed TV regularization algorithm are better localized around their corresponding coordinates and possess less spread compared to $L_2$ regularization. The non-spreading and edge-preserving nature of the TV regularization has been the subject of several studies [97, 98]. The advantages of the TV regularization over $L_2$ regularization are analogous to the advantages of wavelet-based de-noising [99] over low-pass filtering in image processing. Low-pass filtering can filter out the oscillatory image noise. However, low-pass filtering also diffuses the edges and sharp transitions and makes the image blurry and poorly resolved. De-noising through wavelet thresholding only filters out highly oscillatory components in the image while preserving the edges and sharp transitions.

The optimization problem in the TV regularization is not as easily tractable as the one in the $L_2$ regularization. The convergence time for the TV regularization is higher than that of the $L_2$ regularization in almost all cases presented in this chapter. Among the two implementation of the TV regularization presented in this chapter, the split Bregman iteration provides a faster convergence compared to the ROF. This speed difference is

due to the time-marching property of ROF. It takes 100 or more iterations for ROF to converge even when started with a good initial guess. The split Bregman converges within 20 iterations. However, the time required for each step of the ROF is significantly less than the time needed for each step of the split Bregman where the preconditioned conjugate-gradient method needs to be implemented. Pre-conditioned conjugate-gradient method may converge fast or slow depending on the condition number of the symmetric positive-definite linear operator in Equation 63. In other words, in strongly regularized cases, the split Bregman iteration is considerably faster than the ROF while for weakly regularized cases the two approaches have similar convergence times.

The difference between the ROF approach and the split Bregman iteration lies in the degrees of freedom associated with the gradient of the reconstructed image in each method. The split Bregman iteration is not biased towards certain edge directions because this algorithm operates on each gradient component separately. Conversely, the ROF method prefers circular and isotropic edges as the ROF method acts on the magnitude of the gradient vector and not its components. The ROF reconstructions tend to be circular or cylindrical in shape, or isotropic in a more general sense. However, the split Bregman reconstructions have edges and borders of various shapes. This unbiased property makes the split Bregman iteration better in reconstructing various fluorescent inclusions compared to the ROF. Nevertheless, this property also makes split Bregman more sensitive to error-induced edge distortions compared to the ROF. This inherent difference between the ROF and the split Bregman reveals the reason behind the difference between the reconstructions from these two implementations in the numerical and experimental studies.

Based on the results reported in Section 4.4, it is concluded that for performing 3D reconstructions in FT, the $L_2$ regularization is remarkably noise-robust and faster than the TV regularization. But the $L_2$ regularization has poorer resolution compared to the TV regularization. For high-SNR data, the ROF-based TV regularization provides stable results with higher resolution compared to $L_2$ regularization. But the accuracy of the ROF method diminishes with increase in the error and noise level. The split Bregman-based TV regularization performs faster than ROF and provides better resolution than $L_2$ regularization. However, for low-SNR data the performance of the split Bregman method is not as robust as either $L_2$ regularization or the ROF-based TV regularization. Therefore, for high-SNR cases, split Bregman-based TV regularization can provide fast reconstructions with improved resolution, whereas the ROF-based TV regularization can be used for improving the reconstruction resolution in low-SNR cases.

In conclusion, two implementations of the TV regularization were presented and investigated for 3D reconstructions in FT. The main advantage of the TV regularization over the conventional $L_2$ regularization is that in the TV regularization the spatial resolution of the reconstruction is not jeopardized to secure reconstruction stability. In the $L_2$ regularization, the resolution is compromised for stability. Weakly regularized reconstructions have artifacts such as oscillatory components and impulses contaminating the reconstructed inclusions. Strongly regularized reconstructions have smooth and spatially over-spread inclusions as depicted in column (i) of Figure 23 and row (a) in Figure 27. In the TV regularization, it is observed that the edge-preserving nature of the algorithm does not allow spatial spreading in the reconstruction. But the edges of the inclusions may shift as the noise and error levels increase. As can be observed in Figures

23 and 26, strongly TV-regularized reconstructions from low-SNR data do not possess spatial spreading and retain edges and sharp transitions. However, the presence of noise can affect the location of the edges and result in distortions in the shape of the inclusions. These distortions are evident in columns (iii) and (iv) of Figure 23. Consequently, the types of artifacts present in the reconstructions of the TV regularization are inherently different than those in the $L_2$ regularization. In the $L_2$ regularization, removal of artifacts results in poor resolution. In the TV regularization, artifact removal causes distortions in the borders of the reconstructed inclusions. Additionally, the form of noise-induced distortions in the reconstructions of the TV regularization differs between the two implementations. The ROF-based approach is biased towards circularly shaped reconstructions and is less prone to edge distortions as depicted in column (iii) of Figures 23 and row (b) of Figure 27. The split Bregman iteration has more severe edge distortions compared to the ROF. The noise-induced distortions impair the shape and borders of the reconstructed inclusions, especially for low-SNR FT.

To summarize, the resolution offered by the two approaches for the TV regularization is higher than the $L_2$ regularization for high- and low-SNR data because the TV regularization does not compromise resolution to secure stability. The convergence times required for both implementations of the TV regularization are higher than the convergence time for $L_2$ regularization. In low-SNR cases, the spatial resolution is jeopardized in the $L_2$ regularization, and edge distortions contaminate the reconstructions of the TV regularization.

# CHAPTER 4

# HADAMARD TRANSFORM APPROACH TO ROBUST FLUORESCENCE TOMGORAPHY

As discussed in Chapters 2 and 3, the FT data SNR plays an important role in the quality of FT reconstructions. In this chapter, a system-level approach is presented for enhancing the FT data SNR without overcomplicating the hardware used in FT systems. A comprehensive numerical study is presented to validate the advantages of the proposed FT system architecture.

## 4.1 Need for Higher Signal-to-Noise Ratio (SNR)

The performance of various FT reconstruction algorithms and their advantages and limitations were discussed in Chapters 2 and 3. While each reconstruction method offers advantages over the others, performs optimally in certain aspects, and is well-suited for some FT scenarios, none can be selected as the most effective method globally. Furthermore, as indicated by the results presented in Chapters 2 and 3, all the reconstruction methods discussed in Chapters 2 and 3 perform reasonably well in reconstructing shallow inclusions from high-SNR data. However, once the data is noisy (SNR < 30 dB or less) and the inverse problem is extremely ill-conditioned, the performance of the reconstruction algorithms deteriorates in various ways. Depending on the dynamics and nature of the reconstruction algorithm, artifacts and errors arise when reconstructing inclusions from noisy data. Table 2 summarizes the advantages and limitations of the algorithms discussed in Chapters 2 and 3 in performing reconstructions from noisy FT data.

**Table 2: Performance of inverse solvers in reconstructing from low-SNR (30 dB or less) data in highly ill-posed FT scenarios.**

| Method | Resolution | Robustness | Speed |
|---|---|---|---|
| $L_2$ Regularization | Low | High | Low |
| MLS-ART / MLS-AART | Moderate | Very Low | Very High |
| ROF-based TV Regularization | High | Moderate | Very Low |
| Bregman-based TV Regularization | High | Low | Low |

As presented in Table 2, each of the four reconstruction methods suffer from certain limitations and drawbacks in reconstructing inclusions form noisy (or low-SNR) FT data. $L_2$ regularization cannot perform robustly unless it strongly regularizes the inverse problem which, as discussed extensively in Chapter 3, will severely harm the resolution of its reconstructions. MLS-ART (or MLS-AART) is not noise-robust and its reconstructions can become severely contaminated by noise-induced artifacts when reconstructing from low-SNR data as discussed in Chapters 2 and 3. TV regularization is considerably more robust than MLS-ART, however, as discussed in Chapter 3, it does not regularize on-edge voxels so noise-induced artifacts contaminate its reconstructions in the form of edge distortions. ROF-based TV regularization has fewer degrees of freedom in reconstructing inclusions and therefore is less prone to edge distortions compared to Bregman-based TV regularization. Therefore, while both suffer from edge distortions in noisy FT scenarios, ROF-based TV regularization performance is more noise-robust yet

less accurate than Bregman-based TV regularization because it is biased towards isotropic shapes as discussed in Chapter 3.

To summarize the information in Table 2, it can be concluded that all the available reconstruction algorithms, though optimal in certain FT scenarios, fail to provide robust high-resolution reconstructions in noisy and error-contaminated FT scenarios. Improvements in the conditioning of the inverse problem and modeling are of great help in enhancing the accuracy of the reconstructions. However, in many FT scenarios, *e.g.*, imaging of highly heterogeneous regions of small animals, modeling errors cannot be controlled and, depending on the bulk and shape of the animal, the associated inverse problem can be extremely ill-conditioned. Hence, improving the SNR in the data acquisition module is of crucial importance in FT and strongly contributes to the quality of reconstructions regardless of the inversion algorithm being used.

The SNR of FT data is affected by four parameters: sensitivity of the data acquisition system (CCD), absorption of the turbid medium, quantum efficiency of the fluorescent dye, and power of the illumination source. Existing FT systems are equipped with extremely costly, ultra-sensitive, cooled charge-coupled device (CCD) cameras to guarantee a high data-acquisition SNR. Disadvantages of ultra-sensitive CCD systems are two-fold; they are only available at high costs, and they require lengthy integration times for extremely low-noise data acquisition (resulting in extremely lengthy FT scan times). Absorption of the tissue sample being imaged and the quantum efficiency of the administered fluorescent dye vary from experiment to experiment and cannot be controlled in FT systems.

The power of the light source used for illumination of the medium and excitation of the fluorophores is bounded by the per area laser radiation injury thresholds for human skin and biological tissue [100]. Therefore, for conventional point-source FT configuration, which was described in Section 1.6, the power entering the medium is bounded by the skin maximum permissible exposure (MPE) [101] (~2 $mW/mm^2$). However, if instead of single-point illumination, multiple points are illuminated simultaneously, more power can enter the medium. But the problem with multi-point illumination is that as the number of simultaneously illuminated points increases, the number of uncorrelated or minimally correlated measurements obtainable by changing the illumination points decreases. As an example, if all the sources are activated simultaneously, a tremendously high level of radiative power will enter the medium and excite the administered fluorophores, but the acquired data will not include the same level of information content offered by a series of single point illumination measurements. Hence, a trade-off exists between the average number of simultaneously illuminated points per measurement and the information content of the data acquired in that series of measurements. This trade-off can be optimized using Hadamard transform which will be discussed in Section 4.2.

Additionally, in many wide-band FT systems, which offer tunable wavelength in the visible and NIR spectra for the excitation light, the illumination source being used is a filtered incandescent white light source. Considering their relatively low cost and easy maintenance, filtered incandescent sources are preferred over costly and complex tunable high-power lasers for wide-band FT systems. The main disadvantage of filtered incandescent sources is that their radiative power is considerably lower than lasers. As a

result, FT imaging of highly absorbing regions of animal or human subjects with these FT systems is not possible due to their low radiative power.

## 4.2 Hadamard Transform

Hadamard transform is a linear transform used for SNR enhancement in multi-source (or multi-input) measurement systems. Instead of performing measurements with one source active at a time, measurements are acquired while a number of sources are on simultaneously [102]. As discussed in Section 4.1, a trade-off exists between the information content of acquired measurements and the average number of sources active during each measurement. The theory of Hadamard transform [102] provides the optimal multiplexing scheme for measurements that suffer from low SNR. This optimal (0, 1)-weighing scheme is encoded in Hadamard S-matrix, which is a square matrix with entries that are either zero or one. The S-matrix is constructed such that each column (or row) has the maximum possible number of ones while the matrix maintains full rank and remains non-singular.

The Hadamard S-matrix provides the optimal encoding scheme for multiplexing multi-source measurement systems. Each column of the S-matrix is used as a multiplexing scheme for its corresponding measurement and encodes the sources that are on and the sources that are off (with ones and zeros, respectively) in that measurement. As an example, a Hadamard S-matrix of size seven-by-seven is shown below

$$S = \begin{bmatrix} 1 & 1 & 1 & 0 & 1 & 0 & 0 \\ 1 & 1 & 0 & 1 & 0 & 0 & 1 \\ 1 & 0 & 1 & 0 & 0 & 1 & 1 \\ 0 & 1 & 0 & 0 & 1 & 1 & 1 \\ 1 & 0 & 0 & 1 & 1 & 1 & 0 \\ 0 & 0 & 1 & 1 & 1 & 0 & 1 \\ 0 & 1 & 1 & 1 & 0 & 1 & 0 \end{bmatrix}. \tag{66}$$

The multiplexing scheme encoded in the first column of the S-matrix in Equation 66 stipulates that sources numbered 1, 2, 3, and 5 to be on while sources numbered 4, 6, and 7 to be off in the first measurement. The matrix has seven columns so a total of seven measurements can be obtained matching the total number of measurements possible by single-source measurements (since there are seven sources). Moreover, in the measurements obtained using the S-matrix multiplexing scheme, an average of four sources are active during each measurement making the data SNR orders greater than that of single-source measurements. In general, in a measurement system with N sources, S-matrix Hadamard multiplexing increases the SNR by a factor of $\sqrt{N}$ approximately [102]. Therefore, Hadamard multiplexing becomes extremely advantageous in measurement systems with a high number of sources.

In Figure 28, a system-level comparison of conventional single-source and Hadamard multiplexed architectures is presented. Each system has seven inputs or sources. The level of output (detector) noise contaminating the data is identical for both systems. The conventional single-source scheme, as depicted in Figure 28 (a), has a considerably lower output SNR compared to the multi-source Hadamard multiplexed scheme, as shown in Figure 28 (b). This output SNR advantage of Hadamard multiplexing is due to the overlap in the activation of the system inputs or sources. There are four simultaneously active sources at each time in the Hadamard multiplexed system, whereas in the conventional system, only one source is active at a time. This leads to the output signal in the Hadamard multiplexed architecture to be orders higher in intensity compared to the single-source architecture. The amplification order in the output of the Hadamard multiplexed architecture depends on the nonlinearity level of the system.

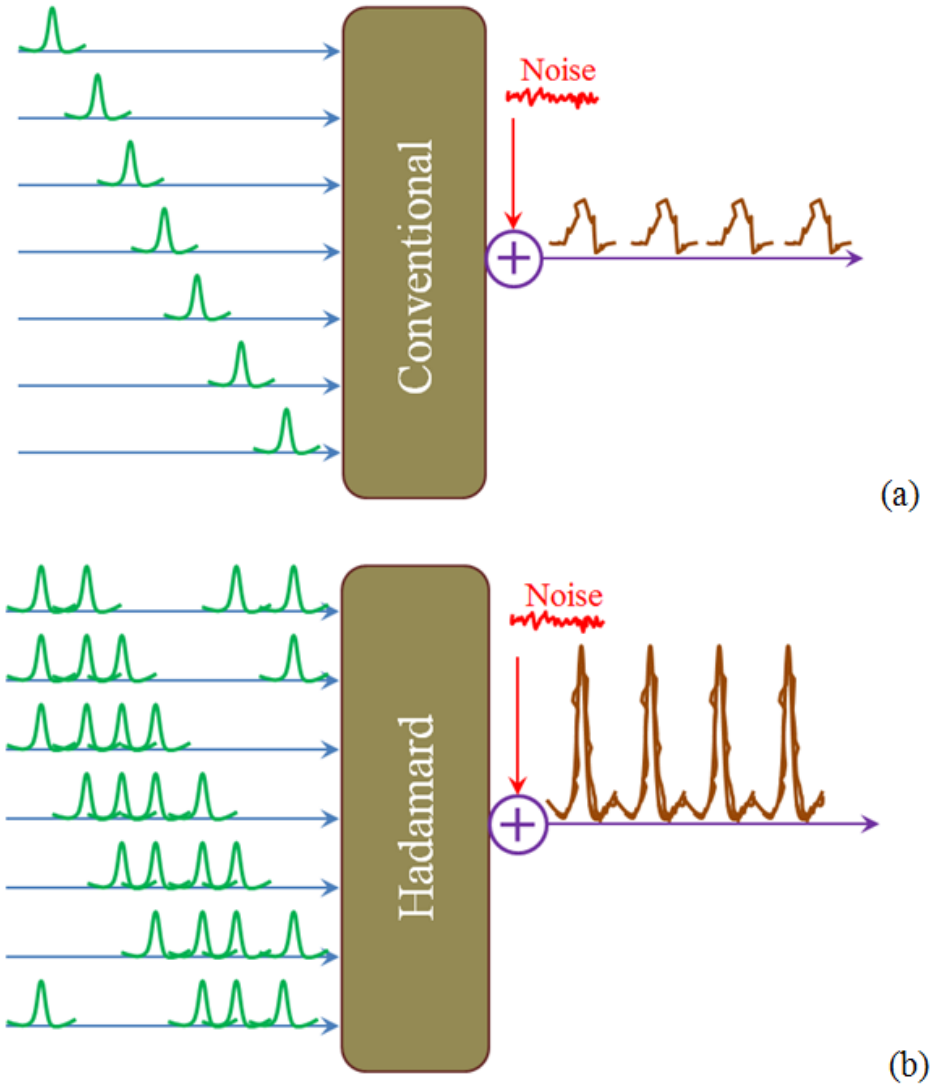


**Figure 28: The conventional single-source and Hadamard multiplexed configurations are compared from a system-level approach. For a fixed level of detector or output noise, the Hadamard multiplexed scheme results in higher SNR in the output signal compared to the conventional scheme.**

## 4.3 Hadamard Multiplexing for Fluorescence Tomography

As described in Section 4.1, SNR enhancement in FT greatly improves the 3D reconstructions irrespective of the inverse solver being used. In FT, multiple sources illuminate the medium at different boundary locations one at a time (as discussed in Section 1.6) and the power entering the medium is limited by the radiation injury threshold of skin. As discussed in Section 4.2, Hadamard multiplexing can be applied to

multi-source systems to enhance the SNR of the acquired data and hence is perfectly suitable for SNR enhancement in FT. Hadamard S-matrix encodings can be used for design of multi-source illumination schemes in FT to improve the SNR of the acquired data without jeopardizing the information content.

In Figure 28, a graphical comparison of conventional FT and Hadamard multiplexed FT is presented. The multiplexing scheme of the S-matrix in Equation 66 is applied to an FT system with seven sources that illuminate a slab turbid medium with two cylindrical fluorescent inclusions. As shown in Figure 29, the radiative power level entering the slab and exciting the fluorescent rods is considerably higher in the case of Hadamard multiplexed FT. Meanwhile, Hadamard multiplexing does not require complex changes to the configuration of the conventional FT system. The only requirement is that the system must be modified so that simultaneous illumination of multiple source locations is possible.

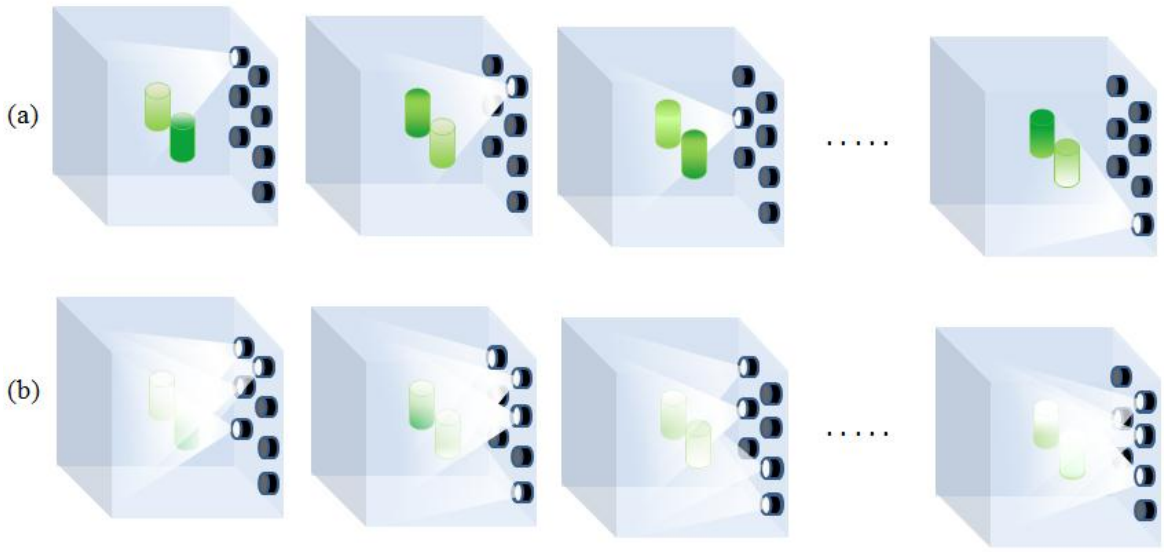


**Figure 29: In conventional FT depicted in row (a), one source illuminates the turbid medium at a time. In Hadamard multiplexed FT depicted in row (b), multiple sources illuminate the medium simultaneously while resulting in the same number of measurements but with higher SNR. The S-matrix Hadamard encoding is based on the seven-by-seven S-matrix in Equation 66.**

The linear model of FT, as formulated in Equation 26, changes with Hadamard multiplexing. The Hadamard multiplexed FT is described using the modified linear model below [103],

$$y = WMx\,, \tag{67}$$

where M is the system matrix defined in Equation 25, and W is the multiplexing matrix constructed from Hadamard S-matrix entries as follows

$$W = \begin{bmatrix} \mathrm{diag}_{n_d}(S_{11}) & \cdots & \mathrm{diag}_{n_d}(S_{1n_s}) \\ \vdots & \ddots & \vdots \\ \mathrm{diag}_{n_d}(S_{n_s1}) & \cdots & \mathrm{diag}_{n_d}(S_{n_sn_s}) \end{bmatrix}, \tag{68}$$

where $\mathrm{diag}_{n_d}(P)$ represents the square diagonal matrix of size $n_d$-by-$n_d$ having the scalar P as its diagonal entries. It must be noted that the Hadamard multiplexing scheme does not change the detector noise or modeling error statistics. According to Equation 67, the system matrix in the case of Hadamard multiplexed FT becomes WM. Therefore, as expected, the noise and error vector remains the same while the noiseless data vector, Mx, is amplified by W. This amplification in the noiseless data results in a boost in the data SNR. The multiplication of M by W also affects the condition number and singular values of the system matrix, which directly determine the condition of the ill-posed 3D reconstruction. However, Hadamard multiplexing is designed to have minimal effect on the condition number of the system matrix. More details regarding the conditioning of the Hadamard multiplexed FT inverse problem will be presented in Chapter 5.

## 4.4 Numerical Studies

To study the performance of Hadamard multiplexed FT, a set of 2D numerical studies (similar to the studies presented in Chapter 3) were performed. The 2D numerical studies are depicted in Figure 30. A rectangular 8 cm by 6 cm turbid medium (scattering

and absorption coefficients of 1 $mm^{-1}$ and 0.01 $mm^{-1}$, respectively) with two circular fluorescent inclusions was simulated using the forward solver described in Section 1.5. The turbid medium was illuminated with a varying number of sources distributed around its perimeter. The fluorescent signal is collected by 23 detectors. The acquired data was contaminated with various levels of noise resulting in data SNRs of 60, 50, 40, 30, 20, 10, and 0 dB to observe the effect of Hadamard multiplexing on the quality of FT reconstructions from high- to low-SNR data. This study was performed for cases with 7, 11, 15, 19, and 23 sources illuminating the medium, respectively, as shown in Figures 30 (a-i), 30 (b-i), 30 (c-i), 30 (d-i), and 30 (e-i) . This allows for investigation of the effect of the number of sources on the improvements offered by Hadamard multiplexed FT.

The reconstructions were performed by the MLS-AART which, as described in Section 2.3, is weakly regularizing compared to other inversion methods [103]. As a result, the poor quality of a reconstruction can be easily observed by checking the accuracy and artifact contamination level of the reconstructed image. The rows labeled (i) in Figure 30 represent the actual location and size of the fluorescent inclusions. The rows labeled (ii) in Figure 30 show the reconstruction by MLS-AART from conventional single-source illumination data. The rows labeled (iii) in Figure 30 show the reconstructions by MLS-AART from Hadamard multiplexed data. For high SNRs (60-40 dB), the reconstructions from single-source data and Hadamard multiplexed data are similar and the two blobs are successfully reconstructed from both datasets. As data SNR decreases below 40dB, the reconstructions from single-source data become inaccurate and contaminated with noise-induced impulses. However, the reconstructions from Hadamard multiplexed data remain considerably accurate down to 10 dB data SNR.

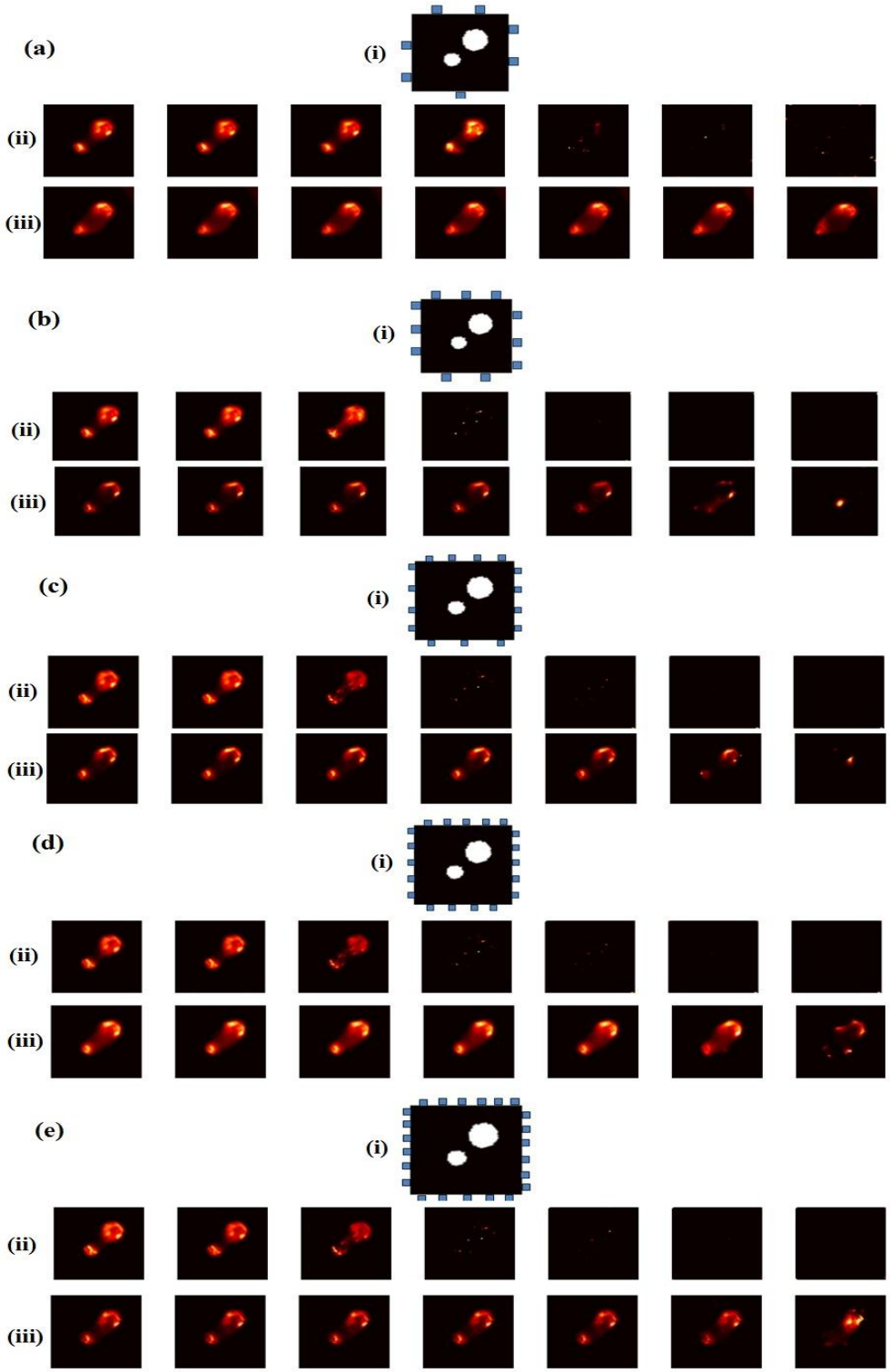


**Figure 30: A 2D FT scenario with a) 7, b) 11, c) 15, d) 19, and e) 23 sources illuminating the medium is simulated to assess the performance of Hadamard multiplexed FT. Reconstructions from ii) conventional single-source illumination and iii) Hadamard multiplexed data were performed using MLS-AART for data SNRs of 60, 50, 40, 30, 20, 10, and 0 dB from left to right respectively.**

Furthermore, the denoising power of Hadamard multiplexed FT increases when the number of sources illuminating the medium increases as suggested by the results presented in Figure 30. The reconstructions from Hadamard multiplexed data (corresponding to the study with 23 sources) presented in row (iii) of Figure 30 (e) demonstrate higher robustness to low SNR data compared to reconstructions presented in row (iii) of Figure 30 (b) (corresponding to the study with 11 sources) which lose accuracy below 30-20 dB SNRs. To compare the results presented in Figure 30 quantitatively, the relative mean square error (MSE) defined in Equation 64 associated with each reconstruction is plotted in Figure 31 [103].

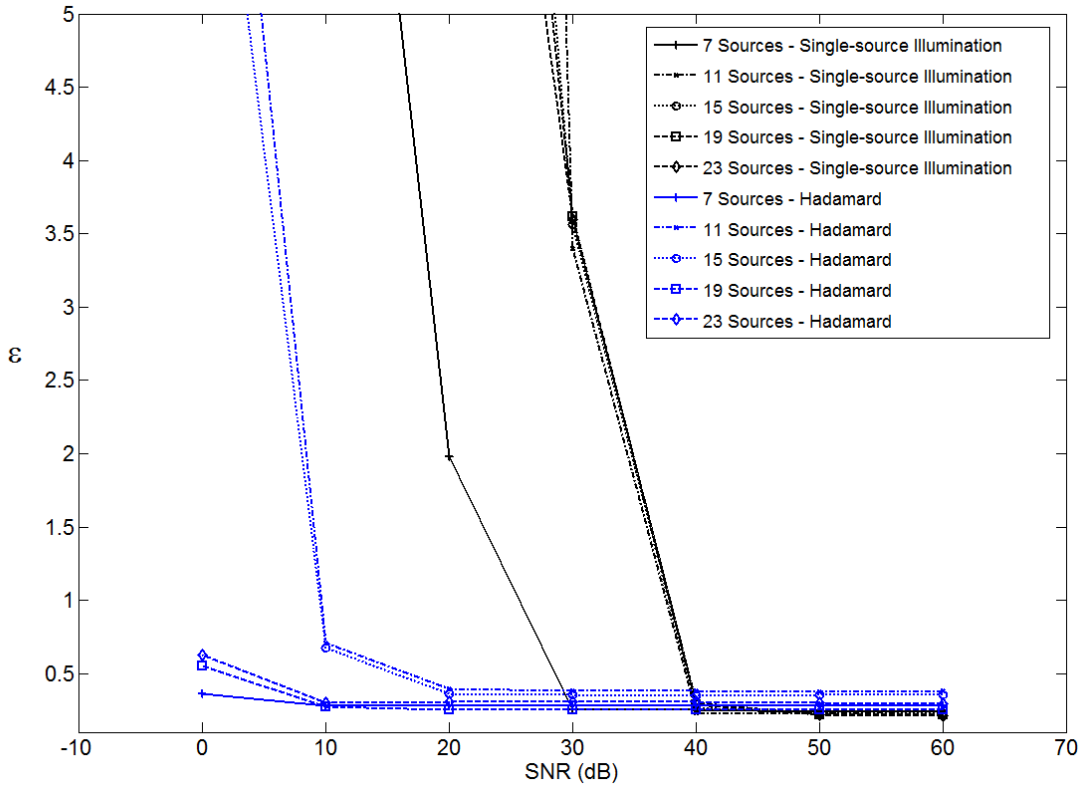


**Figure 31: The relative mean square errors (MSE) of the reconstructions in Figure 29 are plotted versus the data SNR.**

As shown in Figure 31, relative errors higher than five are not included within the borders of the graph. Based on the data presented in Figure 31, Hadamard multiplexing becomes considerably advantageous to single-source illumination as data SNR drops and number of sources increase. This was predicted by the theoretical discussions presented in Sections 4.1 and 4.2. For high-SNR cases (>40 dB), the relative errors for single-source studies are of the same order as that of Hadamard multiplexed studies. Meanwhile, in low-SNR studies, Hadamard multiplexed cases have relative errors below one down to SNRs of 10 dB and even 0 dB in some cases.

In summary, it can be concluded that Hadamard multiplexing greatly improves the accuracy of FT reconstructions in low-SNR cases provided that the number of sources used for illumination is sufficiently large. Additionally, for high-SNR cases, Hadamard multiplexing does not harm the quality of reconstructions and yields datasets with high levels of information content similar to single-source illumination systems.

# CHAPTER 5

# HADAMARD MULTIPLEXED FLUORESCENCE TOMOGRAPHY SYSTEM

It was shown in Chapters 2 and 3 that enhancement in the signal-to-noise ratio (SNR) of FT data improves the accuracy of the 3D reconstructions. Additionally, it was demonstrated in Chapter 4 that Hadamard multiplexing results in a considerable increase in the FT data SNR without a compromise to the condition of the inverse problem and while maintaining the simple instrumentation used for point-source illumination. In this chapter, the development and performance of a phantom-based Hadamard multiplexed FT system is described.

## 5.1 Noise in FT Systems

As discussed in Chapter 4, improvements in the FT data SNR have multiple benefits. Most importantly, the resolution and robustness of the 3D FT reconstructions become considerably enhanced. Also, FT-based imaging of highly absorbing organs and regions of animal and human subjects, such as the chest cavity or skull, becomes feasible as the level of noise contaminating the weak surface photons detected by the CCD drops with increase in the FT data SNR. Additionally, increase in FT data SNR results in faster FT scans as the required integration times for CCD image acquisition will be lower. This speed improvement in FT scan times can greatly enhance the quality of biological or drug studies with short anesthesia durations or experiments involving fluorescent agents with rapidly changing agent uptake.

Similar to other optical imaging and microscopy systems, FT systems are prone to different forms of noise and stray light interference and contamination. The noise in the

FT data can be caused by a variety of sources including the CCD noise, filter leakage, thermal radiation from system components such as motorized filter wheels, and auto-fluorescence of optical instruments and components such as optical posts or stages. While the noise from most of these sources can be corrected or removed by image post-processing or modifications to the system, the CCD noise is always present as it is caused by the internal dynamics of the CCD.

There are three major types of noise in CCDs: 1) read-out noise, 2) dark-current noise, and 3) shot noise. Read-out noise is a result of imperfections in the device-level electronic operations that convert the photon-induced electrons to electric signal in the CCD. Since this noise is generated during the read-out of the image from the CCD pixels, it is expressed as the total number of electrons RMS. Dark-current noise is caused by thermally generated electrons that contaminate the CCD pixels. Dark-current noise is present whether the CCD is exposed to light or not. Dark-current noise is expressed in terms of electrons per second per pixel. Shot noise, also referred to as photon noise or image noise, is caused by the randomness in the arrival of photons on the CCD pixels. The probability distribution associated with shot noise is Poisson. Shot noise level is independent of internal CCD operations and is a function of the number of photons collected by each CCD pixel. Consequently, shot noise is directly depends on the integration or image acquisition time.

Depending on various properties of an FT imaging scenario, all three major types of CCD noise can impair and limit the FT data SNR. The cooled CCD camera used in the experimental system described in Section 1.6 and depicted in Figure 4, which is a typical CCD camera used in FT systems, has the following noise statistics for a binning factor of

2x2 and exposure times of 0.11 sec to 3600 sec: the read-out noise is rated at 8.8 electrons RMS, and the dark-current noise is rated at 0.9 electrons per second per pixel. Also, the quantum efficiency spectrum of this CCD camera is depicted in Figure 32. For the purposes of imaging the emission of Oxazine-750 Perchlorate, the quantum efficiency of the CCD is rated around 0.8 at 700 nm.

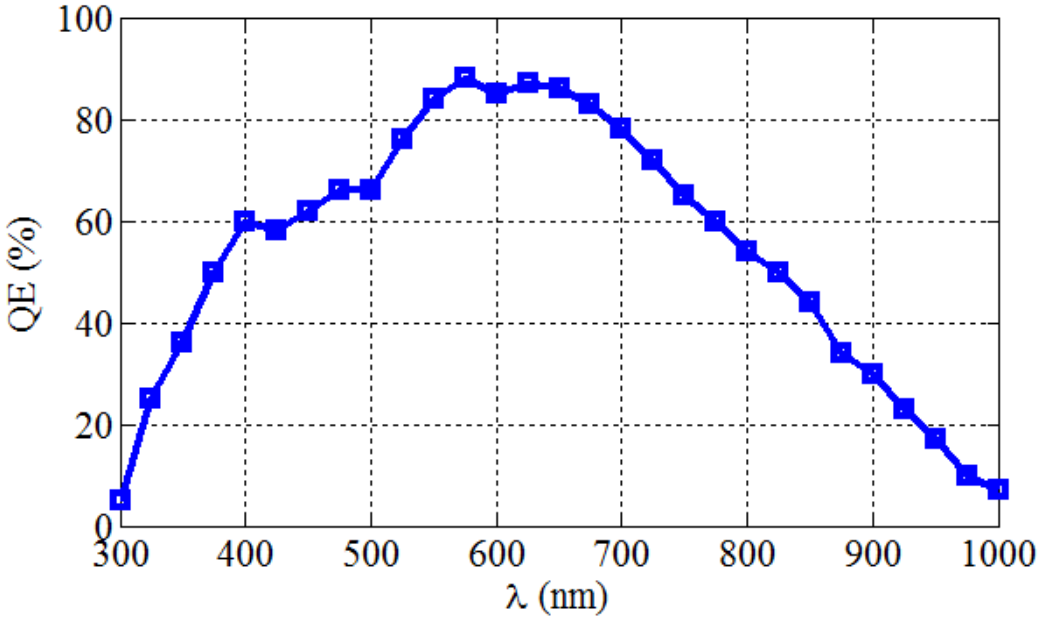


**Figure 32: The quantum efficiency (QE) spectrum of the CCD camera used in the FT system, which is described in Section 1.6 and depicted in Figure 4, peaks around 600 nm.**

Based on these CCD specifications and the Poisson distribution of shot noise, the CCD SNR can be computed as a function of exposure or integration time given the average radiance or maximum photon flux of the object being imaged. The graphs shown in Figure 33 contain plots of the CCD SNR as a function of the CCD integration time. The graph is Figure 33 (a) corresponds to imaging an object with photon flux of 50 photons per pixel per second (~$10^{-17}$ Watts/pixel at 700 nm). The graph in Figure 33 (b) corresponds to imaging an object with photon flux of $10^4$ photons per pixel per second

(~$10^{-17}$ Watts/pixel at 700 nm). So based on the plot in Figure 33 (a), for integration times of 0.1 sec to 100 sec, the CCD SNR goes from ~1 dB to ~21 dB for an incident flux of 50 photons/sec/pix. Similarly for the plot in Figure 33 (b), the CCD SNR goes from ~17 dB to ~31 dB for an incident flux of $10^4$ photons/sec/pix.

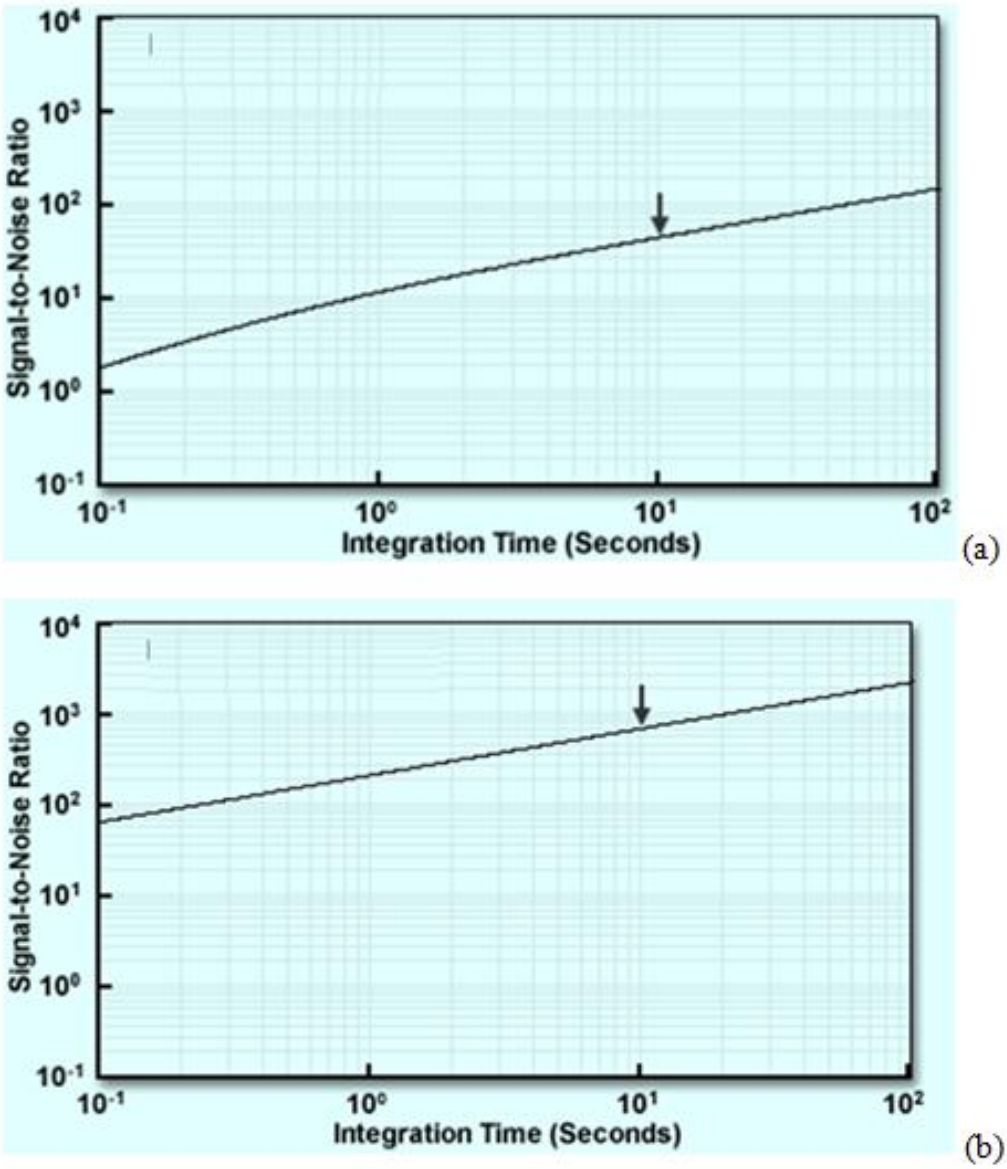


**Figure 33: The SNR of the CCD used in the FT system in Section 1.6 is plotted as a function of integration time for (a) image of an object with photon flux of 50 phot/sec/pix, and (b) image of an object with photon flux of 10000 phot/sec/pix.**

To bring these numbers into the context of FT scenarios, the first case (50 photons/sec/pix) corresponds to an FT scenario with single-point illumination irradiance of 1 $mW/mm^2$ and tissue optical scattering and absorption of 5 $mm^{-1}$ and 0.5 $mm^{-1}$, respectively. The second case ($10^4$ photons/sec/pix) corresponds to an FT scenario with single-point illumination irradiance of 1 $mW/mm^2$ and tissue optical scattering and absorption of 1 $mm^{-1}$ and 0.01 $mm^{-1}$, respectively. In better terms, the SNR plot in Figure 33 (a) corresponds to a typical FT imaging experiment in which maximum permissible illumination power is used to excite fluorophores in the chest cavity area of a small animal. The SNR plot in Figure 33 (b) corresponds to a typical FT imaging experiment in which maximum permissible illumination power is used to excite fluorophores in the thighs or abdominal area of a small animal.

The plots in Figure 33 indicate that for typical FT scenarios involving imaging of fluorescent agents buried in various regions of small animals, the CCD SNR will be below or around 30 dB unless the integration time for each image is raised to above 100 sec. As discussed in Chapters 3 and 4 and considering the reconstructions presented in Figures 23 and 30, the quality of FT reconstructions for SNRs of 30 dB or less are poor. Additionally, raising the image exposure time to above 100 sec results in very lengthy FT scan times that could outlast the effective anesthesia and dye uptake durations.

The FT noise analysis presented above indicates that in typical single-point illumination FT systems the inherent CCD noise can strongly limit the quality of 3D reconstructions. The proposed Hadamard multiplexed FT, as presented in the remainder of this chapter, can circumvent these limitations.

## 5.2 Outline of the Multiplexed FT System

Hadamard multiplexed FT, as described in Chapter 4, aims at increasing the SNR in FT data through replacing single-point illumination with multi-point illumination. The existing FT systems, as described in Section 1.6, employ translation stages to change the position of the tip of an optical fiber that is used to direct the laser or LED radiation to the turbid medium or animal subject. This configuration cannot be used for performing multi-point illumination. Although multi-point illumination is possible using a fiber bundle in contact with the turbid medium, such system can become complicated and costly as the number of source locations and the number of corresponding light sources coupled into the fibers increase. To realize Hadamard multiplexed FT, the translation stage-based FT scan must be replaced by a non-contact free-space design that allows for simultaneous illumination of source points.

In this work, a simple non-contact illumination configuration that allows for simultaneously flooding light on multiple points in the source grid was developed. As presented in Figure 34, after collimating, the NIR radiation passes through a masked lenslet array. The masks block lenslets corresponding to zero entries of the Hadamard S-matrix code while allowing radiation to pass through lenslets corresponding to unit entries. The image acquisition configuration is no different than existing non-contact systems in which the excitation trans-illumination and fluorescent emission are imaged to a cooled CCD by a lens and separated using a motorized filter wheel.

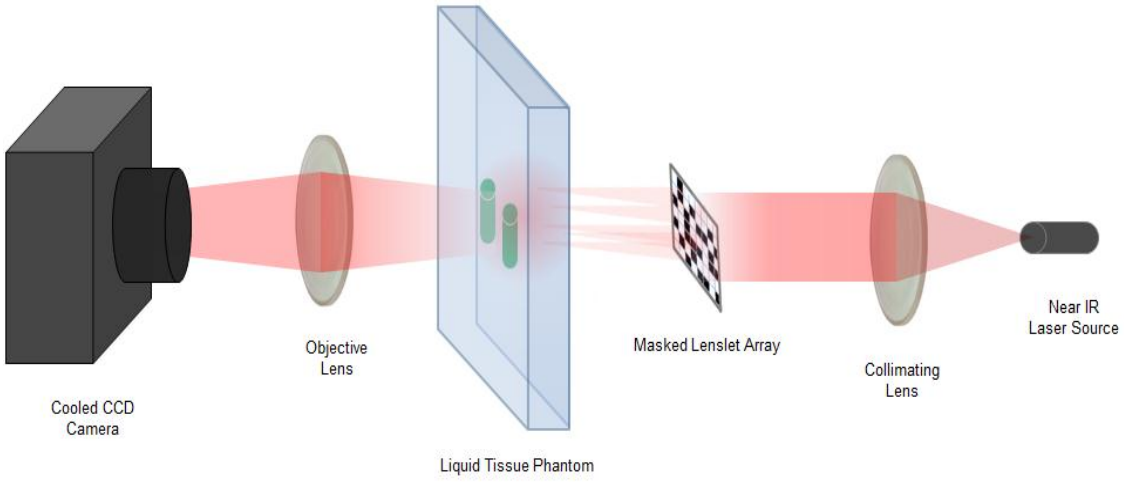


**Figure 34: In the phantom-based Hadamard-multiplexed FT system, radiation from a near infra-red laser is collimated into a beam using a lens and directed to a masked lenslet array that generates an array of point sources to illuminate the tissue phantom and excite the fluorescent tubes. The trans-illumination and the fluorescent signal are then collected by a CCD camera.**

As shown in Figure 34, laser radiation at the excitation wavelength of administered fluorophores is collimated into a beam with a waist of a few centimeters. The beam is directed at a rectangular lenslet array with lenslet dimensions of a few millimeters. Each lenslet focuses the beam on the surface of the small animal or phantom and so an array of point sources is generated. By sequential masking of the lenslet array, different Hadamard S-matrix codes can be realized. In addition to the advantages offered by Hadamard multiplexing, the non-contact illumination system has higher versatility, especially for non-flat geometries, compared to fiber-based systems. Furthermore, the proposed system possesses the same level of simplicity as point illumination FT systems and does not require complicated hardware such as spatial light modulators employed in surface illumination FT systems [104].

## 5.3 Masked Lenslet Array S-matrix Code Generation

It was discussed in Chapter 4 that the advantages offered by Hadamard multiplexing become evident as the number of sources increases and the detector SNR drops. In experimental demonstration of Hadamard multiplexed FT, a masked lenslet array is used for Hadamard S-matrix code generation. The masked lenslet array provides a cost-effective scheme for non-contact multi-point illumination. Also, the number of source locations can be varied by simply reconfiguring the masks to cover more or less lenslets. The masked lenslet configuration can be used to create point illumination (used in single-point illumination FT systems described in Section 1.6). To compare the performance of Hadamard multiplexed FT and single-point illumination FT, the power per area at every point source must be of the same level. This can be realized using a masked lenslet configuration in both single-point illumination and Hadamard multiplexed FT. The S-matrix masks are made by printing Hadamard S-matrix codes on transparencies and mounting them on the lenslet array. In Figure 35, a Hadamard S-matrix code of length 63 is used to make an FT Hadamard mask. The code is arranged in a 2D nine-by-seven array as shown in Figure 35 (a). The 2D array is printed on a transparency and mounted on an optical post to cover the lenslet array as shown in Figure 35 (b).

To construct and calibrate the lenslet-based multiplexing configuration, the configuration shown in Figure 35 (b) was illuminated using a laser to generate the corresponding masked multi-point illumination grid. A power detector was used to measure the radiative power in the illuminated points and the masked points. The module

was calibrated to avoid non-uniform distribution of radiative power among illuminated points while ensuring that the power leakage to masked points is negligible.

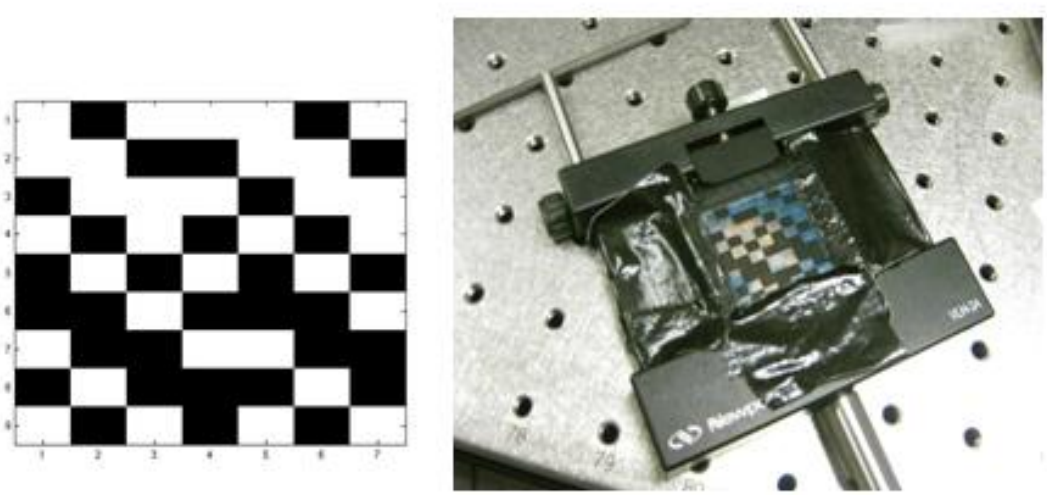

(a) (b)

**Figure 35: An optical mask is made from a Hadamard S-matrix code. a) Hadamard S-matrix code of length 63 is arranged in a 9-by-7 2D mask. b) The Hadamard S-matrix code is printed on a transparency and mounted on an optical post for to function as a mask in a Hadamard multiplexed FT system.**

## 5.4 Phantom-based Experimental Studies

The experimental studies performed to verify advantages of Hadamard multiplexed FT were carried out using a custom-built phantom-based system as shown in Figure 36. Collimated NIR beam of a 635 nm He:Ne continuous-wave laser passes through an engineered diffuser and an opening that functions as an aperture to limit the beam waist arriving at the lenslet array. The 9-by-7 unmasked lenslet array focuses the NIR beam into a grid of 63 points with a vertical pitch of 3 mm and horizontal pitch of 4 mm. The liquid phantom vessel is placed at the focal plane of the lenslet array so that its focal grid functions as a multi-point illumination pattern. As presented in Figures 36 (b) and 36 (c), S-matrix masks are mounted on the lenslet array to create Hadamard-coded multi-point illumination patterns on the phantom. Given the number of source locations,

63 Hadamard codes are used sequentially for the multiplexed FT scan. The liquid phantom used in the experimental studies is a water-based mixture of Intralipid-1% and India ink with scattering and absorption coefficients of 0.8 $mm^{-1}$ and 0.05 $mm^{-1}$ [40, 41]. The mixture is poured into a rectangular vessel with transparent plexiglass sides and dimensions of 120 mm by 90 mm by 14 mm. The fluorescent dye used in the phantom experiments is a dimethyl sulfoxide (DMSO)-based 100 μM solution of Oxazine 750 Perchlorate whose emission peaks around 700 nm when excited at 630 nm. Two capillary glass tubes with an inner diameter of 1 mm are partially filled with the fluorescent dye to form a pair of fluorescent cylinders with 1 mm diameter and 10 mm height.

The dye-filled tubes are suspended in the center of the liquid phantom by an optical post mounted on a translation stage for accurate positioning as depicted in Figure 36 (a). Using the translation stage, the dye-filled tubes are positioned at depths of 3 mm, 6 mm, and 9 mm from the front surface of the phantom vessel facing the camera. The trans-illumination and fluorescent emission are imaged from the front side of the phantom to a cooled CCD camera through a motorized filter wheel for separate acquisition of trans-illumination and emission images. The image acquisition is performed at a field of view (FOV) of 12 degrees with a binning factor of 4 and average exposure time of 15 sec⁄image. The CCD camera is cooled down to around −10 °C to minimize thermal noise effects. Dark-frame images (with laser off) are acquired in each measurement and subtracted from data images to correct for read-out noise, stray light effects, and other unwanted signals.

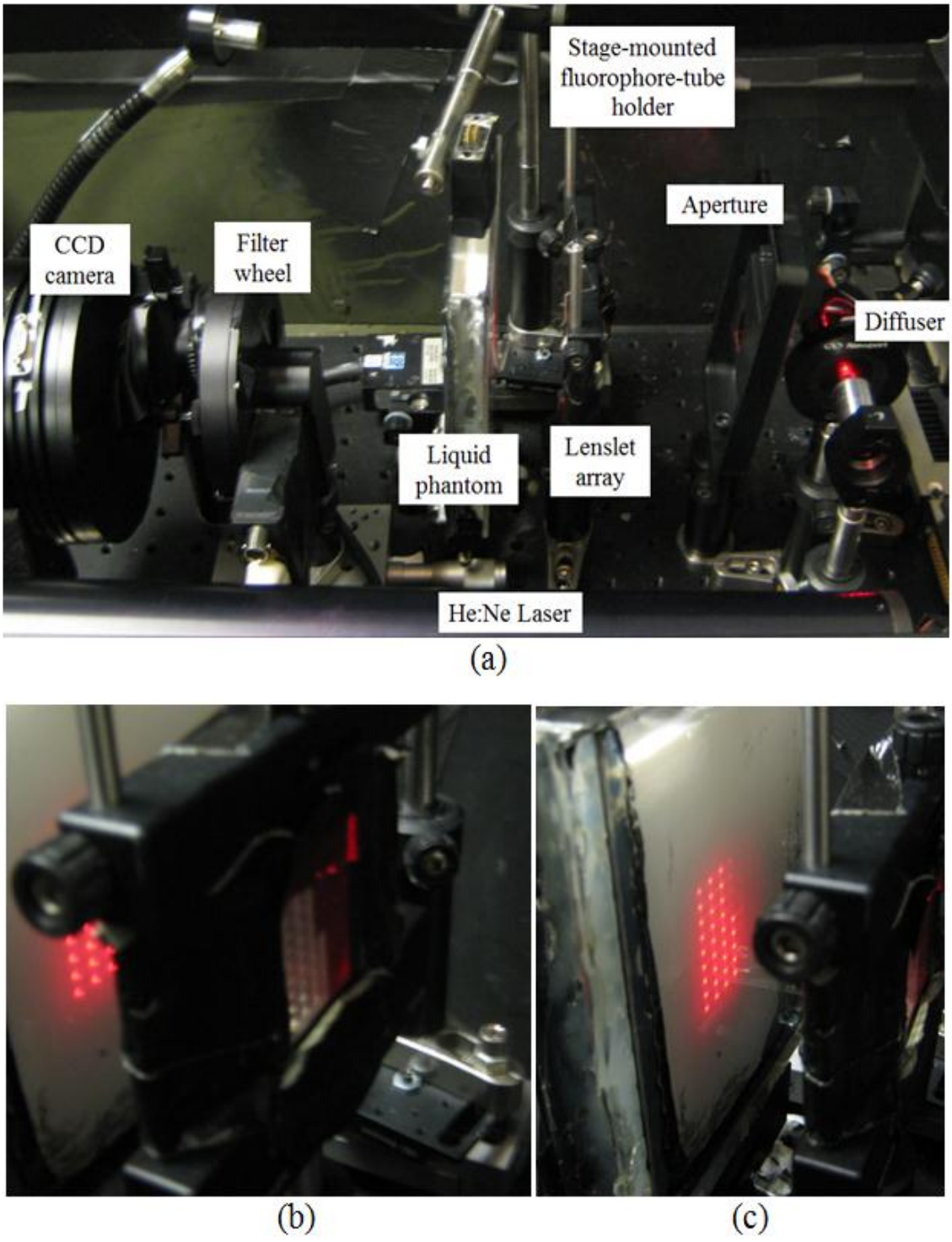


**Figure 36: Phantom-based Hadamard Multiplexed FT system: a) Picture of the experimental system. b) A Hadamard S-matrix mask mounted on a lenslet array is illuminated with collimated beam of NIR laser radiation. c) The S-matrix mask produces the desired excitation source pattern on the phantom surface.**

To compare the performance of the Hadamard-multiplexed FT architecture with existing single-point illumination systems, the phantom experiments were repeated with single-point illumination architecture by replacing the Hadamard coded masks with single-element masks to keep the per-point radiative illumination power constant between experiments. 3D reconstructions were performed on both sets of experimental studies by MLS-ART on a tetrahedral mesh discretizing the phantom volume with 132,325 nodes and 634,149 voxels. The results are presented in Figure 37 [105]. Rows labeled (a), (b), and (c) in Figure 37 correspond to inclusion depths of 3, 6, and 9 mm, respectively. Reconstructions from single-point illumination FT are presented in column (i), and those from Hadamard multiplexed FT in column (ii) of Figure 37.

As expected, the quality of the reconstructions deteriorates as the depth of the inclusions increases. While reconstructions of shallow inclusions (3 mm) from both single-illumination and multiplexed data have a reasonable level of accuracy as shown in Figure 37 (a), the advantage of Hadamard multiplexed FT in enhancing robustness becomes evident as the depth of inclusions increases. Similar to numerical studies, it can be observed that Hadamard multiplexing adds considerable robustness to 3D reconstructions particularly for deeper inclusions as the data will be more noise-sensitive.

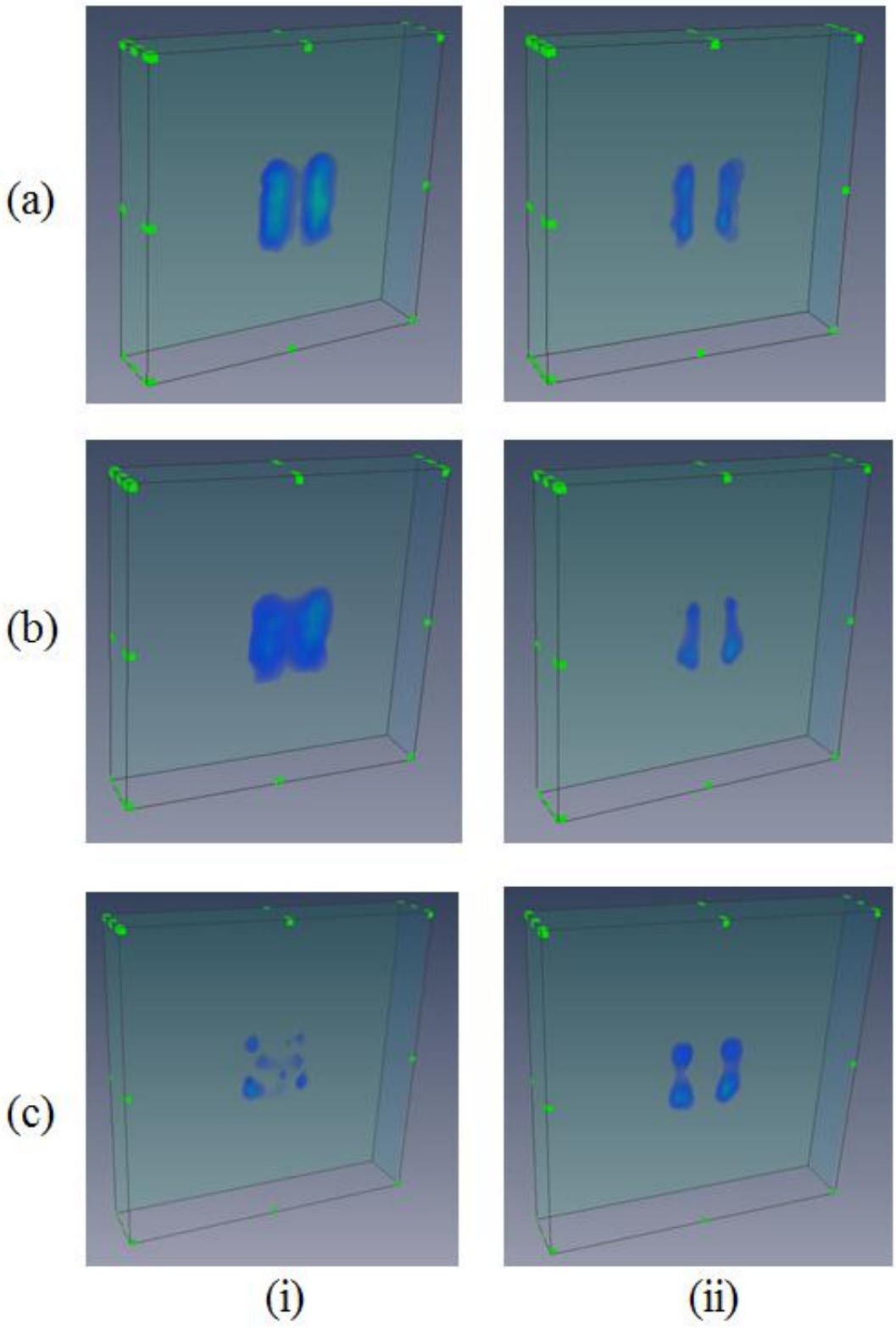


**Figure 37: Phantom-based experimental results: 3D reconstructions performed by MLS-ART on i) conventional single-point illumination phantom FT data, and ii) Hadamard-multiplexed FT data when the depth of the pair of fluorescent tubes is a) 3 mm, b) 6 mm, and c) 9 mm from the phantom surface facing the camera.**

## 5.5 Discussion

In this work, a multiplexing scheme built upon Hadamard S-matrix codes was studied to replace the existing single-point illumination in FT with multi-point illumination to increase the SNR and throughput in FT systems and reduce the required tomographic scan times. The high cost of wide-band tunable high-power light sources and per-area illumination power limitations in *in vivo* optical imaging pose considerable challenges for developing high-throughput high-SNR FT systems. Hadamard multiplexing allows us to overcome these challenges without over-complicating the architecture of the FT system or making them significantly costlier. Hadamard multiplexing provides the optimal trade-off between the throughput (SNR) and information content of a set of measurements. As discussed in Chapter 4, single-illumination FT measurements enjoy high information content because of their spatially disjoint sensitivity maps while suffering from low-throughput that limits their accuracy and optimal performance to scenarios with thin or low absorptive tissues. Hadamard multiplexed FT offers the optimal trade-off where by minimally jeopardizing the information content of the measurements, a considerable boost in the measurement SNR and throughput is obtained.

As shown in Figures 30 and 37, the 2D and 3D FT reconstructions indicate that for low-noise FT scenarios with shallow inclusions, the performance of single-point illumination architecture is not significantly different from Hadamard-multiplexed architecture. Due to changes in the system matrix, its condition number, and singular values, along with changes in the experimental setup, the reconstructions from single-point illumination data in both numerical and phantom studies differ from reconstructions

from Hadamard-multiplexed data, even for low-noise FT scenarios, as presented in Figures 30 and 37. The difference between the two, however, becomes more significant as the noise level and depth of the inclusions increases. The data from deeper inclusions is more diffuse and hence more sensitive to and affected by noise contamination. The accuracy of reconstructing shallow sources from low-noise data is high and in the same order of magnitude for both architectures as shown in the reconstruction error plots of Figure 31. This shows that though the condition of system matrix is affected by Hadamard multiplexing, the reconstruction accuracy is very little jeopardized if any. This is in part due to the low condition number of Hadamard S-matrices. The condition numbers corresponding to S-matrices of sizes 7, 15, 23, 31, and 63 are 2.82, 4, 4.89, 5.65, and 8, respectively. These condition numbers are significantly low compared to the typical condition number of the system matrix in FT, which can range from around $10^{10}$ to above $10^{20}$ depending on the geometry and optical properties of the turbid medium. As a result, when multiplied by the multiplexing matrix, W, as formulated in Equations 67 and 68, the condition and singular values of the FT system matrix M do not change significantly. Hence, the FT reconstruction accuracy is jeopardized quite insignificantly with Hadamard multiplexing.

The advantage of Hadamard multiplexed FT becomes evident as the data noise level, inclusion depth, and number of FT sources increase. This can be observed in the comparative trend of 2D and 3D reconstructions and their relative errors in Figures 30, 31, and 37. In numerical studies, as the FT data SNR decreases to ~30 dB and below, the reconstructions from single-point illumination data completely lose their accuracy and become dominated by artifacts. Meanwhile, reconstructions from Hadamard-multiplexed

data preserve their accuracy down to a noise level equivalent to ~10 dB single-point data SNR. In phantom studies, as the depth of the two fluorescent rods increases, the corresponding FT data becomes more diffuse, and hence the 3D reconstruction more ill-posed and noise-sensitive. As a result, though the noise characteristics of the CCD remain approximately the same (dark, read-out, and image noise), artifact contamination in the reconstructions increases with depth. Hadamard multiplexing offers improved robustness in reconstructing the rods at 9 mm depth over single-point illumination architecture as shown in Figure 37.

Consequently, Hadamard multiplexed FT can greatly enhance the performance of FT systems especially when suffering from limited illumination power or in imaging scenarios dealing with highly absorbing organs, such as the liver or the lungs in small animals. In this work, full Hadamard S-matrix multiplexing was proposed and studied for FT systems. Nevertheless, partial Hadamard multiplexing of the FT illumination architecture can also offer benefits over existing systems. In partial multiplexing, the illumination grid points are divided into groups (e.g., each grid line forms a group of 5 points), and the S-matrix multiplexing is applied to these groups instead of individual illumination points. In FT systems with limited flexibility over modification of the illumination geometry and optics (such as commercial FT systems that use translation stage-based illumination raster scan), partial Hadamard multiplexing can be used to boost the throughput by simply adding one illumination (and a stage) per each line of the illumination grid. Depending on the degree of partial multiplexing (the total number of multiplexed entities or groups), the data SNR and system throughput can be improved over single-point illumination systems. In other FT systems where optical fiber bundles

are used for raster scanning the illumination points, full S-matrix multiplexing can be implemented by simply re-programming the illumination sequence of light sources coupled to the fibers.

In summary, it was shown that the proposed Hadamard multiplexed architecture greatly improves the accuracy and robustness of FT reconstructions in low-SNR scenarios provided that the number of sources used for illumination is sufficiently large. Additionally, for high-SNR cases, Hadamard multiplexing does not harm the quality of the reconstructions. Modifications to the existing FT system architecture required by full or partial Hadamard multiplexing do not add considerable complexity or cost to these systems, unlike recently explored surface illumination FT schemes [104]. These overall characteristics of Hadamard multiplexed FT, as demonstrated in this work, make it considerably advantageous over existing single-point illumination FT systems.

# CHAPTER 6

# CONCLUSIONS AND SUGGESTED FUTURE WORK

In this chapter, the major contributions and conclusions of this thesis are presented and summarized in Section 6.1. Additionally, the possible future directions and extensions to the research discussed in this thesis are discussed in Section 6.2. The suggested future extensions include further joint optimization, improvement, and enhancement of the reconstruction algorithm and the hardware of the non-contact fluorescence tomography system.

## 6.1 Conclusions

The main focus of this research has been the development and implementation of a robust Hadamard multiplexed fluorescence tomography (FT) system. The first course of action was the development and characterization of the software and hardware of a non-contact continuous-wave trans-illumination fluorescence tomography system. The developed system was used to demonstrate the limitations of the existing FT reconstruction algorithms, namely $L_2$ regularization and MLS-ART. Additionally, two subsystems were developed to characterize the scattering and absorption agents used in the liquid tissue phantom employed in the non-contact FT system. An information-theoretic approach was applied to the FT system to optimize the binning of the data images.

The next step was the development of the TV regularization algorithm for performing edge-preserving 3D reconstructions in FT. Two different implementations of the TV regularization were applied to 2D numerical studies and phantom-based experimental studies of FT. Using the concept of PSFs, I demonstrated that the edge-

preserving property of the TV regularization results in higher spatial resolution in the 3D reconstructions compared to $L_2$ regularization. I also demonstrated that the quality of 3D reconstructions from all inverse solvers deteriorates as the noise level in the FT data increases. This increase results in various forms of artifacts and errors contaminating the 3D reconstructions of inverse solvers.

To address the issue of artifact contamination in 3D reconstructions from noisy data, I developed and implemented a Hadamard multiplexed FT system that can increase the data SNR by orders of magnitude. I demonstrated that multiplexing the FT sources can add significant robustness in 3D reconstructions against data noise. To demonstrate the advantages of Hadamard multiplexed FT, I performed 2D numerical studies for a range of data SNRs and analyzed the reconstruction error. The Hadmard multiplexed reconstructions maintained accuracy for SNRs as low as 10 dB, whereas the single-point illumination reconstructions lost accuracy below 30 dB. Additionally, I developed a custom-build phantom-based Hadamard multiplexed FT system using a masked lenslet array architecture. The experimental studies performed using this system indicated that Hadamard multiplexing can significantly improve the reconstructions of deep sources in FT.

A brief summary of my main contributions in this research is as follows:

- I analyzed the limitations and drawbacks of ART and $L_2$ regularization in performing 3D FT reconstructions.
- I developed, implemented, and applied the first TV regularization algorithm used for 3D reconstructions in FT.

- I presented the first comparative analysis of the spatial resolution of reconstructions from $L_2$ regularization and TV regularization using PSFs.
- I developed the first Hadamard transform approach to multi-point illumination FT.
- I developed and implemented the first Hadamard multiplexed FT system that offers the highest FT data SNR.

## 6.1 Suggestions for Future Work

Throughout this thesis, I have presented algorithmic and system improvements for the enhancement of the quality, accuracy, and resolution of the 3D reconstructions in FT. These improvements can result in a new range of applications and capabilities for FT, provided that they do not jeopardize the speed, complexity, and cost of the FT systems. The suggested future extensions of this research can potentially improve the speed, memory efficiency, and cost of the existing FT systems and the system developed in this work.

In Chapters 2 and 3, the row-action memory efficient MLS-ART and the edge-preserving TV regularization algorithms were presented and studied. As discussed in Section 4.1, the advantage of MLS-ART is in speed, memory efficiency, and lack of parameter selection or optimization requirements. This speed and memory advantage is due to the row-action nature of MLS-ART. Unlike regularization techniques where matrix computations must be carried out, in MLS-ART only vector computations are performed in each step. Meanwhile, the TV regularization has the advantage of higher spatial resolution and robustness. This resolution advantage stems from the use of TV semi-norm as the penalty term in the optimization. However, the convergence time for TV regularization is considerably higher than that for MLS-ART.

Considering the advantages of these two algorithms, a future extension of this research can be the development of a row-action edge-preserving reconstruction algorithm. The development of an ART-type algorithm where only vector computations are carried out but the TV semi-norm is used instead of the $L_2$ norm can lead to a speedy memory-efficient edge-preserving inverse solver. Consequently, such algorithm can possess the combined advantages of MLS-ART and TV regularization.

Furthermore, in many FT imaging scenarios, *a priori* information is available for improving the accuracy of the 3D reconstructions. A widely studied scenario is early cancer detection where lesions are small in size and hence sparsely distributed over the tissue. It has been shown that the sparsity-driven $L_1$ regularization offers stable and accurate reconstructions in this scenario [62]. However, similar to TV regularization, solving the nonlinear optimization problem posed by $L_1$ regularization can be computationally costly, often inaccurate due to multitude of local minima. As a result, developing an effective correction scheme to incorporate structural, anatomical, and spatial priors into regularized reconstruction algorithms can greatly improve the use of *a priori* information in FT reconstructions. The kernel correction approach has been shown to provide a framework within which constraints and priors can be incorporated into a regularization method without jeopardizing the data fidelity or the complexity of the problem [106]. As a future extension of this research, the kernel correction technique can be used to implement a joint TV, $L_2$ and $L_1$ regularization technique for robust edge-preserved sparse FT reconstructions.

In Section 5.1, the CCD noise contaminating the FT data was discussed and analyzed. It was shown that for high-SNR FT data acquisition, both the required cost and scan time

will become excessively high. Additionally, the bulk of data acquired in non-contact FT systems and used in reconstruction algorithms is tremendously large compared to fiber-based systems. Similar to many imaging and microscopy systems, post-processing of the FT data images can further denoise and compress the data to enhance the SNR and decrease memory requirements. It has been shown that FT data are compressible in Battle-Lemarie wavelets [107, 108]. As a result, FT images can be compressed and represented in terms of the corresponding wavelet coefficients rather than pixel-by-pixel images. As a future extension of this research, this compression can be performed on acquired FT images, and the use of the wavelet coefficients in the FT reconstructions algorithm, instead of the pixel-by-pixel data vectors, can be studied. This approach can downsize the computational bulk of the reconstruction algorithm. Also, the data will be automatically denoised through the operation of compression, as the negligibly small wavelet coefficients, corresponding to non-smooth components of the data, will be filtered out.

# APPENDIX A

# COMPUTATIONAL DETAILS OF TV REGUALRIZATION ALGORITHMS

Iterative split Bregman total variation regularization algorithm pseudo-code is as follows:

1. $u_{L2} = T^*(M^*M + \lambda^2 I)^{-1}M^*y$
2. *Initialize* $u^0 = T^*M^*y$
3. *While* $\frac{\|u^{k+1}-u^k\|}{\|u^k\|} < eps$

    3.1 $u^{k+1} = PCG\big(\mu T^*M^*MT(u) + \alpha I - \beta\Delta,\ \mu T^*M^*f + \alpha u_{L2} + \beta\nabla_{\mathrm{x}}^{\mathrm{T}}(d_x^k - b_x^k) + \beta\nabla_{\mathrm{y}}^{\mathrm{T}}\big(d_y^k - b_y^k\big) + \beta\nabla_{\mathrm{z}}^{\mathrm{T}}(d_z^k - b_z^k)\big)$

    3.2 *Map u to a cubic mesh by interpolation*

    3.3 $s^k = \sqrt{\left|b_x^k + \nabla_{\mathrm{x}}u^k\right|^2 + \left|b_y^k + \nabla_{\mathrm{y}}u^k\right|^2 + |b_z^k + \nabla_{\mathrm{z}}u^k|^2}$

    3.4 $d_x^{k+1} = \max(s^k - \frac{1}{\lambda}, 0)\frac{\nabla_{\mathrm{x}}u^k + b_x^k}{s^k}$

    3.5 $d_y^{k+1} = \max(s^k - \frac{1}{\lambda}, 0)\frac{\nabla_{\mathrm{y}}u^k + b_y^k}{s^k}$

    3.6 $d_z^{k+1} = \max(s^k - \frac{1}{\lambda}, 0)\frac{\nabla_{\mathrm{z}}u^k + b_z^k}{s^k}$

    3.7 $b_x^{k+1} = b_x^k - d_x^{k+1} + \nabla_{\mathrm{x}}u^{k+1}$

    3.8 $b_y^{k+1} = b_y^k - d_y^{k+1} + \nabla_{\mathrm{y}}u^{k+1}$

    3.9 $b_z^{k+1} = b_z^k - d_z^{k+1} + \nabla_{\mathrm{z}}u^{k+1}$

    3.10 *Map u to a tetrahedral mesh by interpolation*

4. *End*
5. $x^{final} = T\,u^{(k+1)}$

Iterative ROF total variation regularization algorithm pseudo-code is as follows.

1. *Initialize* $u^{(0)} = T^*(M^*M + \lambda^2 I)^{-1} M^* y$
2. *While* $\frac{\|u^{n+1} - u^n\|}{\|u^n\|} < eps$
   2.1 *Map u to a cubic mesh by interpolation*
   2.2 *Approximate* $[u_x\ u_y\ u_z\ u_{xy}\ u_{xx}\ u_{yy}\ u_{xz}\ u_{yz}\ u_{zz}]$ *using finite difference*
   2.3 *Set d* = $\frac{u_x^2 u_{yy} + u_x^2 u_{zz} + u_y^2 u_{xx} + u_y^2 u_{zz} + u_z^2 u_{xx} + u_z^2 u_{yy} - 2(u_x u_y u_{xy} + u_x u_z u_{xz} + u_z u_y u_{zy})}{(u_x^2 + u_y^2 + u_z^2)^{1.5}}$
   2.4 *Map u to a tetrahedral meshby interpolation*
   2.5 $u^{(n+1)} = u^{(n)} + \Delta t\ (T^* M^*\ (y - MT(u)) + \lambda\, d\ )$
   2.6 $u^{(n+1)} = max(0, u^{(n+1)})$
3. *End*
4. $x^{final} = T\, u^{(n+1)}$

# REFERENCES


[1] R. Weissleder, J. M. Wittenberg, M. G. Harisinghani, Primer of Diagnostic Imaging, Mosby, Philadelphia (2003).

[2] V. Ntziachristos, A. Leroy-Willig, B. Tavitian, Textbook of in vivo Imaging in Vertebrates, Wiley, NY (2007).

[3] R. Weissleder, B. D. Ross, A. Rehemtulla, S. S. Gambhir, Molecular Imaging, Principles and Practice, People's Medical Publishing House, Connecticut (2010).

[4] R. Weissleder, "Molecular imaging in cancer," Science 312, 1168–1171 (2006).

[5] M. Rudin, and R. Weissleder, "Molecular imaging in drug discovery and development," Nature Review Drug Discovery 2, 123–131 (2003).

[6] G. Muller, B. Chance, R. R. Alfano, S. R. Arridge, J. Beuthan, E. Gratton, M. F. Kaschke, B. R. Masters, S. Svanberg, P. van der Zee, Medical Optical Tomography: Functional Imaging and Monitoring, SPIE, Bellingham, WA (1993).

[7] B. Chance, K. Kang, H. He, E. Sevick, "Highly sensitive object location in tissue models with linear in-phase and anti-phase multi-element optical arrays in one and two dimensions," Proceedings of the National Academy of Sciences, USA 90, 3424–3427 (1993).

[8] K. M. Yoo, F. Nliu, and R. R. Alfano, "Biological materials probed by the temporal and angular profiles of backscattered laser pulses," Journal of Optical Society of America B 7, 1685-1693 (1990).

[9] J. C. Hebden, and K. S. Wong, "Time-resolved optical tomography," Applied Optics 32, 372-380 (1993).

[10] V. Ntziachristos, C. H. Tung, C. Bremer, R. Weissleder, "Fluorescence molecular tomography resolves protease activity in vivo," Nature Medicine 8, 757–760 (2002).

[11] C. H. Contag, S. D. Spilman, P. R. Contag, M. Oshiro, B. Eames, P. Dennery, D. K. Stevenson, D. A. Benaron, "Visualizing gene expression in living mammals using a bioluminescent reporter," Photochemistry and Photobiology 66,523–531 (1997).

[12] S. Ke, X. Wen, M. Gurfinkel, C. Charnsangavej, S. Wallace, E. M. Sevick-Muraca, and C. Li, "Near-infrared optical imaging of epidermal growth factor receptor in breast cancer xenografts," Cancer Research 63, 7870–7875 (2003).

[13] S. Kwon, S. Ke, J. P. Houston, W. Wang, Q. Wu, C. Li, and E. M. Sevick-Muraca, "Imaging dose-dependent pharmacokinetics of an RGD-fluorescent dye conjugate targeted to alpha v beta 3 receptor expressed in Kaposi's sarcoma," Molecular Imaging 4, 75–87 (2005).

[14] D. R. Vera, D. J. Hall, C. K. Hoh, P. Gallant, L. M. McIntosh, and R. F. Mattrey, "Cy5.5-DTPA-galactosyl-dextran: a fluorescent probe for in vivo measurement of receptor biochemistry," Nuclear Medicine and Biology 32, 687–693 (2005).

[15] R. Weissleder, and V. Ntziachristos, "Shedding light onto live molecular targets," Nature Medicine 9, 123-128 (2003).

[16] K. E. Adams, S. Ke, S. Kwon, F. Liang, Z. Fan, Y. Lu, K. Hirschi, M. E. Mawad, M. A. Barry, E. M. Sevick-Muraca, "Comparison of visible and near-infrared wavelength-excitable fluorescent dyes for molecular imaging of cancer," Journal of Biomedical Optics, 12, 020417-1–024017-9 (2007).

[17] A. Corlu, R. Choe, T. Durduran, M. A. Rosen, M. Schweiger, S. R. Arridge, M. D. Schnall, A. G. Yodh, "Three-dimensional in vivo fluorescence diffuse optical tomography of breast cancer in humans," Optics Express 15, 6696-6716 (2007).

[18] N. Panchuk-Voloshina, R. Haugland, J. Bishop-Stewart, M. Bhalgat, P. Millard, F. Mao, W. Leung, and R. Haugland, "Alexa dyes, a series of new fluorescent dyes that yield exceptionally bright, photostable conjugates," Journal of Histochemistry and Cytochemistry 9, 1179–1188 (1999).

[19] M. Hassan, J. Riley, V. Chernomordk, P. Smith, R. Pursley, S. B. Lee, J. Capala, A. H. Gandjbakhche, "Fluorescence lifetime imaging system for in vivo studies," Molecular Imaging 6, 229–236 (2007).

[20] S. R. Arridge, and J. C. Hebden, "Optical imaging in medicine: II. Modelling and reconstruction" Physics in Medicine and Biology 42, 841–53 (1997).

[21] A. Joshi, J. C. Rasmussen, E. M. Sevick-Muraca, T. A. Wareing, J. McGhee, "Radiative transport-based frequency-domain fluorescence tomography," Physics in Medicine and Biology 53, 2069–2088 (2008).

[22] L. D. Montejo, A. D. Klose, A. H. Hielscher, "Implementation of the equation of radiative transfer on block-structured grids for modeling light propagation in tissue," Biomedical Optics Express 1, 861-878 (2010).

[23] D. Contini, F. Martelli, and G. Zaccanti, "Photon migration through a turbid slab described by a model based on diffusion approximation: I. Theory" Applied Optics 36, 4587–99 (1997).

[24] S. R. Arridge, and J. C. Schotland, "Optical tomography: forward and inverse problems," Inverse Problems 25, 123010 (2009).

[25] M. A. Oleary, D. A. Boas, X. D. Li, B. Chance, and A. G. Yodh, "Fluorescence lifetime imaging in turbid media," Optics Letters 21, 158 –160 (1996).

[26] D. Y. Paithankar, A. U. Chen, B. W. Pogue, M. S. Patterson, and E. M. Sevick-Muraca, "Imaging of fluorescent yield and lifetime from multiply scattered light reemitted from random media," Applied Optics 36, 2260–72 (1997).

[27] J. P. Houston, A. B. Thompson, M. Gurfinkel, and E. M. Sevick-Muraca, "Sensitivity and depth penetration of continuous wave versus frequency-domain photon migration near-infrared fluorescence contrast-enhanced imaging," Photochemistry and Photobiology 77, 420–30 (2003).

[28] V. Ntziachristos, "Fluorescence molecular imaging," Annual Review Biomedical Engineering 8, 1-33 (2006).

[29] M. Schweiger, S. R. Arridge, M. Hiraoka, and D. T. Delpy, "The finite element method for the propagation of light in scattering media: boundary and source conditions," Medical Physics 22 1779–92 (1995).

[30] C. A. Parker, and W. T. Rees, "Correction of fluorescence spectra and measurement of fluorescence quantum efficiency," Analyst 85,587-601 (1960).

[31] G. Arfken, Mathematical methods for physicists, Academic Press, NY (1970).

[32] S. R. Arridge, M. Cope, and D. T. Delpy, "Theoretical basis for the determination of optical pathlengths in tissue: Temporal and frequency analysis," Physics in Medicine and Biology 37, 1531–1560 (1992).

[33] C. Kuo, O. Coquoz, T. L. Troy, H. Xu and B. W. Rice, "Three-dimensional reconstruction of in vivo bioluminescent sources based on multispectral imaging," Journal of Biomedical Optics 12, 24007 (2007).

[34] D. A. Boas, J. P. Culver, J. J. Stott, and A. K. Dunn, "Three dimensional Monte Carlo code for photon migration through complex heterogeneous media including the adult human head," Optics Express 10, 159–69 (2002).

[35] S. R. Arridge, M. Schweiger, M. Hiraoka, and D. T. Delpy, "Finite element approach for modelling photon transport in tissue," Medical Physics 20, 299–309 (1993).

[36] G. Strang, and G. Fix, An Analysis of The Finite Element Method: Prentice Hall, NJ (1973).

[37] H. Jiang, "Frequency-domain fluorescent diffusion tomography: a finite-element based algorithm and simulations," Applied Optics 37, 5337-5343, (1998).

[38] H. Dehghani, M. E. Eames, P. K. Yalavarthy, S. C. Davis, S. Srinivasan, C. M. Carpenter, B. W. Pogue, and K. D. Paulsen, "Near infrared optical tomography using NIRFAST: Algorithm for numerical model and image reconstruction," Communications in Numerical Methods in Engineering 25, 711-732 (2009).

[39] V. Ntziachristos, and R. Weissleder, "Experimental three-dimensional fluorescence reconstruction of diffuse media using a normalized born approximation," Optics Letters 26, 893–895 (2001).

[40] R. Cubeddu, A. Pifferi, P. Taroni, A. Torricelli, and G. Valentini, "A solid tissue phantom for photon migration studies," Physics in Medicine and Biology 42 1971–9, (1997).

[41] S. T. Flock, S. L. Jacques, B. C. Wilson, W. M. Star, and M. J. van Gemert, "Optical properties of Intralipid: a phantom medium for light propagation studies," Lasers in Surgery and Medicine 12 , 510-519 (1992).

[42] B. W. Pogue, and G. Burke, "Fiber optic bundle design for quantitative fluorescence measurement from human tissue," Applied Optics 37, 7429–7436 (1998).

[43] T. M. Cover, and J. A. Thomas, Elements of Information Theory, Wiley, NY (2006).

[44] I. E. Telatar, "Capacity of multi-antenna Gaussian channels," European Transactions on Telecommunications 10, 585–596 (1999).

[45] P. Mohajerani, A. Behrooz, and A. Adibi, "An Information-theoretic Treatment of Fluorescent Molecular Tomography," Proceedings of SPIE 7174, 717413 (2009).

[46] G. Strang, Linear Algebra and Its Applications, Brooks Cole, CA (2005).

[47] A. Bjorck, Numerical Methods for Least Squares Problems, SIAM, Philadelphia, (1996).

[48] G. H. Golub, and C. F. van Van Loan, Matrix Computations, Johns Hopkins University Press, MD (1996).

[49] P. C. Hansen, Discrete inverse problems: insight and algorithms, SIAM, Philadelphia, (2010).

[50] J. Chung, G. Easley, and D. P. O'Leary, "Windowed Spectral Regularization of Inverse Problems," SIAM Journal of Scientific Computation 33, 3175–3200 (2011).

[51] J. K. Cullum, and R. A. Willoughby, Lanczos Algorithms for Large Symmetric Eigenvalue Computations: Theory, SIAM, Boston (2002).

[52] R. C. Aster, B. Borchers, and C. H. Thurber, Parameter Estimation and Inverse Problems, Academic Press, NY (2004).

[53] C. Lawson, and R. Hanson, Solving Least Squares Problems, Englewood Cliffs, Prentice Hall, NJ (1974).

[54] V. G. Romanov, S. I. Kabanikhin, and A. L. Bukhgeim, Ill-posed and Inverse Problems, VSP Intl Science, Netherlands (2003).

[55] A. A. Samarskii, and P. N. Vabishchevich, Numerical Methods for Solving Inverse Problems of Mathematical Physics, VSP, Utrecht (2007).

[56] A. N. Tikhonov, "On the solution of ill-posed problems and a method of regularization," Doklady Akademii Nauk 151, 501-504, (1963).

[57] H. W. Engl, M. Hanke and A. Neubauer, Regularization of Inverse Problems, Kluwer Academic Publisher, Dordrecht (1996).

[58] P. C. Hansen, Rank-Deficient and Discrete Ill-Posed Problems: Numerical Aspects of Linear Inversion, SIAM, Philadelphia (1997).

[59] S. C. Davis, H. Dehghani, J. Wang, S. Jiang, B.W. Pogue, K. D. Paulsen, "Image-guided diffuse optical fluorescence tomography implemented with Laplacian-type regularization," Optics Express 15, 4066–4082 (2007).

[60] A. Corlu, R. Choe, T. Durduran, M. A. Rosen, M. Schweiger, and S. R. Arridge, "Three-dimensional in vivo fluorescence diffuse optical tomography of breast cancer in humans," Optics Express 15, 1–21 (2007).

[61] J. C. Baritaux, K. Hassler, and M. Unser, "An efficient numerical method for general $L_p$ regularization in fluorescence molecular tomography," IEEE Transactions on Medical Imaging 29, 1075–1087 (2010).

[62] P. Mohajerani, A. A. Eftekhar, J. Huang, and A. Adibi, "Optimal sparse solution for fluorescent diffuse optical tomography: theory and phantom experimental results," Applied Optics 46, 1679–1685 (2007).

[63] D. Han, J. Tian, S. Zhu, J. Feng, C. Qin, B. Zhang, and X. Yang, "A fast reconstruction algorithm for fluorescence molecular tomography with sparsity regularization," Optics Express 18, 8630–8646 (2010).

[64] D. Han, X. Yang, K. Liu, C. Qin, B. Zhang, X. Ma, and J. Tian, "Efficient reconstruction method for L1 regularization in fluorescence molecular tomography," Applied Optics 49, 6930-6937 (2010).

[65] J. C. Baritaux, K. Hassler, M. Bucher, S. Sanyal, and M. Unser, "Sparsity-driven reconstruction for FDOT with anatomical priors," IEEE Transactions on Medical Imaging 30, 1143–1153 (2011).

[66] V. A. Morozov, "On the solution of functional equations by the method of regularization," Soviet Mathematics Doklady 7, 414 – 417 (1966).

[67] G. Golub, M. Heath, and G. Wahba, "Generalized cross validation as a method for choosing a good ridge parameter," Technometrics 21, 215-224, (1979).

[68] P. C. Hansen, “The L-curve and its use in the numerical treatment of inverse problems,” Computational Inverse Problems in Electrocardiology 119–142 (2001).

[69] L. N. Trefethen, and D. Bau, Numerical Linear Algebra, SIAM, Philadelphia (1997).

[70] A. B. Bakushinsky, and M. Y. Kokurin, Iterative Methods for Approximate Solutions of Inverse Problems, Dordrecht, Springer (2004).

[71] G. T. Herman, Fundamentals of Computerized Tomography: Image Reconstruction from Projections, Springer-Verlag, London (2009).

[72] R. Gordon, R. Bender, and G. T. Herman, “Algebraic reconstruction techniques (ART) for three-dimensional electron microscopy and x-ray photography,” Journal of Theoretical Biology 29, 471–81 (1970).

[73] G. T. Herman, and L. Meyer, “Algebraic reconstruction techniques can be made computationally efficient,” IEEE Transactions on Medical Imaging 12, 600–9 (1993).

[74] A. H. Andersen, “Algebraic reconstruction in CT from limited views,” IEEE Transactions on Medical Imaging 8, 50–55 (1989).

[75] H. Guan, and R. Gordon, “A projection access order for speedy convergence of ART (algebraic reconstruction technique): A multilevel scheme for computed tomography,” Physics in Medicine and Biology 39, 2005 – 2022 (1994).

[76] X. Intes, V. Ntziachristos, J. P. Culver, A. Yodh, and B. Chance, “Projection access order in algebraic reconstruction technique for diffuse optical tomography,” Physics in Medicine and Biology 47, N1–N10 (2002).

[77] T. Strohmer, and R. Vershynin, “A randomized Kaczmarz algorithm with exponential convergence,” Journal of Fourier Analysis and Applications 15, 262–278 (2009).

[78] L. Wenkai, and F. F. Yin, “Adaptive algebraic reconstruction technique,” Medical Physics 31, 3222–3230 (2004).

[79] D. P. Bertsekas, Nonlinear programming, Athena Scientific, Belmont, MA (1999).

[80] A. Behrooz, C. Kuo, H. Xu, and B. W. Rice, “Adaptive Row-action Inverse Solver for Fast Noise-robust 3D Reconstructions in Bioluminescence Tomography: Theory and Dual-modality Optical/CT In vivo Studies,” Journal of Biomedical Optics 18(7), 076010 (2013).

[81] M. J. Eppstein, D. J. Hawrysz, A. Godavarty, and E. M. SevickMuraca, ‘‘Three-dimensional, Bayesian image reconstruction from sparse and noisy data sets: near-

infrared fluorescence tomography,'' Proceedings of the National Academy of Sciences U.S.A. 99, 9619 – 9624 (2002).

[82] Y. Lin, H. Yan, O. Nalcioglu, and G. Gulsen, "Quantitative fluorescence tomography with functional and structural a priori information," Applied Optics 48, 1328–1336, (2009).

[83] A. X. Cong, and G. Wang, "A finite-element-based reconstruction method for 3D fluorescence tomography," Optics Express 13, 9847–9857 (2005).

[84] X. Song, D. Wang, N. Chen, J. Bai, and H. Wang, "Reconstruction for free-space fluorescence tomography using a novel hybrid adaptive finite element algorithm," Optics Express 15 (26), 18300–18317 (2007).

[85] H. Gao, and H. K. Zhao, "Multilevel bioluminescence tomography based on radiative transfer equation. Part 2: total variation and l1 data fidelity," Optics Express 18, 2894–2912 (2010).

[86] P. Kisilev, M. Zibulevsky, and Y. Zeevi, "Wavelet representation and total variation regularization in emission tomography," Proceedings of IEEE International Conference on Image Processing 1, 702–5, (2001).

[87] J. A. Fessler, and W. L. Rogers, "Spatial resolution properties of penalized-likelihood image reconstruction: Spatial-invariant tomographs," IEEE Transactions on Image Processing 9, 1346–1358, (1996).

[88] L. Rudin, S. Osher, and E. Fatemi, "Nonlinear total variation based noise removal algorithms," Physica D 60, 259–268, (1992).

[89] T. Goldstein, and S. Osher, "The Split Bregman method for L1-regularized problems," SIAM Journal on Imaging Sciences 2, 323–343, (2009).

[90] R. Courant, K. Friedrichs, and H. Lewy, "On the partial difference equations of mathematical physics," Mathematische Annalen, 100, 32–74, (1928).

[91] X. Liu, and L. Huang, "Split Bregman iteration algorithm for total bounded variation regularization based image deblurring," Journal of Mathematical Analysis and Applications 372, 486-495, (2010).

[92] C. T. Kelley, Iterative Methods for Linear and Nonlinear Equations, SIAM, Philadelphia (1995).

[93] A. Behrooz, H. M. Zhou, A. A. Eftekhar, A. Adibi, "Fast total variation regularization for higher resolution in fluorescence tomography: A split Bregman iteration approach," Proceedings of IEEE Photonics Conference (PHO) 2011, 725-726 (2011).

[94] A. Behrooz, H. M. Zhou, A. A. Eftekhar, and A. Adibi, "Toward Robust High-resolution Fluorescence Tomography: A Hybrid Row-action Edge Preserving Regularization," Proceedings of the SPIE 7896, 78961E-78961E-9 (2011).

[95] A. Michelson, Studies in Optics, U. of Chicago Press, (1927).

[96] A. Behrooz, H. M. Zhou, A. A. Eftekhar, and A. Adibi, "Total Variation Regularization for 3D Reconstruction in Fluorescence Tomography: Experimental Phantom Studies," Applied Optics 51(34), 8216–8227 (2012).

[97] D. Strong, and T. Chan, "Edge-preserving and scale-dependent properties of total variation regularization," Inverse Problems 19, S165–S187 (2003).

[98] R. Acar, and C. R. Vogel, "Analysis of bounded variation penalty methods for ill-posed problems," Inverse Problems 10, 1217–1229 (1994).

[99] S. Chang, B. Yu, and M. Vetterli, "Adaptive wavelet thresholding for image denoising and compression," IEEE Transactions on Image Processing 9, 1532–1546 (2000).

[100] D. Sliney, and M. Wolbarsht, Safety with Lasers and Other Optical Sources, Plenum, NY (1980).

[101] ANSI Standard Z136.1, American National Standard for the Safe Use of Lasers, American National Standards Institute, Inc., New York (2000).

[102] M. Harwit, and N. J. A. Sloane, Hadamard Transform Optics: Academic Press, NY (1979).

[103] A. Behrooz, A. A. Eftekhar, P. Mohajerani, and A. Adibi, "Hadamard multiplexed fluorescence molecular tomography: Theory and numerical studies," Proceedings of Lasers and Electro-Optics (CLEO) and Quantum Electronics and Laser Science Conference (QELS), 1-2 (2010).

[104] A. Joshi, W. Bangerth, E. M. Sevick-Muraca, "Non-contact fluorescence opticaltomography with scanning patterned illumination," Optics Express 14, 6516-6534 (2006).

[105] A. Behrooz, A. A. Eftekhar, and A. Adibi, "Hadamard Multiplexed Fluorescence Tomography," Submitted to Biomedical Optics Express.

[106] S. Chow, H. M Zhou, K. Yin, and A. Behrooz, "Solving Inverse Source Problems by the Orthogonal Solution and Kernel Correction Algorithm (OSKCA) with Applications in Fluorescence Tomography," To appear in Inverse Problems and Imaging.

[107] A. Behrooz, A. A. Eftekhar, and A. Adibi, "Toward Compressive Architecture for Image Acquisition in Optical Tomography: An Application of Compressed Sensing

in Wavelet Compression of Fluorescence Tomography Data," in Biomedical Optics, OSA Technical Digest (CD) (Optical Society of America, 2012), paper BTu3A.47.

[108] T. Correia, T. Rudge, M. Koch, V. Ntziachristos, S. Arridge, "Wavelet-based data and solution compression for efficient image reconstruction in fluorescence diffuse optical tomography," Journal of Biomedical Optics 18(8), 086008-086008 (2013).

# VITA

Ali Behrooz received his B.S. in electrical engineering from Sharif University of Technology in Tehran, Iran, in 2007. He was ranked 2$^{nd}$ among 400,000 participants in the national Iranian university entrance examination. He joined the Photonics Research Group at Georgia Institute of Technology as a doctoral student in January 2008 where he developed the first multiplexed fluorescence tomography system. He earned his M.S. and Ph.D. degrees in Electrical and Computer Engineering from Georgia Institute of Technology in Atlanta, GA, in 2011 and 2013, respectively. Ali worked as an R&D intern at Caliper Life Sciences, PerkinElmer, Inc., and AstraZeneca Pharmaceuticals, in 2010, 2012, and 2013, respectively, where he developed image processing and reconstruction techniques for optical tomography and digital pathology systems. Ali served as the president of the Optical Society of America (OSA) student chapter at Georgia Tech from May 2012 to December 2013. His primary field of research is focused on optical imaging and microscopy, image reconstruction, and image processing techniques with applications in biomedicine.